

**STUDY OF UPSET PROTRUSION JOINING PROCESS  
FOR JOINING A CAST MAGNESIUM COMPONENT TO  
OTHER SHEET MATERIALS**

**STUDY OF UPSET PROTRUSION JOINING  
PROCESS FOR JOINING A CAST MAGNESIUM  
COMPONENT TO OTHER SHEET MATERIALS**

**By Nicholas Andrae, B.Sc.**

A Thesis Submitted to the School of Graduate Studies in Partial Fulfillment  
of the Requirements for the Degree Masters of Applied Science

McMaster University © Copyright Nicholas Andrae, September 2015

MASTER OF APPLIED SCIENCE (2015)

McMaster University

(Mechanical Engineering)

Hamilton, Ontario

**TITLE:** STUDY OF UPSET PROTRUSION JOINING  
PROCESS FOR JOINING A CAST MAGNESIUM  
COMPONENT TO OTHER SHEET MATERIALS

**AUTHOR:** Nicholas Andraea, B.Eng

**SUPERVISOR:** Professor Mukesh K. Jain

Department of Mechanical Engineering

McMaster University

**NUMBER OF PAGES:** xxi, 156

## **Abstract**

Magnesium alloys are being increasingly considered for many automotive applications due to their low density and high strength to weight ratio. However, joining of these materials by welding and especially to dissimilar materials such as aluminum or steel or mechanically by riveting at room temperature have faced many challenges. Research presented in this thesis explores a new hot joining process referred to as Upset Protrusion Joining (or UPJ) as a means of mechanically joining a cast magnesium alloy to other similar or dissimilar sheet materials. UPJ is being developed as a rapid and reliable joining method to be implemented in the automotive industry for weight and manufacturing cost reduction. It involves a cylindrical protrusion emanating perpendicular to the flat surface of a cast plate-like magnesium component that is fitted through a hole in another plate or sheet material. The two components are then clamped together, electrically heated and compressed perpendicular to the axis of the protrusion. During this process, the protrusion expands circumferentially to fill the hole as well as the region above the hole thus entrapping the sheet metal between the mushroomed head and the casting.

The effect of different UPJ process parameters such as applied current, current duration, compression loading rate and compression distance were studied through experimentation that involved a newly developed computer-controlled experimental UPJ setup. The studies involved two cast magnesium alloys of interest to the automotive industry, AM60 and AZ91, with protrusions of 11 mm diameter and 14 mm height on a 2 mm thick plate. Studies of the material properties and UPJ process parameters were performed to find optimal process parameters to achieve satisfactory quality of the joint in terms of post-UPJ joint strength with appearance. Also, microstructural studies, temperature measurements in the protrusion region, and electrical resistivity



measurements were performed for the two alloys to fundamentally understand their roles in promoting temperature dependent material flow, strain localization, and fracture in the UPJ process. Lastly, materials specific process window for UPJ process was identified based on the experimental work for creation of robust UPJ joints with acceptable joint strengths in tensile shear mode of failure.

This new hot joining method was shown as an industrially viable joining method for cast magnesium component. UPJ is a rapid joining method and provides good joint-strength depending upon joint specifications. This method can be implemented in automotive and other industrial manufacturing environment for joining cast component to a similar or dissimilar wrought sheet component.

## **Acknowledgements**

First, I would like to state my gratitude to my supervisor, Dr. Mukesh K. Jain providing a challenging, exciting and continually intriguing project as well as providing continual assistance in guidance, direction, and focus. Dr. Sumanth Shankar provided critical management, data analysis and production assistance for this research project and has provided me continual support for years before this project. Dr. Dharmendra Chalasani, co-researcher on the upset protrusion joining project provided exemplary assistance in the material analysis.

I would also like to thank the numerous technicians, researchers, members of the McMaster community and surrounding. The engineering technicians Ron Lodewyks for his invaluable aid in design, Joe Verhaeghe, Michal Lee, John Colenbrander, and Mark MacKenzie for their aid in machining, installation and fabrication. Clealand Berwick provided invaluable aid in precision machining of the hundreds of samples needed. The highly skilled research technician Mike Bruhis provided aid in material testing and analysis as well as direction in experimentation. Dr. Hatem S. Zurob provided equipment for resistivity measurement that lead to improved resistivity sample machining and analysis that lay the groundwork for the system parameters. Dr. R. L. Judd provided help in heating analysis. John Stencil IV from Frank Bacon Machinery Services Sales Co and Josh Garmon from T.J. Snow provided equipment and assistance necessary for the experimental setup to be created and controlled. Everyone in turn provided exemplary support and assistance that made this research possible.

Lastly, I would like to thank Steve Logan, Mohammed Malik and Joe Beckham from Fiat Chrysler Automobiles for providing external assistance and guidance in my research.

# Table of Contents

_Toc435553820Abstract .....	iii
Acknowledgements .....	v
Table of Contents .....	vi
List of Figures .....	xi
List of Tables .....	xx
Chapter 1. Introduction .....	1
1.1] Background .....	1
[1.2] Project Objectives.....	3
[1.3] Thesis Structure .....	4
Chapter 2. Literature Review .....	6
[2.1] Heating Methods.....	6
[2.2] Resistance heating process .....	8
[2.3] Uniaxial Compressive Deformation of Protrusion and Joining.....	12
[2.4] Other UPJ Process Parameters .....	14
[2.4.1] Electrode material selection.....	14
[2.4.2] Heat input .....	15
[2.4.3] Compression Rate.....	16
[2.4.4] Compression Distance .....	17

[2.4.5] Sequence of heating and compression.....	18
[2.5] Cast Magnesium Properties .....	19
[2.5.1] AM60 Alloy .....	21
[2.5.2] AZ91 .....	25
[2.6] Summary.....	30
Chapter 3. Design and Development of a UPJ System.....	32
[3.1] Design Objectives and Requirements.....	32
[3.2] Heating System Design .....	33
[3.2.1] Heating Method .....	33
[3.2.2] Components of the heating system.....	35
[3.3] Mechanical Loading System Design .....	37
[3.4] Integration of Heating and Loading Systems .....	40
[3.5] Safety Considerations.....	42
[3.6] UPJ System Process Limits .....	43
[3.7] UPJ System Process Inputs and Outputs .....	44
[3.8] Summary.....	45
Chapter 4. Experimental Procedure .....	47
[4.1.] UPJ System Details .....	48
[4.1.1.] Process Steps and Sequences.....	48

[4.1.2] Die Cast Protrusion Parts for UPJ Study .....	49
[4.1.3] Part Assembly and Electrode Surface Preparation .....	50
[4.1.4] Current Squared Time Profile and Maximum Current Applied .....	51
[4.1.5] Heating Experiments .....	52
[4.1.6] Current Profile Experiments .....	54
[4.1.7] UPJ Test Repeatability Experiments .....	55
[4.1.8] Experimental Test Matrices .....	56
[4.1.9] Observation and Assessment of UPJ Joints .....	57
[4.2] Isothermal Uniaxial Compression Tests .....	59
[4.2.1] Mechanical test system .....	59
[4.2.2] Test Specimen Geometry .....	60
[4.2.3] Surface Strain Field Measurements .....	61
[4.2.4] Role of Friction in Uniaxial Compression .....	61
[4.2.5] Experimental Test Matrix .....	62
[4.2.6] Observation and Assessment of Test Specimens .....	62
[4.3] Post-UPJ Joint Strength .....	63
[4.4] Electrical Resistivity Measurements .....	63
[4.5] Summary .....	66
Chapter 5. Results .....	67

[5.1.1] True Stress versus True Strain Curves .....	67
[5.1.2] Deformed Specimen Surface and Fracture Characteristics .....	76
[5.2] UPJ Specimen Heating Results .....	83
[5.2.1] Thermocouple-based Results.....	83
[5.2.2] Infrared (IR) Camera-based Results .....	93
[5.3] Cast Protrusion Compression Experiments .....	94
[5.4] UPJ Trial Results .....	96
[5.4.1] Test repeatability results .....	97
[5.4.2] Test Matrix 1 Results .....	99
[5.4.3] Experimental Test Matrix 2 (Taguchi Orthogonal Array) Results.....	118
[5.5] Further Process Optimization .....	121
[5.5.2] AZ91 .....	124
[5.6] Post-UPJ Joint Strength .....	127
[5.6.1] General Observations .....	127
[5.6.2] Post-UPJ Joint Strength of AZ91.....	129
[5.6.3] Post-UPJ Joint Strength of AM60 .....	130
[5.7] Electrical Resistivity Results .....	131
[5.8]. Summary.....	132
Chapter 6. Discussion.....	134

[6.1]. New UPJ Test System Characteristics .....	134
[6.2] High Temperature and High Strain Rate Deformation of Cast Magnesium Alloys AM60 and AZ91 .....	135
[6.3] Current Squared Time Profile (CSTP) as a UPJ Process Variable .....	136
[6.4] UPJ Process Optimization Studies .....	138
[6.5] UPJ Joint Strength Evaluation.....	139
[6.6]. Miscellaneous Experimental Limitations .....	140
Chapter 7. Conclusions .....	144
Chapter 8. Suggestions for Future Work .....	146
Chapter 9. References .....	148

## List of Figures

Figure 1.1. A view of two assembled components prior to UPJ process, a sliced view of a UPJ joint and a successful UPJ joint.....	2
Figure 2.1. Example of inductive heating. ....	7
Figure 2.2. Changes in resistances in a spot weld during the heating operation. ....	10
Figure 2.3. Comparison of electrical resistivity versus temperature of magnesium polycrystal.....	11
Figure 2.4. Contact resistance of one batch of 2 mm thick AZ31 rolled sheets.....	12
Figure 2.5. Comparison of axial versus circumferential strain of compressed steel cylinders.....	13
Figure 2.6. Effect of initial specimen temperature in a strain rate range of 0.2-1.5 s <sup>-1</sup> , and effect of strain rate at 200°C on simple upsetting experiments of AZ31 cylinders.....	14
Figure 2.7. Shear bands forming an X shape within a mild steel cylinder deformed at room temperature with high-friction platens.....	18
Figure 2.8. Compressed Magnesium AZ31 cylinders showing angular fracture and cracks.....	18
Figure 2.9. Effect of temperature on the tensile elastic modulus of a set of pure metals.....	20
Figure 2.10. Effect of temperature on the Poisson's ratio $\mu$ of Aluminum and Magnesium.....	20
Figure 2.11. Compression diagrams of pure Magnesium at 20°C and -180°C, brittle at low temperatures.....	21
Figure 2.12. AM60 microstructural characteristics at a low cooling rate as-cast condition.....	24
Figure 2.13. Optical microstructures of AM60, as-cast and heat-treated at 450°C for 30 min after	



rolling at 375°C with a thickness reduction of 80%.....	25
Figure 2.14. Strain rate sensitivity versus strain rate curves at different temperatures for conventionally cast and rapid solidification.....	27
Figure 2.15. Comparison of tensile strength (Rm) and deformation energy (DE) versus temperature for AZ91 alloy.....	28
Figure 2.16. AZ91 microstructural characteristics in an as cast steel mould and a sand cast mould.....	29
Figure 2.17. Optical microstructures of AZ91 before deformation and after 6 passes of equal channel angular pressing at 325°C.....	30
Figure 3.1. Electrical heating setup, current profiles produced by the MFDC transformer and water chiller used in the setup.....	36
Figure 3.2. UPJ loading system.....	39
Figure 3.3. UPJ testing area and setup. ....	39
Figure 3.4. Voltage to the servo-hydraulic ram and position measured by the LVDT.....	42
Figure 3.5. A sliced view of a UPJ sample after upsetting showing an extensive shape change of the cylindrical protrusion.....	44
Figure 4.1. Applied current and electrode (punch) displacement profile of UPJ process.....	49
Figure 4.2. Die cast test sample geometries for creation of UPJ joints.....	50
Figure 4.3. Sample preparation for UPJ.....	51
Figure 4.4. Thermocouple mounted inside a protrusion, thermocouple welded to the surface of a	

protrusion and the three different thermocouples locations.....	53
Figure 4.5. Photographs showing evidence of burning and melting on the top of a heated AZ91 protrusion.....	54
Figure 4.6. Taguchi orthogonal array for three process parameters.....	57
Figure 4.7. Isothermal uniaxial compression test set-up and a compressed test sample between two compression platens inside the environmental chamber.....	60
Figure 4.8. A cylindrical test sample with a speckle pattern applied to its surface for Aramis-based strain field measurements.....	61
Figure 4.9. Experimental set-up for UPJ joint testing and the specimen in the setup.....	63
Figure 4.10. Electrical circuit for resistivity measurement. The test specimen in the form of a strip is shown in grey.....	64
Figure 4.11. A schematic of a resistivity test-jig, and a photograph of the set-up utilized.....	66
Figure 4.12. A precision magnesium AZ91 sample with aluminum wires bonded to a specimen...	66
Figure 5.1. Barreling of a 14 long and 11 mm diameter cylinder of AZ91 compressed at 400°C and at a rate of 1 mm/minute.....	68
Figure 5.2. Comparison of material flow curves in axisymmetric compression at different temperatures in a true stress versus true strain plot and load versus displacement plot.....	69
Figure 5.3. ARAMIS normal strain from the DIC software of 14mm long AZ91 cylinder compressed at a rate of 10 mm/minute.....	70
Figure 5.4. Comparison of compression load versus displacement traces for AZ91 cylinders tested	

at 300° C and 3 different compression rates.....	71
Figure 5.5. Comparison of compression load versus displacement traces for AZ91 cylinders tested at 350° C and 3 different compression rates.....	72
Figure 5.6. Comparison of compression load versus displacement traces for AZ91 cylinders tested at 400° C and 3 different compression rates.....	72
Figure 5.7. Comparison of compression load versus displacement traces for AZ91 cylinders tested at 5 different temperatures.....	73
Figure 5.8. Comparison of compression load versus displacement traces for AZ91 cylinders tested at 5 different temperatures.....	73
Figure 5.9. Comparison of compression load versus displacement traces for AZ91 cylinders tested at 5 different temperatures.....	74
Figure 5.10. Comparison of lubricated and non-lubricated compression of AZ91 cylinders compressed at different temperatures.....	75
Figure 5.11. A comparison of load versus displacement of lubricated AM60 and AZ91 specimens compressed at different rates.....	76
Figure 5.12. Crack initiation and growth on AZ91 cylinder compressed at a temperature of 350°C at a rate of 10 mm/minute.....	77
Figure 5.13. Comparison of crack initiation as a function of compression distance at different compression rates and temperatures.....	78
Figure 5.14. A comparison of fracture characteristics of AZ91 specimens compressed at 3 different	

compression rates.....	79
Figure 5.15. A comparison of fracture characteristics of uniaxial compressed AZ91.....	80
Figure 5.16. A comparison of deformed AZ91 samples compressed with and without lubrication compressed at 10 mm/min to a height of 4 mm.....	81
Figure 5.17. A comparison of AZ91 and AM60 cylinders compressed with lubrication at 1mm/minute compressed from 10 mm to a final length of 4 mm.....	82
Figure 5.18. Temperature-time trace obtained from a thermocouple mounted inside an AZ91 protrusion at its mid-length.....	83
Figure 5.19. A comparison of temperature-time profiles for AZ91 protrusion from three different locations.....	84
Figure 5.20. A plot of temperature from the middle thermocouple versus applied current.....	85
Figure 5.21. A comparison of temperature increase from the middle thermocouple as a function of duration of constant applied current.....	86
Figure 5.22. A comparison of temperature-time profiles at the mid-length position of an AZ91 protrusion heated for 4 different time durations.....	87
Figure 5.23. A comparison of temperature-time profiles for AM60 protrusion.....	88
Figure 5.24. A comparison of temperature-time traces for surface mounted thermocouple located in the middle of an AM60 protrusion heated over increasing durations.....	89
Figure 5.25. A comparison of temperature-time profiles from surface mounted thermocouples located in the middle of an AM60 protrusion.....	89

Figure 5.26. A comparison of surface temperature-time profiles for AZ91 protrusion heated with 0 to 11kA over 0.66 seconds.....	91
Figure 5.27. A comparison of temperature-time profiles from surface mounted thermocouples located in the middle of an AZ91 protrusion subjected to a CSTP of 81 kA <sup>2</sup> -s.....	92
Figure 5.28. Two experimental results from the infrared camera under the same current profile conditions.....	94
Figure 5.29. Load versus time traces from repeated UPJ experiments. ....	98
Figure 5.30. Position versus time traces from repeated UPJ experiments.....	98
Figure 5.31. A comparison of visual appearance of UPJ heads from 5 repeat tests.....	99
Figure 5.32. A comparison of load versus time traces for AM60 protrusions compressed at a rate of 21mm/s and a CSTP of 141 kA <sup>2</sup> -s.....	100
Figure 5.33. A comparison of images of protrusion head compressed at a rate of 31.5 mm/s and with the same CSTP of 100 kA <sup>2</sup> -s with different maximum current.....	101
Figure 5.34. A defect-free UPJ head from AM60 protrusion formed with a maximum current of 15 kA for 0.63 seconds and corresponding to a CSTP of 140 kA <sup>2</sup> -s, at a compression rate of 21 mm/s.....	102
Figure 5.35. A comparison of changing the CSTP on the load versus time traces for AM60 alloy. ....	103
Figure 5.36. Effect of change in energy input on fracture characteristics of AM60 protrusion....	104
Figure 5.37. A comparison of load versus displacement for 3 different compression distances...	105

Figure 5.38. Comparison of compression distance on the presence of crack size and density.....106

Figure 5.39. Optical micrographs of the sliced and mounted AM60 protrusion samples at different compression distances.....107

Figure 5.40. Load versus displacement traces at 3 different compression rates.....108

Figure 5.41. A comparison of compression rate of AM60 compressed at different rates.....109

Figure 5.42. Microstructure comparison of compression rates for AM60 specimen heated with 0 to 11.5kA over 1.08 seconds with a CSTP of 141 kA<sup>2</sup>-s.....109

Figure 5.43. A comparison of load versus time traces for compression for AZ91 protrusions compressed by 10 mm at a rate of 21mm/s with a CSTP value of 100 kA<sup>2</sup>-s.....110

Figure 5.44. Images of AZ91 protrusion heads with different maximum applied current.....111

Figure 5.45. A comparison of punch load versus displacement traces for AZ91 with different CSTP values.....112

Figure 5.46. Images of protrusion head of the UPJ joint with AZ91 protrusion for different CSTP inputs.....113

Figure 5.47. AZ91 protrusions subjected to CSTP beyond the operational range.....113

Figure 5.48. A comparison of load versus displacement of protrusions for different compression distances.....114

Figure 5.49. Comparison of compression distance on the presence of crack size and density.....115

Figure 5.50. Optical micrographs of the sliced and mounted AZ91 protrusion samples compressed to different distance.....116

Figure 5.51. A comparison of load versus time and load versus displacement traces for AZ91 protrusion compressed at 4 different compression rates.....	117
Figure 5.52. AZ91 UPJ protrusion head characteristics as a function of compression rate.....	118
Figure 5.53. Results of Taguchi analysis for UPJ process optimization for part quality of AM60 alloy.....	119
Figure 5.54. Three repeat tests for AM60 alloy based on Taguchi optimal process variables.....	120
Figure 5.55. Results of Taguchi analysis for UPJ process optimization for part quality of AZ91 alloy.....	121
Figure 5.56. Three repeat tests for AM60 alloy based on Taguchi optimal process variables.....	121
Figure 5.57. Comparison of compression rate on joint visual quality.....	122
Figure 5.58. AM60 protrusion compressed at a rate of 21 mm/s and different distances.....	123
Figure 5.59. Comparison of two AM60 UPJ joints produced using applied current of 0 to 15 kA over 0.62 seconds and compressed a compression rate of 21mm/s.....	124
Figure 5.60. Comparison of surface quality of magnesium AZ91 heated with different CSTP values.....	125
Figure 5.61. Cross-sectional views of the AZ91 UPJ joints compressed different distances.....	126
Figure 5.62. Failure modes associated with UPJ joints from tensile tests.....	128
Figure 5.63. Cavities inside an upset protrusion formed in AM60 during the upsetting process...	129
Figure 5.64. Comparison of tensile shear failure loads from UPJ joints obtained from Experimental Test Matrix 1.....	130

Figure 5.65. Taguchi output matrix in terms of failure load.....131

Figure 5.66. Electrical resistivity as a function of temperature of AZ91 and AM60.....132



## List of Tables

Table 2.1. Mass percentage composition of AM60 alloy.....	21
Table 2.2. Physical properties of AM60 alloy.....	22
Table 2.3. Material properties of AM60 alloy at room temperature.....	23
Table 2.4. Mass percentage composition of AZ91 showing maximum and minimum limits for the different alloying elements.....	26
Table 2.5. Physical properties of AZ91 alloy in F (as fabricated) temper.....	26
Table 2.6. Material properties of AZ91 alloy in F temper condition. ....	27
Table 3.1. Comparison of different methods of heating a protrusion for the UPJ process.....	34
Table 3.2. Mechanical loading system capabilities.....	40
Table 4.1. UPJ joint quality grading method.....	63
Table 5.1. Comparison of temperatures measured by a centrally located thermocouple inside an AZ91 protrusion heated with the same CSTP of 81 kA <sup>2</sup> -s.....	87
Table 5.2. A comparison of maximum internal and external temperatures from AM60 81 kA <sup>2</sup> -s CSTP experiments.....	90
Table 5.3. A comparison of applied current, current duration and maximum internal and external temperatures attained in AZ91 protrusions.....	93
Table 5.4. Comparison of compressions of AZ91 cast plate to set distances.....	96

## **Chapter 1. Introduction**

### **1.1] Background**

Magnesium alloys as lightweight automotive materials have been gaining considerable popularity in last decade or so. In addition to their low density compared to most industrial metallic materials, they can have desirable mechanical properties for many automotive structural applications. However, their poor room temperature ductility, weldability and corrosion resistance have prevented their implementation on a larger scale. Magnesium's highly anodic properties cause corrosion when electrically bonded to less anodic metals. Atoms of copper from equipment used to bond magnesium have been found to be key factors in magnesium corrosion (Zeng, 2010). Surface corrosion causes large variation in welding magnesium due to oxidization on the skin surface even when comparing over the same batch of rolled magnesium sheet (Liu et al. 2009). Much effort is being made to overcome these limitations. Recent developments in magnesium alloys have significantly reduced corrosion, bringing a rapid increase in demand for magnesium alloys (Matos, 2010).

As an alternative to welding, Upset Protrusion Joining (UPJ) is a very recent mechanical joining process developed by FCA US LLC to join cast magnesium to other sheet-like components such as aluminum or steel sheets. A cast component with a cylindrical protrusion on one side is fitted through a hole in another sheet-like part made from wrought component (see Figure 1.1(a)). The assembly is then clamped, rapidly heated, and plastically deformed in compression (upset) by applying a load on the top face of the protrusion and bottom plate surface. Application of load 'mushrooms' the protrusion, entrapping the metal sheet between the mushroomed head and the

casting (see Figure 1.1(b,c)). This process is being developed for automotive application, but can be potentially applied to other industries to mechanically join components with poor room temperature ductility.

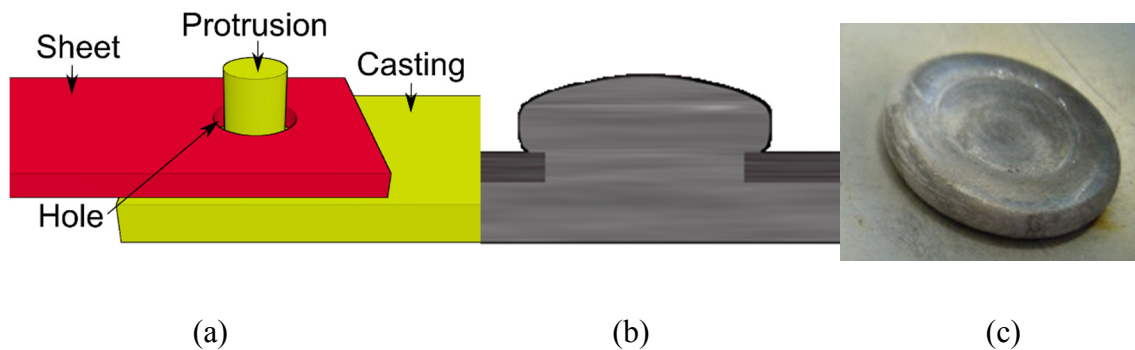


Figure 1.1. UPJ process, (a). a view of two assembled components prior to UPJ process, (b) a sliced view of a UPJ joint formed by axially compressing the cylindrical protrusion where a mushroomed head entraps the sheet metal between the head and the casting, (c) a photo of the protrusion head as part of a successful UPJ joint made from a cast magnesium alloy.

The current UPJ process uses an industry standard Mid-Frequency Direct Current (MFDC) resistance heating system (commonly associated with spot welders) to rapidly heat the protrusion to a set warm forming temperature. The protrusion is then rapidly compressed using a ram to create a UPJ joint. There is also a need for development of a well-instrumented and computer-controlled UPJ test system. Such a system can be then utilized for a better understanding of the UPJ process in terms of interrelationships between process variables, component design and material parameters, and quality and performance of the UPJ joint. Also, performance of different materials can be assessed using such a system and material specific process optimization can be carried out to achieve a more desirable joint quality.

Key challenges in the UPJ process development for industrial use are finding a suitable range of material parameters (such as microstructural characteristics of the cast alloys, physical and mechanical properties) and process parameters such as heating rates, temperatures, loads, strains and strain rates (or process speeds). So far electrical resistance heating has been utilized as a viable heating method for the UPJ process. However, the relationship between applied current, current duration and the resulting temperature of the parts to be joined has not been developed either experimentally or via numerical modeling work. Such a relationship appears to depend on a host of seemingly diverse material and process parameters as discussed in the next chapter.

This thesis attempts to further develop our understanding of the UPJ process in a laboratory setting, specifically for two cast magnesium alloys, AZ91 and AM60, of interest, in general, to the automotive industry. In order to develop this understanding, much effort has been devoted over a period of more than a year towards the development of a new well instrumented and computer controlled UPJ experimental set-up. The new set-up is then utilized to systematically study the effect of many of the UPJ process variables on joint visual quality and strength.

## **[1.2] Project Objectives**

The development of an experimental test apparatus to produce UPJ joints was a key first objective of this research. Finding parameters such as compression rate, compressive loads, electrical current and power demands proved difficult due to the unique and un-researched process of UPJ. Experimentation with an in-house spot welder, isothermal compression tests, and aid from industry proved invaluable in establishing experimental conditions and limits for the new system. The new UPJ test system was created by combining a refurbished servo-hydraulic mechanical test

system with a ram and a refurbished MFDC resistance heating system. Details of this system are provided in Chapter 3.

Another key objective was to optimize the new UPJ process in terms of two key output variables, visual quality of the UPJ joint and performance of the joint in terms of failure load in tensile shear mode. Beyond surface quality and strength, the process was optimized to produce a joint reliably, rapidly (under 2 seconds) and with an equipment setup that could be mounted onto a robot arm in an industrial environment. Upsetting without cracking of the protrusion head was a key goal of the UPJ experiments. This optimization was carried out experimentally for two cast magnesium alloys, AM60 and AZ91. The optimization effort involved selection of key measurable and controllable process parameters and systematically varying those parameters to relate the process to joint quality. Additionally, a Taguchi orthogonal array was utilized for experimental process optimization.

### **[1.3] Thesis Structure**

The thesis is structured as follows. Chapter 2 presents a literature review of topics closely related to the UPJ process such as electrical resistance heating, large strain, high strain rate, and high temperature compression of cast magnesium alloys. While reviewing the literature, available data is summarized wherever possible and topics where information and knowledge is lacking are identified. Chapter 3 presents details of the new UPJ system in terms of design goals, process steps and characteristics after commissioning of the equipment, test-to-test repeatability, safety and other considerations. Chapter 4 describes various experimental procedures associated with not only the UPJ experiments but also several other complementary experiments such as isothermal uniaxial

compression tests on cylindrical specimens, electrical resistivity measurements as a function of temperature for AM60 and AZ91 alloys, post-UPJ joint testing etc. Chapter 5 presents the results of UPJ experiments and various complementary experiments based on several different experimental test matrices. The key findings and results from Chapter 5 are discussed in Chapter 6 with the goal of explaining the nature of the results as well as their shortcomings. This is followed by conclusions in Chapter 7 and suggestions for future work in Chapter 8. A list of references are provided in Chapter 9 at the end of the thesis.

## **Chapter 2. Literature Review**

Mechanical joining offers a cost-effective solution for joining of similar and dissimilar sheet materials for many industrial applications. It is especially useful in applications where welding is quite difficult such as for joining of magnesium cast components to aluminum or steel in an automotive structure. Upset protrusion joining (UPJ), a new mechanical joining process, is being experimentally studied for joining cast magnesium to other materials. UPJ has been shown to be a viable process for use in automotive industry for joining AM60 and AZ91 cast magnesium components to other wrought sheet (or plate-like) components. In this chapter various fundamental aspects of the UPJ process in terms of heating methods (including the electrical resistance heating method), mechanical joining, and large deformation behavior of candidate cast magnesium alloys are reviewed.

### **[2.1] Heating Methods**

There are many possible ways for locally heating sheet material prior to forming. These include furnace heating, induction heating, infrared radiation heating and electrical resistance heating. Furnace heating has many serious drawbacks in terms of cycle time and energy consumption. The effects of heating of the nearby components, as well as the obstruction of the short manufacturing sequence are typically the main disadvantages of using this heating technique. Therefore, it is more desirable to locally heat up the UPJ joint region. Inductive heating is another common approach for heating up components to be joined where heating can be applied locally to raise the temperature of the sheet metal. Figure 2.1 illustrates a heating process with inductive

heating. This heating technique was effective in joining magnesium alloys, but it does not preclude disadvantages such as increase in cycle time and attaining a well-defined temperature profile as a function of process parameters.

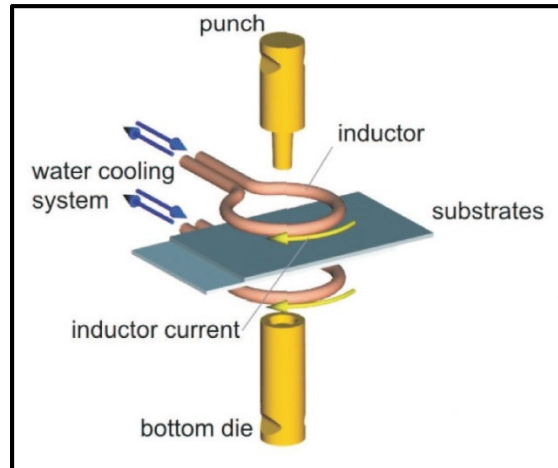


Figure 2.1. Example of inductive heating (Coppieters, 2012).

Infrared radiation heating is a relatively easy and flexible heating technique where heating time and radiation intensity are parameters that can be adjusted based on the material type and thickness, to control the heating process to attain the desired temperature. Moreover, ‘no contact’ nature of this process results in no surface contamination of the components to be joined. The main drawback that limits its use for the UPJ process is the inhomogeneous heating of the sample as the heat is largely transmitted from the surface to the centre of the protrusion. Also, there will be heat losses during the UPJ process as well as an increase in the cycle time.

Lastly, resistance heating is an interesting heating technique that is based on heat generation due to passing of a high current through a resistance. This heating method has many advantages of the previous heating techniques including rapid heating. Also, it is easier to control



the heating rate by adjusting the current value and its duration to locally heat the protrusion region to the desired temperature. The efficacy of the process, however, does depend upon a large number of variables that need to be carefully considered.

## [2.2] Resistance heating process

Resistance heating is a function of applied current, current duration, resistivity of the work piece, surface contact resistance, and temperature. Electrical energy in resistance heating can be expressed as follows:

$$Energy = \int_0^{t_f} I^2(t) * R(t) dt \quad (2.1)$$

where  $I$  and  $R$  are is applied current and effective resistance respectively. Both of these quantities can be made to vary with time variable  $t$ , and  $t_f$  is the final time (or the total current duration) (Mucha et al. 2011). This energy is then directly converted to heat. The energy density is found through current density, by dividing the current by the cross sectional area. In the resistance heating of a UPJ joint, the protrusion can be assumed to be a uniform cylinder of constant cross-sectional area, and so current density is the same throughout. The magnitude of the current and its duration can be controlled (or kept constant). Therefore, equation (2.1) can be simplified to the following equation:

$$Energy = I^2 R t_f \quad (2.2)$$

Energy expression (2.2) can be further simplified, if one assumes a linear ramp function for current (i.e., current increasing from 0 to a final current value  $I_f$  over the duration of  $t_f$ ).

Further, assuming resistance  $R$  to be constant, equation (2.1) yields,

$$Energy = \frac{I_f^2 R t_f}{3} \quad (2.3)$$

Resistance heating is utilized extensively for spot welding where high electrical currents are passed through metal inducing heat within the material. This is commonly used to form a nugget of liquid metal between two sheets of metal, forming a spot weld. The resistance heating in the UPJ process does not heat the material to a liquid state, but, excluding the melting in a spot weld, the heating principles are the same.

Electrical resistance heating is governed by the cross sectional area ( $A$ ) and length ( $L$ ) in which the current is passed, surface contact resistance between electrode and sheet ( $R_{surf}$ ) and the bulk resistivity ( $\phi$ ) of the material as follows:

$$R_{net} = \frac{L\phi}{A} + 2 * R_{surf} \quad (2.4)$$

At the initiation of current flow in a resistance heating process such as spot welding, it is common for the surface resistances to be larger than the material's bulk resistance. However, as the temperature increases the material's resistivity also increases until the weld nugget forms and the faying surface (i.e., surface where parts are joined together in welding) is replaced with a liquid weld nugget (see Figure 2.2). It is to be noted that equation (2.4) is for a single sheet in a spot welding and assumes that the current passes directly through the sheet thickness between the electrodes without any transverse spread.

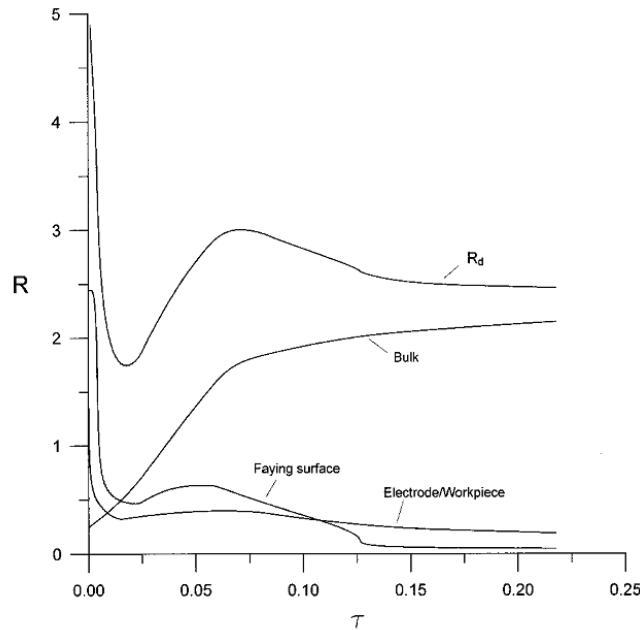


Figure 2.2. Changes in resistances in a spot weld during the heating operation. The net resistance ( $R_d$ ) is a sum of the bulk material resistance, the electrical resistance between the two sheets (Faying surface) and the resistance between the electrode and the workpiece (Electrode/workpiece). (Wang, 2001)

As shown in Eqn. (2.1), increasing current increases the energy entering the protrusion non-linearly (as a function of square of the applied current) and increasing duration increases the energy linearly. The energy entering the protrusion can also be applied in a ramp function, reducing the amount of energy entering the protrusion according to Eqn. (2.3), but preventing the initial surface contact resistance seen in Figure 2.2 from heating the surface far more rapidly than the bulk of the material.

Bulk electrical resistivity of a material depends upon alloy composition, grain size, and defects within the material volume as well as temperature  $T$ . Resistivity increases as a function of

$T^4$  with the exception of superconducting temperatures (approaching  $0^\circ K$ ). However, due to the limited temperature range and room temperature to warm-forging temperature setup, a linear increase in resistivity as a function of temperature is often assumed (Ho et al., 1983). In fact, many experiments on many magnesium alloys have shown a linear increase in resistivity with temperature, (see Figure 2.3, Yakubtsov, 2010)

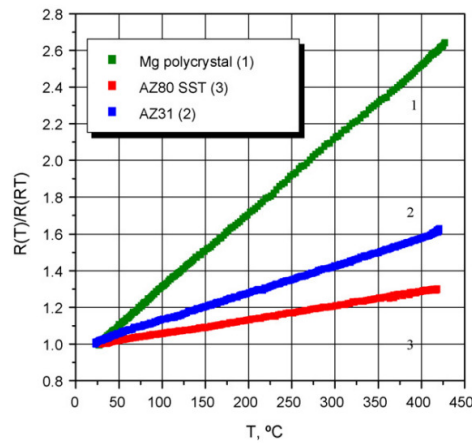


Figure 2.3. Comparison of electrical resistivity versus temperature of magnesium polycrystal (line 1), AZ31 alloy (line 2) and magnesium SST alloy (line 3). (Yakubtsov, 2010)

Magnesium surface contact resistance has a high variability as a function of the surface conditions. Repeated experiments from one batch of magnesium AZ31 sheet metal were found to have a variability in surface resistance of over 10,000 times (see Figure 2.4 below). The sheet was then cleaned with dichromic ( $H_2Cr_2O_7$ ) acid and the variability was reduced to only about 80 times. The use of dichromic acid and a consequent reduction in the surface resistance increased the repeatability and quality of the joints (Liu et al., 2009).

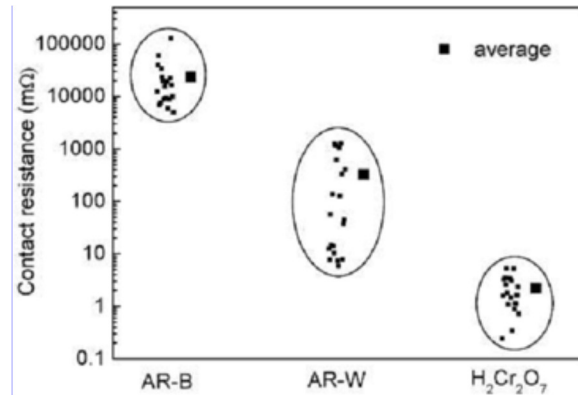


Figure 2.4. Contact resistance of one batch of 2 mm thick AZ31 rolled sheets. Some sheets from the batch were visibly black (AR-B) or white (AR-W). Sheets were also cleaned with dichromic acid (H<sub>2</sub>Cr<sub>2</sub>O<sub>7</sub>) producing a significantly lower contact resistance (Liu et al., 2009).

### [2.3] Uniaxial Compressive Deformation of Protrusion and Joining

The UPJ process is akin to riveting process in that a cylinder of material protruding from a base is fitted through a hole in sheet metal and upset, entrapping the sheet metal between the base of the rivet and the upset head. This upsetting process is governed by the material properties of the protrusion, temperature, compression rate, compression distance and the friction coefficient between the platen (die) and the material. Friction coefficient at the tool and work piece in the contact region as well as surface conditions govern the surface circumferential (or hoop) strain that develop during compressive loading. Studies on lubricated, polished and roughened platens indicate that reducing the coefficient of friction (polished and lubricated case) increases the slope of axial and circumferential strain curve as shown in Figure 2.5 and thereby allows increased compression of the cylinders. It has been also shown to reduce barrelling of the cylinder.

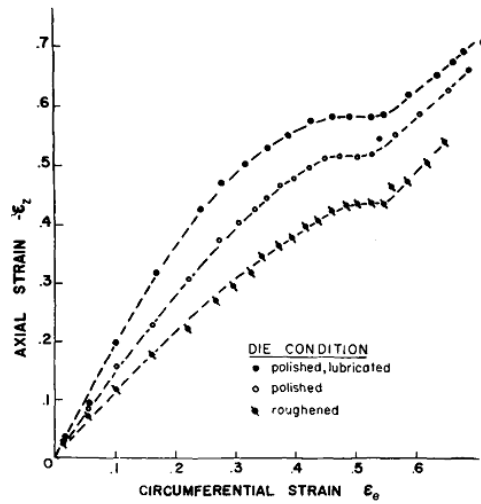


Figure 2.5. Comparison of axial versus circumferential strain of compressed steel cylinders. (Kuhn et al., 1971)

Workpiece temperature and compression rate (i.e., strain rate), and compression distance (i.e., strain) are parameters that govern crack formation in simple cylindrical upsetting processes that involve a cylinder under axial compression. In compression experiments on AZ31 under warm forging temperatures and controlled compression profiles, higher temperatures improved ductility as shown by increased height reductions in Figure 2.6 (left). (Matumoto et al., 2010). Increased compression rate, on the other hand, yielded lower heights before crack formation (Figure 2.6 (right)).

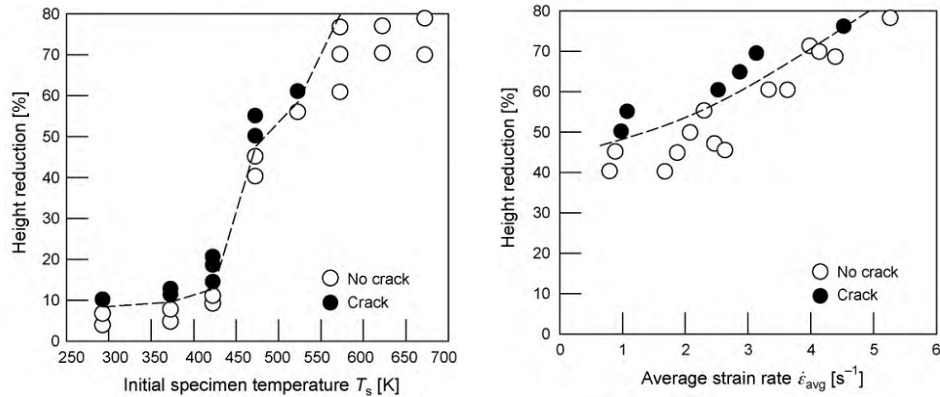


Figure 2.6. Simple upsetting experiments on AZ31 cylinders, (left) effect of initial specimen temperature in a strain rate range of 0.2-1.5 s<sup>-1</sup>, (right) effect of strain rate at 200°C, (Matumoto et al., 2010).

## [2.4] Other UPJ Process Parameters

Besides the resistance heating and mechanical deformation parameters there are several others that are likely to affect the performance of the UPJ process. These are briefly discussed in this sub-section.

### [2.4.1] Electrode material selection

The electrodes are typically made from a low resistivity material and are water cooled to keep their temperature below their melting point to avoid any melting. Also, the electrode material for resistance heating should have sufficient strength and not deform plastically under applied load at its peak operating temperature. Treatments for improving material strength, such as alloying, heat treating and work hardening, result in an increase in its electrical resistance. Therefore, a good compromise of high strength (electrode performance and life) and low resistivity must be made. Also, the electrode should have no reactivity with the metals being joined. For the present UPJ

work, one needs to be concerned about copper electrodes as any transfer of copper to magnesium is considered detrimental to the properties of the joint, especially from corrosion perspective. Magnesium is highly anodic and strongly reacts with copper (Zeng et al., 2009). Molybdenum and tungsten based alloys are considered good candidate electrode materials for spot welding applications (Spotwelding Consultants, 2015).

#### **[2.4.2] Heat input**

When electricity is passed through a resistive material, nearly all electrical energy is converted into heat (with the remainder converted into sound and light and lost to the surroundings). Through precision in electrical design, the amount of energy entering a specimen can be controlled. Since electrical resistance heating converts heat energy to temperature through the material's specific heat, a closed loop control system (or experimentation to devise an accurate open loop control system) to account for heat losses to the surroundings is required. The heat energy resides internally in the specimen and is first redistributed through conduction to the surface, then by conduction to other contacting bodies, and finally by convection and radiation to the surroundings. This, in essence, is quite different from other sources of heat energy such as a flame, torch, hot liquid, or gas where heat flux is transported from the external surface to the bulk. The advantage of an external heat source is that it can be more readily used to set the temperature of the work piece. On the other hand, a key advantage of electrical resistance heating is the precision and control over the current entering the protrusion as well as more uniform internal heating of the work piece. The amount of current, and in effect, energy entering a specimen can be controlled as all or nearly all of the heat energy is added to the system (Hynes, 1948).



A unique spot welding setup was developed and experimented upon at the Chinese Academy of Science in Beijing, China, comparing the popular constant current control (CCC) to a rather uncommon constant power control (CPC) systems. The CPC system actively measured and controlled current and voltage across the electrodes during welding and manipulated the voltage to produce a constant power input into the sheet material. The experiment yielded CPC to be less versatile and requiring higher power consumption compared CCC due to the high surface contact resistance prior to weld nugget formation (Kang et al. 2015). A CPC system may be preferable for the UPJ process due to control of the amount of energy entering the protrusion if surface contact resistance was kept constant.

### **[2.4.3] Compression Rate**

Compression rate (or speed of compression) is closely related to strain rate at which a material is deformed. The latter is a universal process variable associated with high temperature processing and forming of materials. It is always preferable that plastic forming processes are carried out at high compression (or strain) rates to minimize the process time. The flow stress of most metallic alloys at higher temperature depends critically on strain rate. Typically the flow stresses increase with increase in strain rate at higher temperatures. This increase in flow stress is often expressed in terms of strain rate sensitivity of the material, or its so-called m-value. The following classical expression relates flow stress to strain rate under isothermal conditions,

$$\sigma = C\dot{\epsilon}^m \quad (2.5)$$

where C and m are material constants. The m-value is typically in the range 0.1-0.2 for most metallic materials deformed at higher temperatures (Campbell, 2008). More comprehensive flow

stress, strain rate, strain and temperature relationships, also referred to as material constitutive law, are available in the literature. One such relationship by Johnson et al. (Johnson & Cook, 1983) is expressed as,

$$\sigma(\epsilon_p, \dot{\epsilon}_p, T) = [A + B(\epsilon_p)^n][1 + C \ln(\dot{\epsilon}_p)][1 - (T)^m] \quad (2.6)$$

where  $A$ ,  $B$ ,  $C$ ,  $m$  and  $n$  are material constants,  $T$  is temperature,  $\epsilon_p$  is equivalent plastic strain,  $\dot{\epsilon}_p$  is equivalent plastic strain rate, and  $\sigma$  is the flow stress.

#### [2.4.4] Compression Distance

Compression distance is a process variable that is closely related to applied axial strain in the context of UPJ process. An increase in compression distance results in development of three-dimensional principal plastic strain state in a cylindrical specimen; radial, axial and circumferential (or hoop) strains, when barrelling occurs. Since only two of the principal plastic strain components are fully independent at a material point in the work piece because of the plastic incompressibility assumption, the surface axial strains and hoop strains can be utilized to assess surface strain development as a function of compression distance. Since failure typically initiates from the surface of a highly barrelling specimen under upsetting process, a crack initiation criterion based on these two strain components or their combination in the form of so-called effective strain at fracture is often measured via experiments (Marciniak et al., 2002). The deformation process can also be localized during upsetting process in the form of a pair of shear bands that propagate diagonally across the deforming protrusion (see Figure 2.7 below) to create an ‘X’ shape where most of the deformation becomes concentrated. This form of strain localization is more common at lower temperatures or at higher strain rates where adiabatic heating results in flow softening of

the material along the shear bands and consequent failure of the specimen (see Figure 2.7 below).



Figure 2.7. Shear bands forming an X shape within a mild steel cylinder deformed at room temperature with high-friction platens (Semiatin & Jonas, 1984).

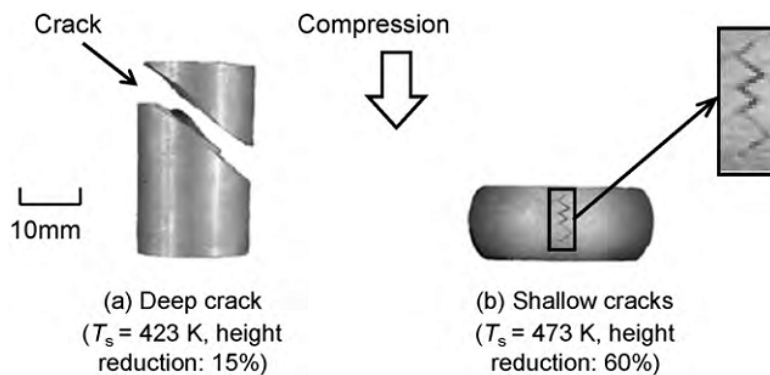


Figure 2.8. Compressed Magnesium AZ31 cylinders showing angular fracture and cracks, (a) inclined fracture common at low temperature compression, (b) shallow cracks that are attributed to higher compression rate and/or overheating (Matumoto et al. 2010).

#### [2.4.5] Sequence of heating and compression

Since the UPJ process involves application of heat and mechanical load (or pressure) to the protrusion to form it into a mushroomed protrusion head UPJ joint, it is also useful to know the time sequence of heating and deformation processes. There are two basic possibilities in terms of applying the heat and deformation; concurrently or sequentially. Clearly, concurrent application of heat and load to the work piece is a more efficient process compared to heating first and then

applying the load. However, when the process is very rapid such as the UPJ process, it is possible that the work piece may not have reached a suitable temperature and the load (or strain) limit for fracture may be still quite low. This can lead to premature fracture of the joint. On the other hand, a sequential application of heating followed by plastic loading of the work piece is not as efficient in term of cycle time but the process does allow for a greater control of heating parameters to achieve the desired forming temperature including a time delay to ensure homogenization of temperature within the work piece so that it may have enough ‘plasticity’ within in the work piece to attain the desired UPJ joint shape without cracking. Unfortunately, no systematic studies related to the two cases noted above could be found with reference to high temperature simple upsetting process or other processes similar to the UPJ process.

## **[2.5] Cast Magnesium Properties**

For the Mg alloys of interest in the present study, most material properties reported in the literature were at 20°C and not a function of temperature. Due to the nature of the UPJ process, changes in material properties as a function of temperature was desired. Some material properties for pure magnesium as a function of temperature could be found, as shown in Figure 2.8-2.11. Noticeable is a decrease in tensile elastic modulus, an increase in Poisson’s ratio, and a decrease in compressive flow stress for magnesium at elevated temperatures (Buch, 1999).

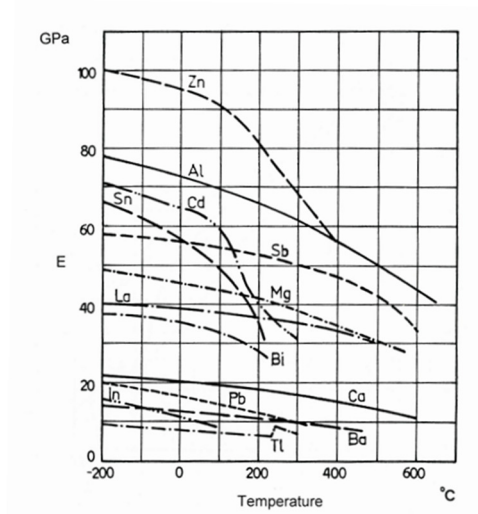


Figure 2.9. Effect of temperature on the tensile elastic modulus of pure metals Zn, Al, Cd, Sn, Sb, Mg, La, Bi, Ca, Pb, In, Ba, Ti (Buch, 1999).

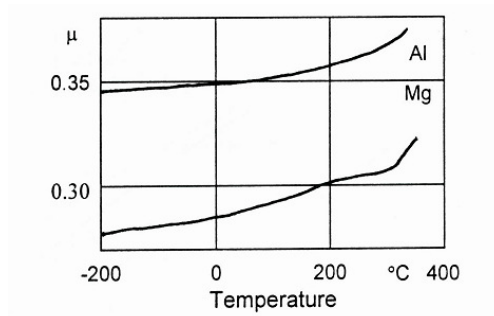


Figure 2.10. Effect of temperature on the Poisson's ratio  $\mu$  of Aluminum and Magnesium (Buch, 1999).

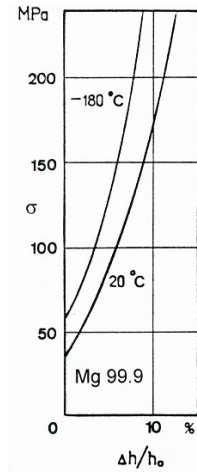


Figure 2.11. Compression diagrams of pure Magnesium at 20°C and -180°C, brittle at low temperatures (Buch, 1999).

### [2.5.1] AM60 Alloy

#### [2.5.1.1] Physical

AM60 is a common cast magnesium alloy that is composed primarily of aluminum and manganese with set limits of copper, silicon and zinc. The mass percentages of different alloying elements are shown in Table 2.1. Corrosion resistance decreases with increasing Fe, Cu, or Ni content (Ricketts, 2014). The metal surface can go from a light white shine to a dark gunmetal grey depending on surface oxidation or corrosion. Other physical properties are shown in Table 2.2.

Table 2.1. Mass percentage composition of AM60 alloy. (Buch, 1999)

Element	Al	Mn	Si	Cu	Zn	Ni	Mg
Percentage	5.5-6.5	0.24-0.6	0.10 max.	0.010 max.	0.22 max.	0.002 max.	balance

Table 2.2. Physical properties of AM60 alloy (Buch, 1999).

Density	1.80 g/cm <sup>3</sup>
Liquidus Temperature	615°C
Solidus Temperature	540°C
Coefficient of Linear Thermal Expansion (CTE)	25.6 μm/m.K
Thermal Conductivity	61 W/m.K at 20°C
Electrical Resistivity at 20°C	0.0000120 ohm-cm

Thermal diffusivity was calculated from the above parameters and the specific heat of magnesium AM60 as shown in Equation 2.7. The specific heat of magnesium AM60 was found as 1.02 J/g\*K (Engineering Casting Solutions, 2006), yielding a thermal diffusivity of 33.2 mm<sup>2</sup>/s.

$$D = \frac{\kappa}{\rho C_p} \quad (2.7)$$

Equation 2.7. Where  $\kappa$  is thermal conductivity,  $\rho$  is density and  $C_p$  is specific heat.

Properties such as change in electrical resistivity and thermal conductivity as a function of temperature, and surface conductivity were unavailable in the literature for this alloy. Therefore, some of these properties, specifically, the change in resistivity as a function of temperature, was experimentally measured in this study as described in Chapter 4.

### [2.5.1.2] Mechanical

Mechanical properties of AM60 alloy at room temperature from uniaxial tests are shown in Table 2.3. Yield and fracture strengths increase with loading speed, but the alloy is not strain rate sensitive in the strain rates range from  $3.3 \times 10^{-4} \text{ s}^{-1}$  to  $0.1 \text{ s}^{-1}$ . Impact energy is not sensitive to temperature (Yan et al, 2008). Strain rates present in the UPJ process and strain rate sensitivity at

elevated temperatures for AM60 could not be found in the literature.

Table 2.3. Material properties of AM60 alloy at room temperature (Buch, 1999).

Tensile Strength	241 MPa
Tensile Yield Strength	131MPa
Tensile Elongation	13% in 50mm
Compressive Yield Strength	131MPa
Poisson's Ratio	0.35
Elastic Modulus (Tension)	45 GPa

### [2.5.1.3] Cast Microstructures

The 'A' in the Mg alloy designation 'AM60' indicates that aluminum is the main alloying element and the first numeral is the approximate wt% of Al. Therefore, AM60 contains 6 wt% aluminum. When the alloying additions (such as Mn, Zn, Si, and rare earth elements) are made to Mg-Al alloys in small proportions, these elements are most likely segregate to form secondary phases after the primary phase (Mg) has nucleated, and therefore, show little effect on nucleation of primary phase (Luo, 1996). The cooling rates that are usually employed in die-castings of commercial Mg alloys such as AM60 are sufficient for the formation of eutectic phase (Polmear, 1989), and therefore these alloys contain a significant volume fraction of the eutectic phase. In the Mg alloys with less than 10 wt% Al (Guldberg, 1997), it is reported that the eutectic morphologies are usually fully or partially divorced.

#### [2.5.1.3.1] Undeformed State

The typical microstructure of the cast AM60 alloy that is used in the present study is shown in Figure 2.11 left. The microstructure exhibits grain size in the range of 20  $\mu\text{m}$  to 30  $\mu\text{m}$  and primarily consists of  $\alpha_{\text{Mg}}$  matrix,  $\text{Mg}_{17}\text{Al}_{12}$  intermetallic particles and the eutectic ( $\alpha_{\text{Mg}}+\text{Mg}_{17}\text{Al}_{12}$ )



that are precipitated on the grain boundaries (Mrvar et. al. 2006). X-ray diffraction plot for the cast AM60 alloy is shown in in Figure 2.11(b). The peaks in the spectrum confirms the presence of  $Mg_{17}Al_{12}$  intermetallic particles.

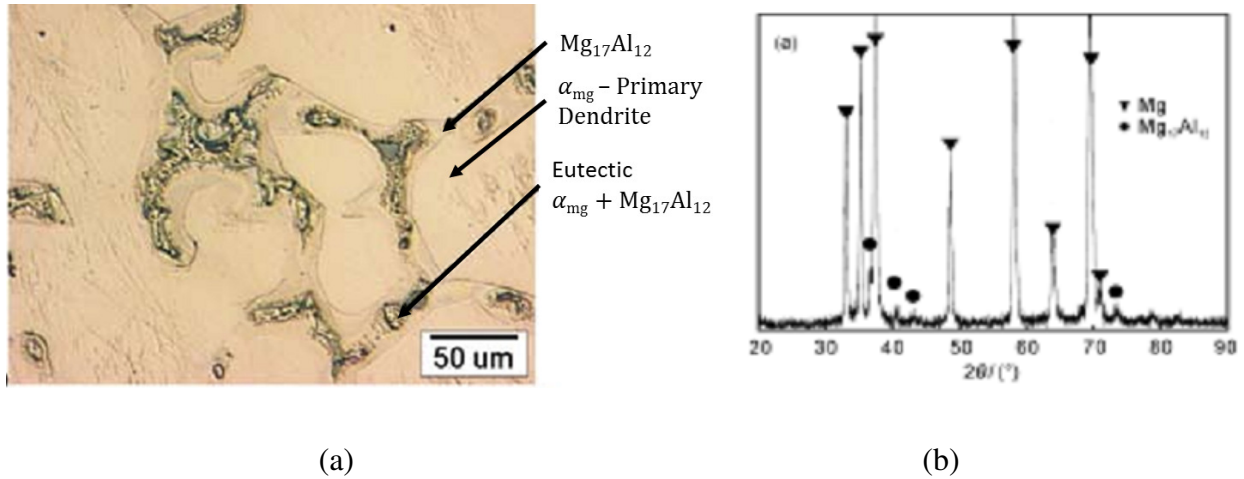


Figure 2.12. AM60 microstructural characteristics at a low cooling rate as-cast condition, (a) optical micrograph showing matrix grain structure (Mrvar et al., 2006), (b) XRD pattern (Wang et al. 2007).

### [2.5.1.3.2] Deformed

The high temperature deformation of AM60 increases the grain density and grain refinement from recrystallization. The alloy undergoes continuous dynamic recrystallization at elevated temperatures (375°C). This is seen in large strain hot rolling where the alloy grain density increases significantly as shown in Figure 2.12. The formation of new grains on the grain boundaries indicates the occurrence of dynamic recrystallization (DRX) during deformation under these conditions and the as-cast structure is converted to a wrought structure (Pérez-Prado et al. 2004).

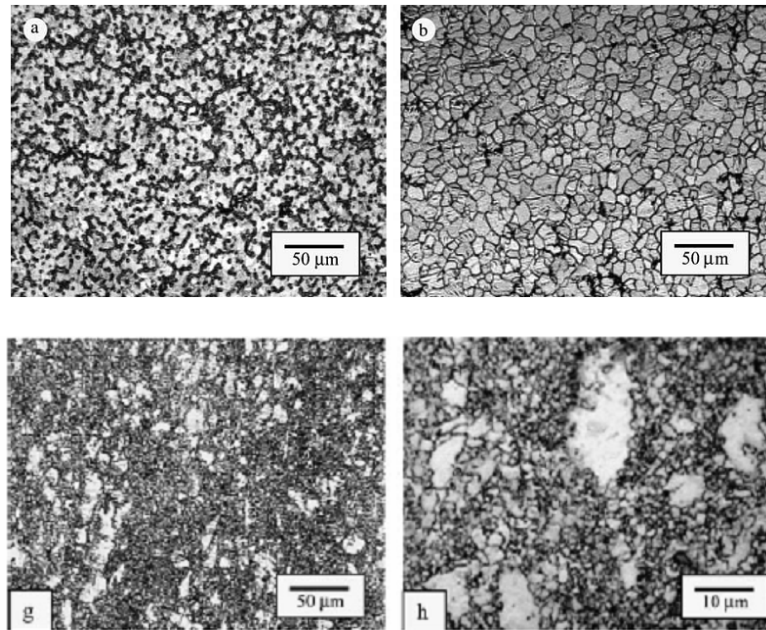


Figure. 2.13. Optical microstructures of AM60, (a) as-cast and (b) heat-treated at 450°C for 30 min (g, h) after rolling at 375°C with a thickness reduction of 80%. The micrographs were taken in the rolling plane (Pérez-Prado et al. 2004).

## [2.5.2] AZ91

### [2.5.2.1] Physical

AZ91 alloy composition in terms of mass percentages of different alloying elements and other physical properties are shown in Tables 2.3 and 2.4 respectively from the work of Bauccio (Bauccio, 1993). Corrosion resistance decreases with increasing Fe, Cu, or Ni content. More than 0.5% Si decreases elongation (Ricketts, 2014). The metal surface can go from a light white shine to a dark gunmetal grey depending on corrosion.

Table 2.4. Mass percentage composition of AZ91 showing maximum and minimum limits for the different alloying elements (Bauccio, 1993).

Element	Al	Mn	Zn	Si	Cu	Ni	Fe	Other	Mg
Percentage	8.3-9.7	0.13 min.	0.35-1.0	0.10 max.	0.30 max.	0.0020 max.	0.0050 max.	0.30 max. other	Balance

Table 2.5. Physical properties of AZ91 alloy in F (as fabricated) temper (Bauccio, 1993).

Density	1.81 g/cm <sup>3</sup>
Liquidus Temperature	595°C
Solidus Temperature	470°C
Coefficient of Linear Thermal Expansion	26 µm/m.K
Thermal Conductivity	72 W/m.K

A thermal diffusivity value of 39.0 mm<sup>2</sup>/s was obtained for AZ91 from equation (2.7) by utilizing the thermal conductivity and density values from Table 2.5 and a specific heat value of 1.02 J/g\*t from Ricketts (Ricketts, 2014)

As with AM60, minimal information on parameters such as change in electrical resistivity and thermal conductivity as a function of temperature, and surface conductivity was available for AZ91 alloy in the literature. As a result, experiments to obtain change in resistivity as a function of temperature were performed in support of the UPJ studies.

### [2.5.2.2] Mechanical

The mechanical strengths of AZ91 alloy in F temper condition are shown in Table 2.5. Strain rate sensitivity was found to be a variable parameter as a function of temperature as shown

in Figure 2.13, increasing with higher strain rates. These temperatures were lower, but the strain rates were comparable to those present in the UPJ process.

Table 2.6. Material properties of AZ91 alloy in F temper condition (Bauccio, 1993).

Tensile Strength	230 MPa
Tensile Yield Strength	150 MPa
Elongation	3% in 50mm
Compressive Yield Strength	165 MPa
Poisson's Ratio	0.35
Elastic Modulus	45 GPa

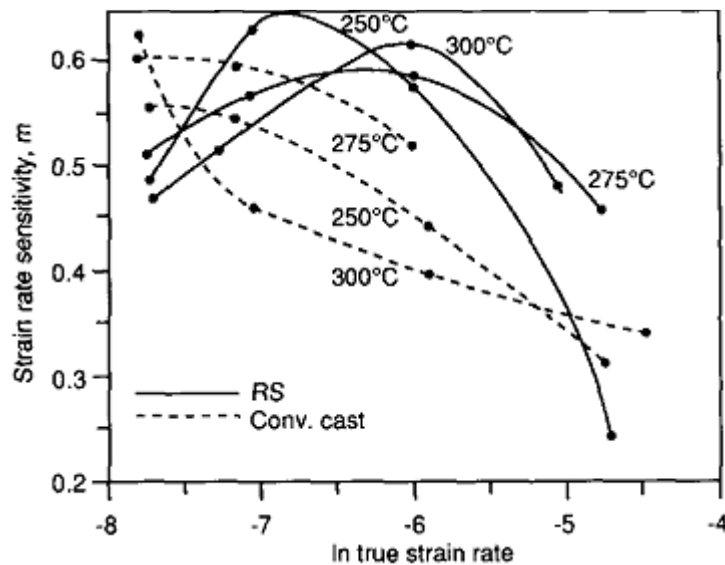


Figure 2.14. Strain rate sensitivity versus strain rate curves at different temperatures for conventionally cast and rapid solidification (RS) AZ91 alloys (Solberg & Tørklep, 1991).

Increasing temperature increased the tensile strength (report as ‘Rm’) up to 300°C, while deformation energy (DE) decreased at all temperatures, as shown in Figure 2.14. From this data, the optimal temperature for deformation of AZ91 was suggested between 250°C and 300°C in order

to increase tensile strength. This could have optimal material characteristics at this temperature. However, strain rate sensitivity increases with strain rate, implying a low compression rate would be preferable for AZ91.

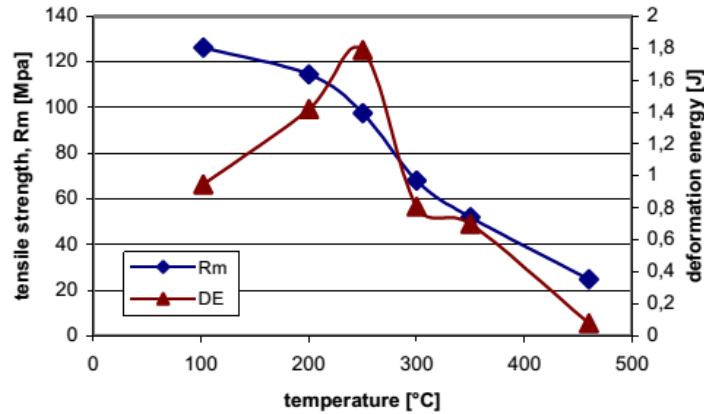


Figure 2.15. Comparison of tensile strength (Rm) and deformation energy (DE) versus temperature for AZ91 alloy (Čížek et al. 2006).

### [2.5.2.3] Cast Microstructure

AZ-series Mg cast alloys with high content of Al normally contain large volume fraction of  $\beta$ -Mg<sub>17</sub>Al<sub>12</sub> precipitates which form during solidification. It is generally considered that the presence of these particles on grain boundaries will have detrimental effects on workability and subsequent mechanical properties of AZ type Mg alloys (Čížek et al. 2006).

#### [2.5.2.3.1] Undeformed

The optical microstructure of the cast AZ91 alloy into steel and sand cast moulds are shown in Figure 2.15(a,b). The microstructures exhibits a typical dendritic microstructure consisting of dendritic  $\alpha_{Mg}$  matrix and  $\beta$  Al<sub>8</sub>Mn<sub>5</sub> phase crystallized at the grain boundaries (Kumar et. al., 2003.

Zhu et al., 2010). In comparison to AM60, higher volume fraction of  $Mg_{17}Al_{12}$  is present (Braszczyńska-Malik, 2011).

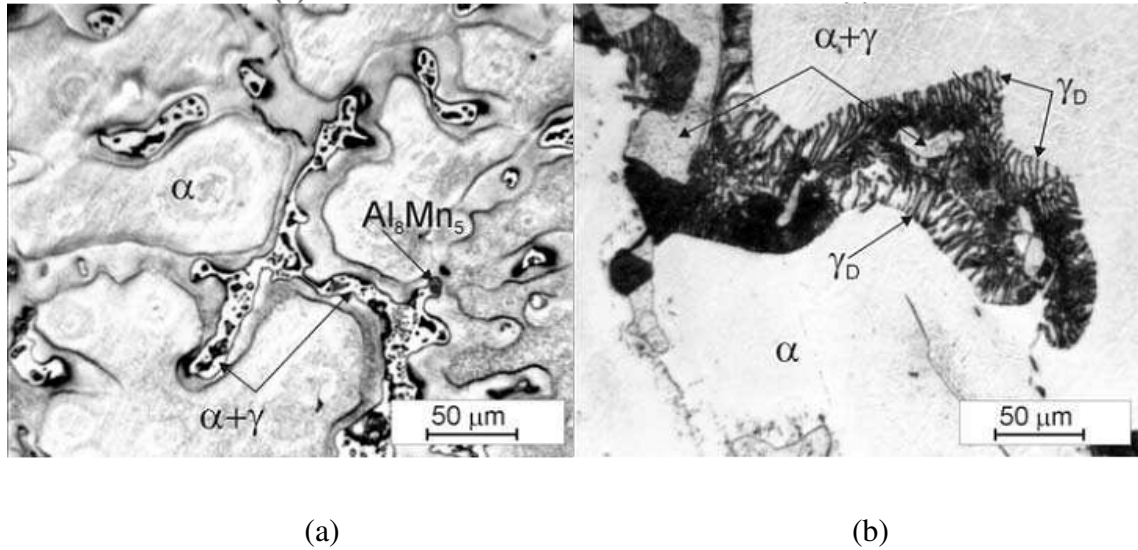


Figure. 2.16. AZ91 microstructural characteristics in (a) an as cast steel mould and (b) a sand cast mould. The  $\gamma$  are discontinuous precipitates (Braszczyńska-Malik, 2011).

#### [2.5.2.3.2] Deformed

Under deformation from an equal channel angular pressing at 325°C, the microstructure of AZ91 increased in grain density as shown in Figure 2.16. The original microstructure of AZ91 shows large dendrite-like grains, while the new grains indicates the occurrence of dynamic recrystallization (DRX) during deformation at these conditions as the as-cast structure was converted to a wrought one.



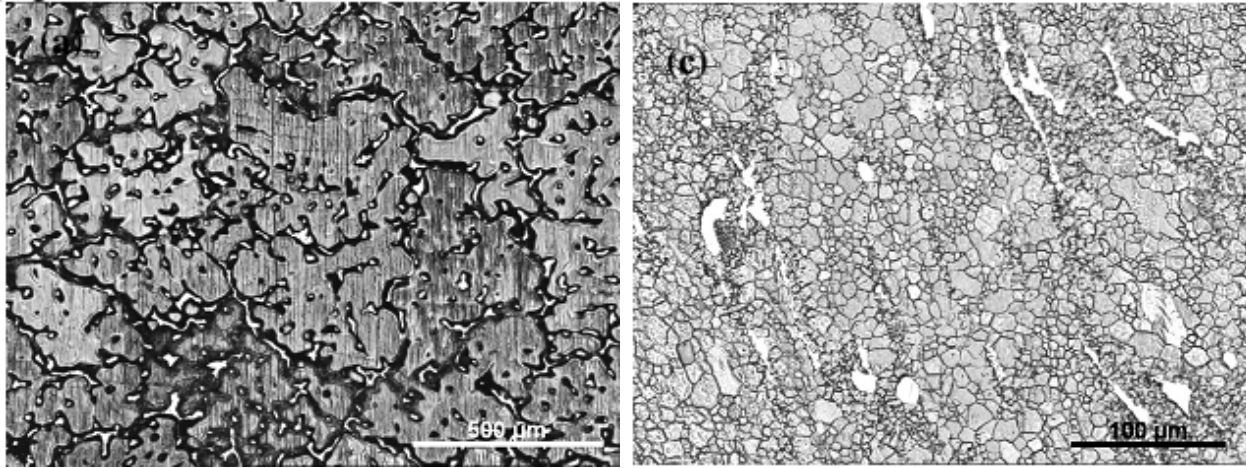


Figure 2.17. Optical microstructures of AZ91 (left) before deformation and (right) after 6 passes of equal channel angular pressing at 325°C. (Chung et al. 2009)

## [2.6] Summary

This chapter presented a review of literature on relevant topics related to the UPJ process and other related manufacturing processes such as spot welding. Various process characteristics and parameters were reviewed. Specifically, the electrical resistance heating and the large strain uniaxial plastic compressive deformation processes were extensively reviewed in terms of the associated parameters. Lastly, the physical, mechanical and microstructural characteristics and properties of cast AM60 and AZ91 magnesium alloys were reviewed from published scientific papers. It is clear from this review that many physical and mechanical properties as a function of temperature are not readily available for the two alloys in the literature. In fact, electrical resistivity data for AM60 and AZ91 alloys as a function of temperature were determined as part of this thesis (see Chapter 5.2). The mechanical properties at high temperatures and strains rates are also limited to low strains in the literature compared to the observed strains in

the isothermal compression and UPJ experiments.



## **Chapter 3. Design and Development of a UPJ System**

This chapter presents details of the new experimental UPJ system that was developed as part of the objectives stated earlier in Chapter 1. This system was utilized to study the UPJ process characteristics to carry out studies towards the other objectives of this research work.

### **[3.1] Design Objectives and Requirements**

Design and development of a new UPJ system was initiated as part of this thesis work. The general design objectives for this UPJ system were, (i) to identify, measure and control as many critical UPJ process variables as possible within the constraint of time and budget for the system as well as resources at McMaster, (ii) to purchase and utilize used or refurbished equipment and components as much as possible to reduce costs without compromising the control and measurement aspects, as noted above, (iii) to carry out fabrication of many of the components in-house from raw materials using the facilities of the Mechanical Engineering Department's Project Laboratories, (iv) to minimize costs by selecting used resistance heating equipment in the low power consumption range, and (v) to carry out experiments safely in the high current (a sparking and fire hazard), high temperature and high speed mechanical test environment. The first objective was especially challenging (and novel) considering that two different commercial pieces of equipment, a resistance heating system of a spot welder and a servo-hydraulic mechanical test system were selected for integration to create the new UPJ system. More specific technical objectives were (i) to determine via separate experiments on the existing spot welder in the Department of Mechanical Engineering at McMaster, the current levels that were needed to

achieve maximum temperatures in the range of 350°C – 400°C in a period of 1-2 seconds for the two magnesium alloys being considered for the UPJ process, (ii) to have a repeatable UPJ process as recorded by applied current, current duration, applied displacement rates and displacement values to produce a good UPJ joint (that met the visual appearance and strength requirement), (iii) to allow flexibility in terms of choice of electrodes and test specimen geometry, and sequence and superposition of pre-loading, heating and mechanical loading process steps, (iv) to facilitate rapid specimen mounting and removal from the test system, and (v) to allow for observation of the deforming cylindrical specimen during the UPJ process, for experiments requiring access to the test specimen surface during surface temperature field measurements

In the following sub-sections, the design and development of the new UPJ system in terms its two principal sub-systems, heating and mechanical loading, is presented.

### **[3.2] Heating System Design**

#### **[3.2.1] Heating Method**

Different methods of heating were briefly investigated in the available literature. These were induction heating based dies, oxy-hydrogen torches, electrical induction, friction stir, and electrical resistance heating. Heated dies transfer heat to the protrusion through conduction and it was clear that this method would not be able to achieve the desired temperature range in 1-2 seconds. Electrical induction is an industrial method of heating metals. This method of heating would place induction coil around the test piece and likely interfere with specimen mounting and removal as well as with the compression loading process and temperature measurements using thermocouple and Infrared cameras. In addition, the method would require a high capacity power

source in order to heat rapidly. Oxy-hydrogen torches are used for welding magnesium but such a process was considered unlikely to provide well-controlled heating or temperature profile for the test piece and could burn or melt the surface. Friction stir welding was also eliminated as this process would involve heating the material under a rotating disk and was unlikely to produce uniform heating of the protrusion. Electrical resistance heating was considered superior to all of the above heating methods in that it is routinely used in spot welding where local rapid heating of a clamped work-piece, similar to the UPJ process, is involved. Spot welding machines are common in automotive assembly lines, and this method can be used to heat even steels to achieve melting temperatures. After careful consideration of the resistance heating based UPJ system and its efficient and affordable heating rates, this method was chosen for the present UPJ system. Table 3.1 below provides a comparison of strengths and limitations of the different heating methods.

Table 3.1. Comparison of different methods of heating a protrusion for the UPJ process.

	Simple Control System	Rapid Heating	Uniform Heating	Standard Industrial Equipment
Oxy-hydrogen	Yes	No	No	Yes
Heated Dies	Yes	No	No	Yes
Electrical induction	No	Yes	No	No
Friction stir	Yes	No	No	Yes
Electrical resistance heating	Yes	Yes	Yes	Yes

Electrical resistance heating could be carried out by passing current between the top electrode (in contact with the protrusion) and the bottom cast plate in contact with the lower electrode. It was envisaged that a high current flowing through the protrusion would heat the protrusion along its entire length. UPJ, unlike spot welding, is a solid state mechanical joining process and does not require melting temperatures to be reached. It is to be noted that the cross

section involved in UPJ is much larger than that in spot welding, however aluminum welding goes to much higher temperatures than that needed for heating magnesium, resulting in comparable electrical currents. Standard spot welding control systems can reach in excess of 50 kA and have standardized, accurate, and certified control systems. An in-house spot welder, based on resistance heating, was utilized to conduct independent experiments to assess the heating capability of resistance heating method for the two magnesium alloys of interest in this study and the chosen test specimen geometry. These experiments also confirmed the feasibility of electric resistance heating method for UPJ process.

Based on the above in-house spot welder study, a Mid-Frequency Direct Current (MFDC) spot welding machine was chosen amongst the various available. This choice provided the fastest and most uniform heating for a protrusion using standard assembly line equipment.

### **[3.2.2] Components of the heating system**

The electrical heating setup was composed of a MFDC transformer, flexible copper shunts, and two electrodes. As the lower electrode had a significantly larger contact area, risk of melting at that location was lower, and therefore, a copper electrode, a more effective and less costly material, was used. A more expensive pure molybdenum electrode was used as the top electrode for resistance heating. This same molybdenum electrode was also used as a punch due to its machinability and high strength for compressively deforming the protrusion during the upsetting phase. The electrode was machined to appropriate dimensions based on resistance heating and mechanical loading considerations.

The MFDC transformer has control and speed advantages over a standard AC welder, the

largest being passing current constantly through the protrusion instead of oscillating the current resulting in faster heating. From research and testing, the machine was designed to be capable of producing 15 kA for 1 second, a value nearly seven times the required power. The machine also uses standard weld control code, enabling multiple, precise, and standard welding control programs on a reliable system. Programs can provide constant (step) or increasing (ramp) current or voltage, providing several welding profiles (for example, see Figure 3.1, left). By incorporating multiple ramps, steps, and delays any standard electrical profile could be produced. The machine control interface was wired and connected to the actuator control system and treated like a standard spot welding hydraulic clamp system, closing a relay to activate the clamping process.

A water chiller system was also installed with the equipment (Figure 3.1 right) as per the new installation requirement of a recirculating chilling water system instead of the tap water. A hydraulic loop, linking the MFDC transformer, the control unit, and the servo-hydraulic pump was created, providing cooling water to all three devices.

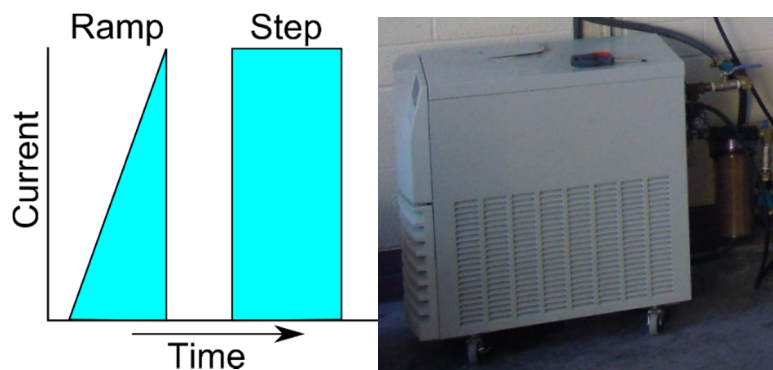


Figure 3.1. Current profiles produced by the MFDC transformer (left). Water chiller used in the setup (right).

### **[3.3] Mechanical Loading System Design**

Prior to the selection of a mechanical loading system, various possible methods of loading the UPJ components in compression to large strains were reviewed in the literature, for their strength and limitations. These included pneumatic rams, hydraulic rams, servo-controlled hydraulic rams, screw jacks, and servo guns. A pneumatic and hydraulic ram would use air and oil pressure respectively to compress the protrusion rapidly. Control of the pneumatic system was considered difficult especially when large forces are involved. As the compression rate was to be controlled, this did not appear as a good option. Screw jacks could be controlled to compress at the desired loads and rates, however, as the protrusion was to be rapidly compressed from rest, the gearing system would be unable to compress the protrusion at a desirable acceleration rate. A servo gun, a ball screw ram with several planetary gear clutches, would be capable of providing the speed and compression loads required and would likely be used in an industrial setting. However, due to the cost, complexity, and unfamiliarity with the servo gun, this method of loading was also not considered.

In the end, a computer-controlled servo-hydraulic ram, commonly used in compression and tensile testing machines, appeared to be most suitable for use with the UPJ process. However, new servo-hydraulic mechanical test systems were quite expensive and well beyond the equipment budget available. Therefore, to keep the costs down, a used computer-controlled servo-hydraulic mechanical test system was selected. This equipment was purchased in a refurbished form with a new test software and other hardware upgrades. This equipment was integrated with the resistance heating system to compress rapidly heated UPJ parts (but largely the protrusion) at a controlled rate to a pre-determined distance. This test system is a single hydraulic actuator system where the

actuator is located at the base of the two-column test frame with a maximum displacement rate and load shown in Table 3.2. The load cell was moved from the cross bar to this bottom actuator so that it could be distanced from the resistance heating system located at the cross-bar, a source of potential electromagnetic signal noise. Figure 3.2 shows a photograph of the test system and its principal components (except the computer interface).

A tensile testing machine with a fixed cross bar was chosen in order to mount the transformer close to the testing area, to reduce copper shunt length and to improve access to the testing area. The testing area is composed of two shunts, the top copper mount, the top electrode, the bottom electrode, the surface plate, and the rear shunt as shown in Figure 3.3. This design was made for simplicity, ease of assembly, and easy access that was later used when a metal shielding box surrounded the testing area. This large open frame required a long bar between the load cell and testing area to prevent signal noise from interfering with the equipment. The long distance between the ram and the testing area resulted in skewed compression, fracturing the protrusion. To counter this the testing area was fitted with two ground steel bars and bushings to prevent horizontal motion (Figure 3.4).

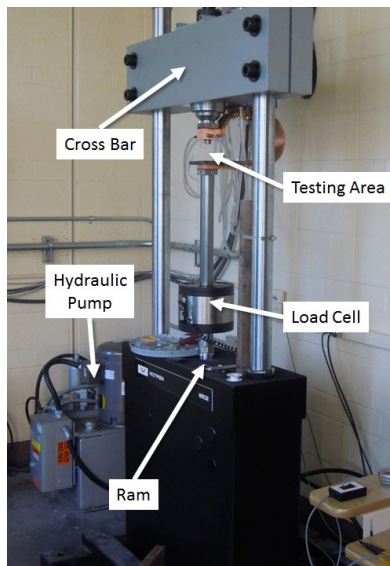


Figure 3.2. Loading system.

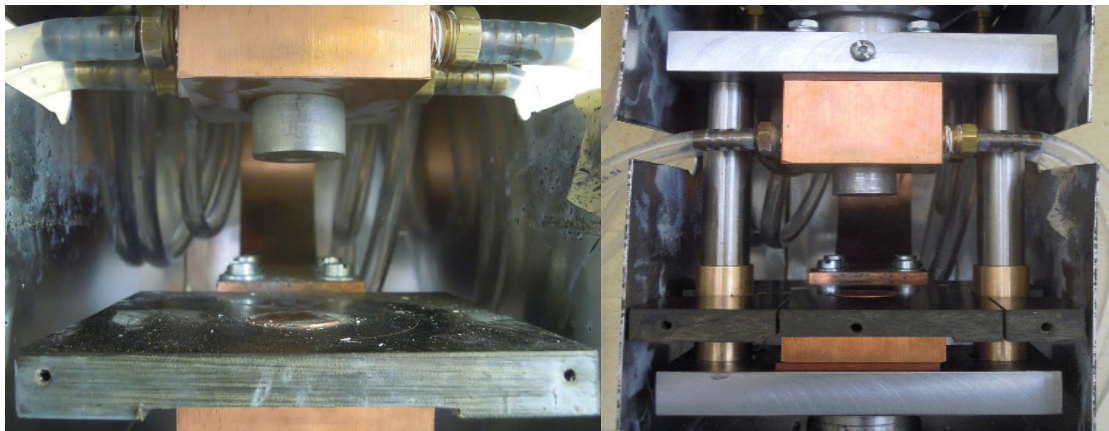


Figure 3.3. The original test setup (left). The setup was fitted with a punch guide system consisting of two vertical bars and bushings to prevent non-axial sliding (right)



Table 3.2. Mechanical loading system capabilities

Maximum load	100 kN
Maximum ram displacement	150 mm
Maximum compression rate	44 mm/s
Maximum UPJ specimen height	125 mm

### [3.4] Integration of Heating and Loading Systems

Key difficulties in the integration of a load system and a resistance spot welder into one machine were differences in the two control system programs, signal noise, power sources, and space considerations. Spot welding commonly uses a hydraulic ram with a set oil pressure to press the electrodes into the metal before welding. Due to the high currents, the welding circuit is also commonly as small as possible in order to reduce electrical resistances across the circuit. Different orientations of the transformer, load cell, and ram were tested, however, the high electrical noise from the transformer made distancing the transformer from the servo-ram and the load cell a high priority. Load cells in servo presses are commonly mounted to the stationary cross bar but they were instead mounted to the actuator to distance the load cell from the transformer. Several unique brackets were made to mount the transformer to the cross bar.

Despite the distance separation from the MFDC transformer, signal noise produced by the transformer was found to interfere with the load cell and Linear Variable Differential Transducer (LVDT) that measure load and displacement respectively. The high magnitude and rapid increase in the current passing through the resistance heating circuit caused an electromagnetic signal that induced current and voltage in signal wires, disrupting the actuator process controls. To reduce the effect of the high current pulse on the actuator control system, the UPJ area was surrounded in a

Faraday Cage, a common technique in noise reduction. The electromagnetic field was reduced by surrounding the electrical resistance area in a conductive aluminum box, surrounding the load cell in a metal can, thick aluminum plates around the LVDT, and wrapping the signal wires in aluminum foil. As well, a long cylindrical rod as an extension of the hydraulic piston was used to further separate the load cell from the UPJ area.

The aluminum sheet metal in the two-part UPJ unit vibrated in the event of a breaking electrical circuit as the aluminum resisted the changing magnetic field. Some signal noise was still present even after the implantation of the electromagnetic shielding and other design modifications. An example of the heating process where the ram was held at a fixed position is shown below in Figure 3.4. Electrical resistance heating produced electromagnetic noise after 0.35 seconds. The signals shown are the input position signal from the LVDT and the output voltage signal to the servo-hydraulic ram in order to maintain position. This noise signal is also very small, on the order of 0.2 mm over a protrusion 14 mm long on a 4 mm thick plate. This noise signal was considered insignificant in this experiment as it did not affect the UPJ process. However, if simultaneous heating and compression was to be implemented on this machine, the noise may become a more prominent issue with the equipment and require more shielding or redesign.

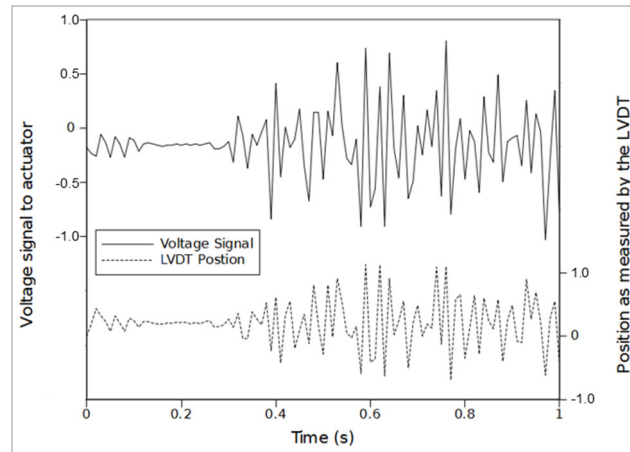


Figure 3.4. Voltage to the servo-hydraulic ram and position measured by the LVDT. The ram was controlled to remain fixed during heating that began at 0.3 seconds.

A final key complication in the system was the implementation of two separate power systems required. The servo-hydraulic power pack required 230V 18A three phase while the MFDC control system required 600V 100A three phase, requiring two power systems to provide power. This power source issue added complication in finding a suitable experimental setup location.

### [3.5] Safety Considerations

Safety was an important element of the UPJ system as it involved high temperatures from a high power resistance heating system and large rapid forces from a servo-hydraulic ram. The resistance heating system produced a maximum of 9 volts, a voltage typically incapable of producing an arc. This prevented the system from welding or producing electrical heat without the electrical circuit being closed. This low voltage also prevented risk of electrical shock. However, burning did occur in some test cases during the equipment commissioning and the cause of arcing

was determined and addressed. To attenuate the risk of injury from sparks and/or liquid metal spray, an enclosure around the testing area, the Faraday cage (Figure 3.4) was added to the system. In order to start the UPJ process, the user must press the control button on the heating system. This sends a signal to the actuator to clamp onto the protrusion prior to heating. The button to control the heating system was located more than 2 m away from the testing area to prevent activation of the equipment during setup. In the unlikely event of a magnesium fire, a Class D fire extinguisher was positioned beside the equipment.

### **[3.6] UPJ System Process Limits**

The UPJ process had three key limits that consisted of (i) minimizing process time to form a single joint, (ii) no burning or melting of the protrusion, and (iii) creation of a strong bond between the casting and the upper plate with a hole, by filling of the hole gap by material flow during upsetting as in Figure 3.5. An incomplete gap can potentially cause relative sliding between the joined components under in-service conditions. Minimizing process time to form a single joint was to meet the automotive assembly line demands and process efficiency. The protrusion could not melt or burn during the UPJ process to meet safety considerations. Melting and burning would not only provide a fire hazard, but also damage the electrodes used in this process.

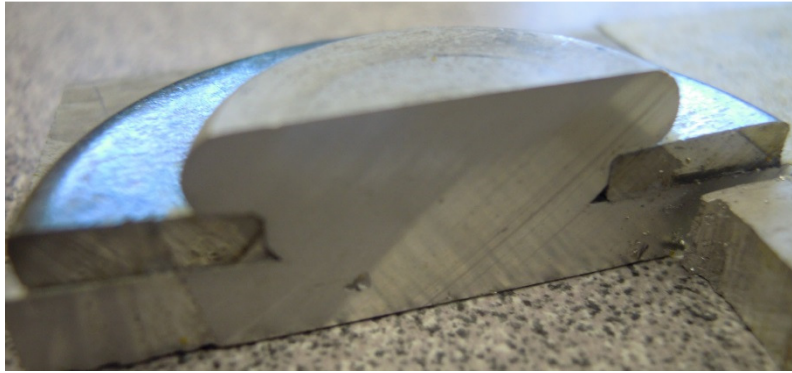


Figure 3.5. A sliced view of a UPJ sample after upsetting showing an extensive shape change of the cylindrical protrusion in the form of a mushroomed head.

The process limits on the equipment consisted of a high maximum current, a maximum applied load of 100 kN, and a rapid maximum compression rate over a 300 mm maximum travel distance. These process parameters are far below industrial limitations that can provide currents in excess of 60 kA and provide higher compression rates and loads through the use of a servo gun or a larger hydraulic servo. The equipment process limits were selected around research needs, budget, power and equipment. The servo hydraulic press was a common material testing machine that was specified with a maximum load of 100 kN. The transformer was specified in order to produce enough current and duration to heat the protrusion to deformation temperatures more than seven times over. The equipment at present is capable of heating and compressing an 11mm wide and 14mm long protrusion, but could theoretically (not yet tested) heat magnesium protrusion up to 20 mm wide and 40 mm long to forming temperatures or heat aluminum alloy protrusions.

### **[3.7] UPJ System Process Inputs and Outputs**

Parts to be joined were heated and then compressed in a well-controlled manner using the new UPJ system. The input data consisted of applied current, current duration, displacement rate

and displacement whereas the output consisted of load and corresponding displacement data during the large deformation (or upsetting) of the protrusion, and a visual assessment of the UPJ joint quality after the test. Load was measured by a 100 kN load cell and displacement was measured by a LVDT. Both of these devices, as well as the ram's servo valve, were susceptible to signal noise from the electrical resistance system. Other parameters such as final diameter of the protrusion, were also measured. Further, as the quality of the joint was a key parameter, a qualitative scale of 1-10 was devised to quantify the joint quality as described in the next chapter.

### **[3.8] Summary**

This chapter presented details of a new, and rather novel, UPJ system that was designed and built at McMaster University, as part of this thesis work. Many of the design objectives, as outlined earlier, were met and exceeded. A number of revisions to the original design were made during the commissioning stage (for example, electromagnetic field noise and isolation of resistance heating and loading system components and guide system for the punch motion). In fact, the system in its present form is capable of easy modification to implement other hot joining methods.

The present UPJ method, based on a custom equipment developed at McMaster, involves integration of a modern instrumented high speed servo-hydraulic mechanical test system and a commercial spot welding equipment for local heating and consists of a transformer, a chiller, a controller and electrodes. This method utilizes (i) a small pre-load in the elastic and small strain plastic range to establish contact between the electrodes and protrusion, (ii) pre-heating of the protrusion through resistance heating, and (iii) forming of the part while the current is switched off.

The experimental procedures associated with the use of the current UPJ system as well as other test methods utilized in this thesis are described in the next chapter (Chapter 4). The results from the UPJ system and from other experiments are presented in Chapter 5.

## **Chapter 4. Experimental Procedure**

Custom equipment developed at McMaster integrates a modern instrumented high speed servo-hydraulic mechanical test system and a commercial spot welding equipment for local heating and consists of a transformer, a chiller, a controller and electrodes. This method utilizes (i) a small pre-load in the elastic and small strain plastic range to establish contact between the electrodes and protrusion, (ii) pre-heating of the protrusion through resistance heating, and (iii) forming of the part while the current is switched off.

This chapter presents further details of experimental procedure associated with the McMaster UPJ system. Also, details of the die casting process to produce the plate component with a protrusion component in AM60 and AZ91 magnesium alloys are provided. Casting process has a bearing on the resulting microstructure and mechanical properties of the alloys and therefore on the UPJ process. Further, details of the temperature measurements during the resistance heating process from thermocouple inserted within the protrusion as well as surface temperature measurements using an infra-red (IR) camera system are provided as a way of establishing a link between energy input, applied current and current duration. Furthermore, details of the isothermal uniaxial compression experiments on cylindrical A60 and AZ91 specimens are provided. Lastly, the procedures associated with assessing test-to-test repeatability of experiments, selection of two separate experimental test matrices for UPJ experiments, and post-test characterization of joint strength are provided.



## **[4.1.] UPJ System Details**

### **[4.1.1.] Process Steps and Sequences**

As mentioned earlier, the UPJ process developed at McMaster University involves pre-heating of the protrusion by passing electric current through the protrusion with a controlled current profile to heat the protrusion followed by compression of the protrusion at a fixed compression rate to a set distance (see Figure 4.1). Heating was commonly a ramp function increasing from 0 value to a fixed maximum current over a duration. The maximum current is referred to as the peak current at the end of the ramp throughout the thesis. By changing the peak current and the current duration, the average temperature of the protrusion could be varied (see Chapter 6.2.1 for temperatures attained). Prior to the pre-heating process, the protrusion was lightly compressed. This, akin to clamping load during a spot weld, helped improve electrical conductivity between the electrode and material. Reducing clamping load below a certain minimum resulted in poor electrode contact with the protrusion, and consequently, a significantly smaller localized area of contact in the form of surface asperity contact of the electrode and protrusion. This typically caused melting and/or burning of the top surface of the magnesium protrusion and had to be avoided. Application of a small pre-load could plastically deform the protrusion asperities so as to increase the contact area and more uniform current transfer could take place across the electrode and the protrusion. After pre-heating, the protrusion was compressed after a small time delay. However, this feature of the test system was not explored in this research and the delay was set to zero for all experiments. The extent of compression of the protrusion was governed by compression rate and compression distance. Also, the UPJ system in its current configuration,

could allow the current to be passed through the protrusion during the compression step to provide additional heating. However, this was also not explored in this research. The electrode was also utilized as a mechanical tool (i.e., a punch) to compress and upset the protrusion to create the UPJ joint. After the protrusion was compressed, the electrode was held in position before it was retracted to complete the UPJ cycle.

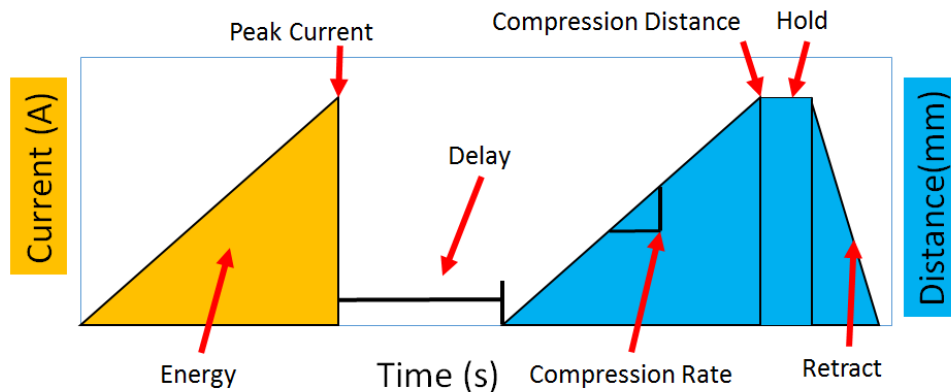


Figure 4.1. Applied current and electrode (punch) displacement profile of UPJ process.

#### [4.1.2] Die Cast Protrusion Parts for UPJ Study

Plates with cylindrical protrusions were die cast from AM60 and AZ91 magnesium alloys. Two protrusion locations of identical protrusion shape on the cast plate part were considered for UPJ process in order to tests post-UPJ joints in ‘Lap Shear’ and ‘Cross Tension’ (see Figure 4.2). It is to be noted that the location of the protrusion on the plate did not have a bearing on the UPJ results. All original cast surfaces of the protrusion (top and bottom flat surfaces and cylindrical surface) were retained in the UPJ experiments. The outer cylindrical surface was not machined to retain the original fine grain structure of the surface region.

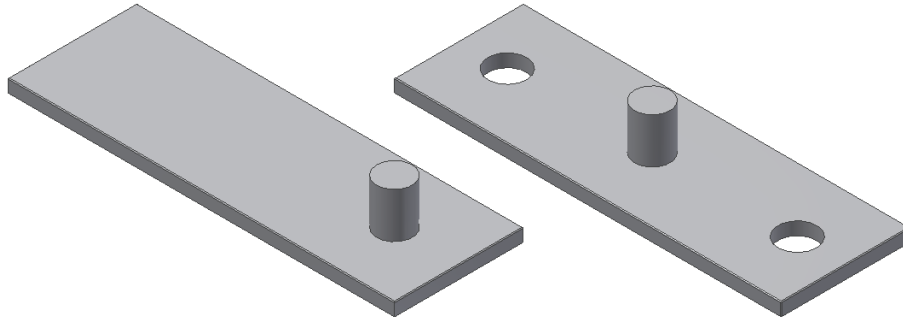


Figure 4.2. Die cast test sample geometries for creation of UPJ joints. The joints were produced and subsequently tested in lap shear only (left).

#### **[4.1.3] Part Assembly and Electrode Surface Preparation**

The 11 mm diameter protrusion on the die cast part was fitted with a 2.2 mm thick sheet of aluminum 6061 with a 14 mm hole. The hole in the aluminum sheet was drilled, reamed, and lightly deburred. The sheet was 40 mm by 40 mm and loosely placed on the protrusion (see Figure 4.3(a)). For lap shear tests, the sheet was longer, 40 mm by 120 mm (not shown). The electrodes were then polished (Figure 4.3(b)) and any debris removed (Figure 4.3(c, d)) prior to placing the specimen into the UPJ system (Figure 4.3(e)). The UPJ process was then performed.

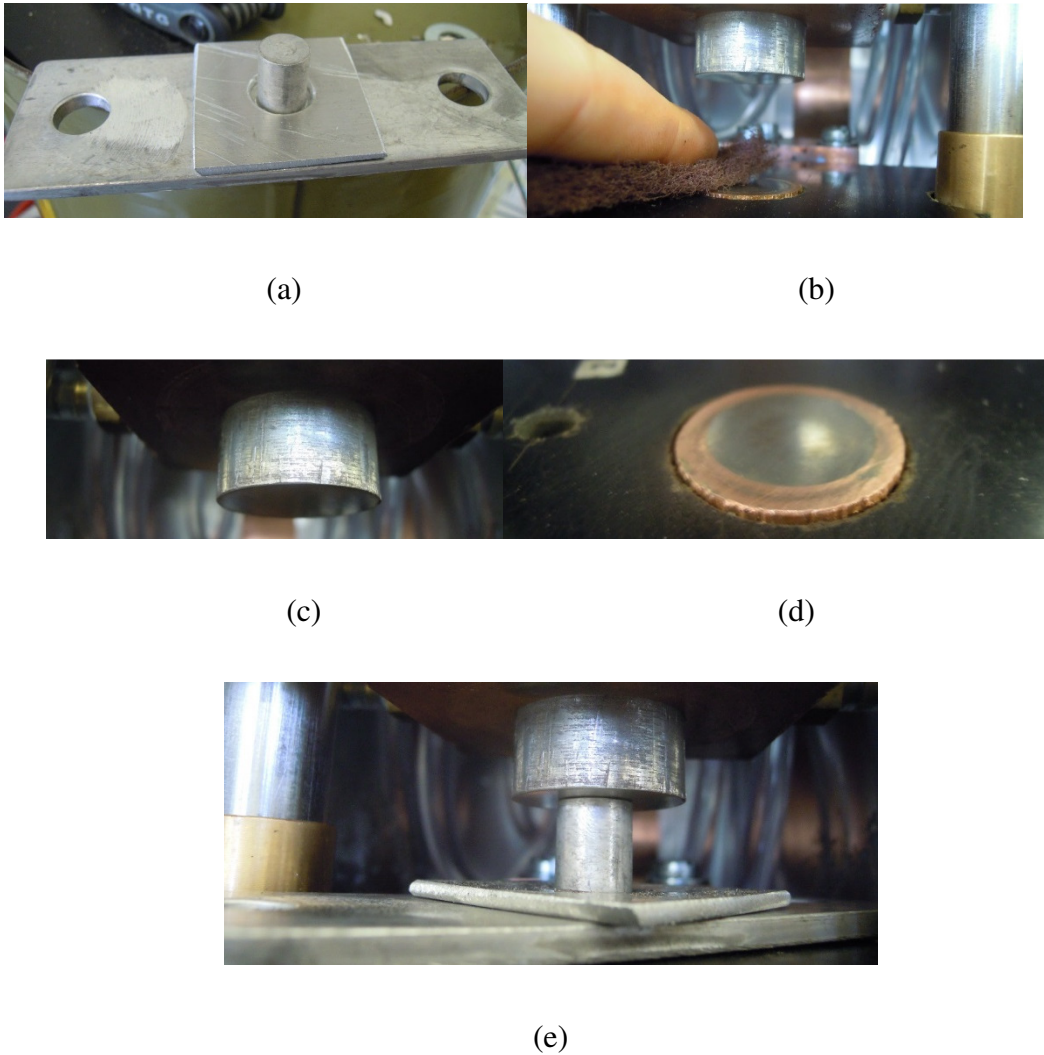


Figure 4.3. Sample preparation for UPJ, (a) A lap-shear protrusion sample with a mounted aluminum plate, (b) Polishing of the electrodes with Scotch Bright, (c) top electrode, (d) bottom electrode as inspected for debris, (e) pre-loading of protrusion prior to heating.

#### [4.1.4] Current Squared Time Profile and Maximum Current Applied

As mentioned earlier, the protrusions were heated via resistance heating by passing current between the top and bottom electrodes. Current was applied to the protrusion commonly through

a ramp function from 0 to a maximum current over a certain duration. Increasing the maximum current or duration were known to increase the amount of energy entering a protrusion, and in effect the temperature, according to Equation 2.1 from Chapter 2. In order to account for different maximum currents and durations, a new parameter, Current Squared Time Profile (CSTP) was defined. The CSTP variable used the maximum current applied and the duration of applied current to heat the protrusion. This variable can be expressed by the following equation:

$$CSTP = I_{\max}^2 t \quad (4.1)$$

where CSTP has units of  $\text{kA}^2\text{-s}$ . For constant CSTP tests, equation (4.1) was expressed as follows:

$$CSTP = I_{\max 1}^2 t_1 = I_{\max 2}^2 t_2 \quad (4.2)$$

where  $I_{\max 1}$  and  $t_1$  and  $I_{\max 2}$  and  $t_2$  refer to two equivalent CSTP profiles.

#### **[4.1.5] Heating Experiments**

Separate heating experiments were performed while carrying out temperature measurements in the protrusion region of the sample. This was to assess heating characteristics such as temperature distribution and heating rates as a function of UPJ process parameters. In order to measure the protrusion temperature, thermocouples were mounted internally and externally on the protrusion. Alternatively, an infrared camera were used in a separate experiment to obtain surface temperature field data. No forming (i.e., plastic deformation) of the protrusion was performed in these experiments.

##### **[4.1.5.1] Thermocouple-Based Experiments**

By press-fitting a sheathed thermocouple into a very small horizontal hole in the protrusion

(hole axis being perpendicular to the protrusion axis) coated with a thermally conducting paste, the internal temperature of the protrusion could be measured during heating (Figure 4.3(a)). Another setup used thermocouples welded to the surface of the protrusion (Figure 4.3(b)). Thermocouples were mounted at three different locations; 1 mm from the top of the protrusion, in the middle, and at the bottom of the protrusion corresponding to 1 mm from the upper surface of the bottom cast plate (Figure 4.3(c)). A set of experiments were performed where applied current was steadily increased over a set of time durations. Another set of experiments was conducted by changing both the duration and magnitude of the current in order to maintain a constant CSTP. This was to investigate how the CSTP and maximum current affected the protrusion temperature prior to forming.

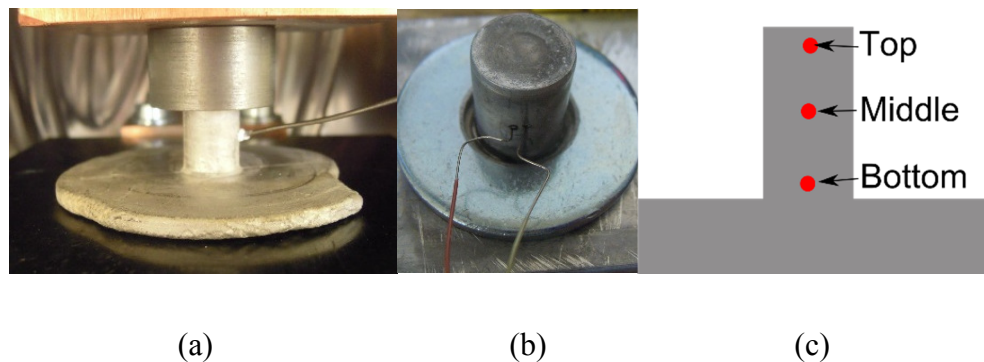


Figure 4.4. Thermocouple mounted inside a protrusion (a). Thermocouple welded to the surface of a protrusion. The thermocouples were mounted at three different locations (b).

#### [4.1.5.2] Infrared (IR) camera-based experiments

As the protrusion surface showed visual cracking during the UPJ process, and a large number of thermocouples could not be physically welded to the protrusion, an infrared camera was used in an attempt to directly observe the surface temperature distribution (as field data) during heating.

A FLIR E40 infrared camera from FLIR Corporation was located 1 m away from the experimental setup during heating. Also, the protrusion was coated in black soot in order to produce an emissive surface. Experimental matrix was kept identical to that for thermocouple-based measurements to enable a comparison of results from two very different methods. However, due to technical limitations of the equipment, the IR camera could only yield a video image of colour contour of the temperature field. The video was taken frame-by-frame and the ‘hottest’ location was identified as per the colour band. Unfortunately, the system did not provide a reliable digital temperature output at specific desired locations on the specimen.

#### [4.1.6] Current Profile Experiments

The most uniform current profile would be from the application of a constant current. However, this was found to cause burning and/or splatter on the top face of protrusion (Figure 4.5 (a,b)). Constant current was also found to cause the aluminum shielding to vibrate and the actuator would ‘jump’ and move when set to remain stationary.

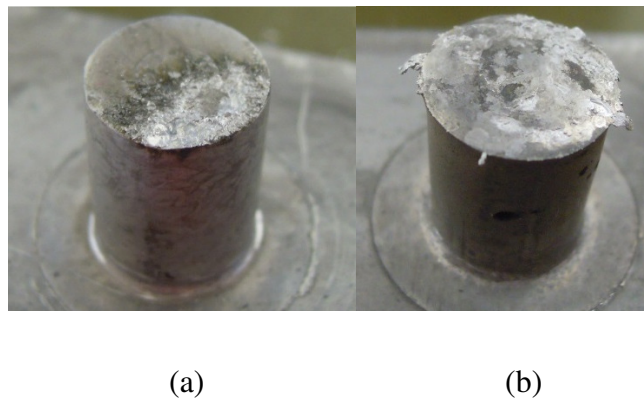


Figure 4.5. Photographs showing evidence of burning and melting on the top of a heated AZ91 protrusion. (a) A protrusion heated with 5kA for 1 second shows signs of magnesium burning on

the lower right side of the protrusion top. Craters and black burn marks are present. (b) A protrusion used for several constant current profile experiments. The top of the protrusion melted and sprayed outwards, solidifying rapidly and leaving tendrils on the top protrusion edge.

This was later corrected by use of a ramp function (see Chapter 4.1.1). The ramp function was found to prevent the noise, burning and damage present with a constant current function. The problem with the constant current function is attributed to the initial electrical surface contact resistance between the sheet metal and the electrode as seen in Chapter 2.2. The high current is thought to melt and burn the surface. This large current spike also produces large signal noise detected by the actuator resulting in the actuator moving away. This opening of the electrical circuit causes the hot magnesium to burn, forming and breaking the electrical circuit, producing more electrical noise. Through the use of the ramp function the surface is thought to melt and improves electrical contact between the electrode and the material over a more gradual (but still under a second) heating process.

#### **[4.1.7] UPJ Test Repeatability Experiments**

UPJ system was assessed for test-to-test repeatability using AM60 cast component. UPJ joints were obtained by conducting 5 identical experiments at the same process parameter settings. The tests were remarkably reliable and repeatable in terms of current-time and displacement-time history but there was varying outcome in terms of the quality of the joint (more on the assessment of joint quality in the next sub-section).



#### **[4.1.8] Experimental Test Matrices**

##### **[4.1.8.1] Experimental Test Matrix 1**

The first test matrix was developed to broadly assess the UPJ system capability and limits and resulting UPJ joint characteristics. This test matrix provided a semi-optimal UPJ profile for an AZ91 cast part where three key process variables, (i) CSTP, (ii) maximum current and (iii) compression rate, were evaluated. Additionally, compression distance could be varied to create UPJ joints with the top of the protrusion (above the aluminum sheet) in the form of a barrel shape at short compression distances or a thin disk at large compression distances.

##### **[4.1.8.2] Experimental Test Matrix 2**

The second experimental test matrix was in the form of a Taguchi orthogonal array to reduce the number of experiments and to assess the relative significance of each of the process variables. This was also constructed based on the 3 key variables, as noted above. In the Taguchi method, multiple parameters per experiment are changed, and fewer experiments are required to quantify the interaction between parameters. The first test matrix had three maximum currents, CSTPs and compression rates. Each experiment was repeated 3 times, originally requiring 27 experimental setups and 81 samples. The Taguchi orthogonal array matrix, on the other hand, required only 9 experimental setups and 27 samples, an obvious benefit as there are limited samples and experiments. A schematic of the Taguchi orthogonal array for this matrix is shown in Figure 4.6(a). Each value is independent, in that no two experiments can be directly compared to one another. In order to find a parameter trend, the mean of the three outputs at each compression rate value were obtained and compared (Figure 4.6.b). As not all input variables had strong effect

on the output value, noise in the data and experiment may be responsible for an inconclusive trend. Consequently, the signal to noise ratio, a term used to find the accuracy and precision of the value, was used. Standard deviation in the results was another quantity used to assess the output quantity. The Taguchi orthogonal array is optimal for output quantities such as ultimate strength of the material, a value that is quantitative and not subjective (or operator dependent). For a more subjective quantity such as ‘quality’ of the UPJ joint as an output parameter (see the next subsection for ranking of quality), noise and variability were expected in the data.

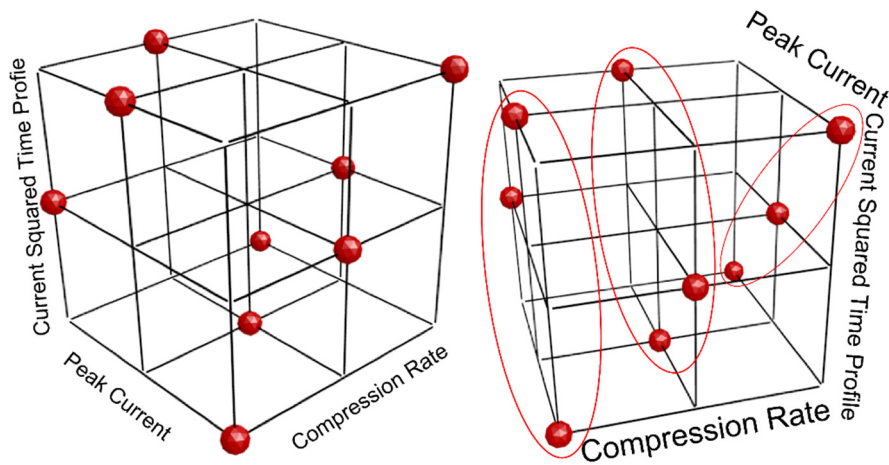


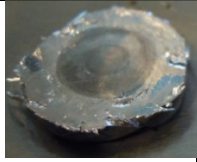









Figure 4.6. Taguchi orthogonal array for three process parameters each with three potential values (low, medium and high), (left) test locations marked with a red dot, (right) significance of compression rate on the output quantity by utilizing the mean of the three sets of values (circled in red).

#### [4.1.9] Observation and Assessment of UPJ Joints

The assessment of the UPJ joint quality was critical to the analysis of UPJ process. As improvement in the quality and elimination of crack formation on the joint was a primary focus, a

quantitative nomenclature was devised to assess the UPJ joint quality. Each joint was analyzed and given a value from 1 to 10 according to the crack location, shape, type, and density. The four main crack types were surface cracks which are cracks on the outer surface of the protrusion that have no visible effect on the strength or geometry of the protrusion, barreled surface cracks which are deeper into the barreled surface and change the geometry of the barreled surface, deep cracks which go into the center of the protrusion, and main protrusion cracks that form in the middle of the protrusion and affect the structural integrity of the joint. An ideal protrusion should have no cracks of any form and should be free of any surface blemishes. The ranking is summarized in Table 4.1.

Table 4.1. UPJ joint quality grading method.

Value	Crack Description	Example	Value	Crack Description	Example
1	Structural failure and large slanted cracks breaking through the protrusion. Indication of improper heating and/or structural failure of the main protrusion		6	1-2 cracks that are past the barreled surface and change the geometry of the protrusion	
2	Increased density of cracks breaking into the main part of the protrusion as well as horizontal cracks		7	8+ Surface cracks and cracks begin to enter main part of protrusion	
3	Pattern of deep cracks all around the periphery of the protrusion		8	3-7 Small surface cracks	
4	1-2 cracks breaking into the main part of the protrusion or a pattern of cracks part-way around the periphery of the protrusion.		9	1-2 Small surface cracks	
5	3-8 cracks that are past the barreled surface and change the geometry of the protrusion. No pattern to the crack formation		10 (best)	No cracks	

## [4.2] Isothermal Uniaxial Compression Tests

### [4.2.1] Mechanical test system

A separate servo-hydraulic MTS mechanical testing system was used to compress

protrusions inside an environmental chamber (Figure 4.7(a)). The machine was capable of a maximum of 26 kN of force at a compression rate of 1000 mm/minute. Due to machine DAQ system and sampling rate, compressions beyond 100 mm/minute were not performed. Inconel platens were ground and connected to the actuator to provide a flat compression surface (Figure 4.7(b)).

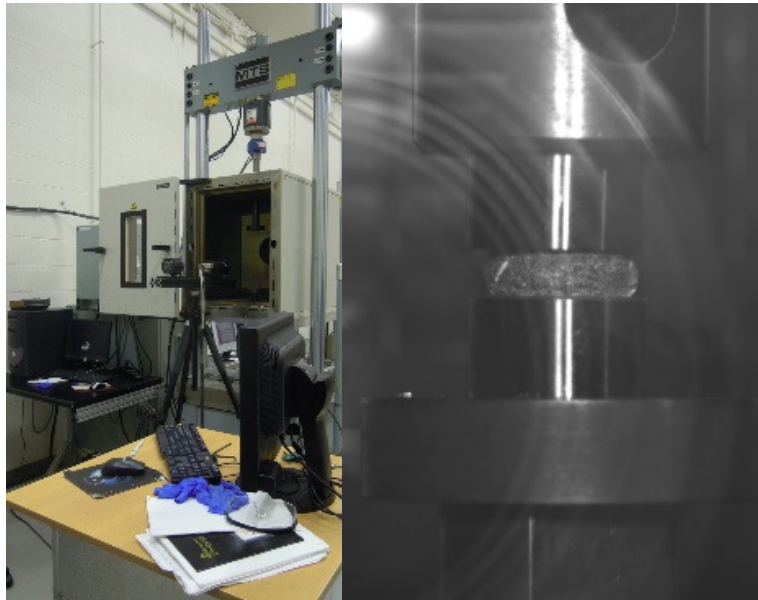


Figure 4.7. Isothermal uniaxial compression test set-up, (left) a photo of the servo-hydraulic MTS mechanical test system fitted with an environmental chamber, and (right) a view of a compressed test sample between two compression platens inside the environmental chamber.

#### **[4.2.2] Test Specimen Geometry**

Cylinders of magnesium were machined from cast lap shear samples in a collet lathe and machined to 14.0 mm long. As the material was from squeeze cast cylinders 11 mm in diameter and 0.5 degree taper, the outer cylindrical surface was not machined to retain the original fine grain

structure of the surface region.

#### **[4.2.3] Surface Strain Field Measurements**

Cylinders were painted with a black/white speckle (i.e., random) pattern as shown in Figure 4.8 in order to utilize a commercial optical strain-field measurement system (Aramis) based on digital image correlation (DIC) technology. The images of the deforming specimen were continuously acquired using the Aramis hardware (high resolution digital camera, frame grabber, and data acquisition system). The image were later analyzed using the DIC-based Aramis PIV software to obtain the strain field on the surface of the protrusion during compression.

#### **[4.2.4] Role of Friction in Uniaxial Compression**

The role of friction between the protrusion and the two compression platens on barrelling of uniaxial compression sample was also briefly investigated. Friction was indeed found to play a large role in the barreling, crack formation and deformation of a cylinder. To reduce friction, graphite paste and graphite paper was applied to the top and bottom surfaces of the cylindrical specimens.

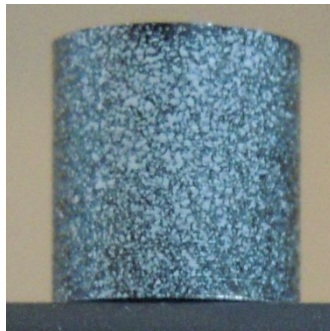


Figure 4.8. A cylindrical test sample with a speckle pattern applied to its surface for Aramis-based

strain field measurements.

#### **[4.2.5] Experimental Test Matrix**

The two primary parameters in the compression of cylinders are compression rate (or test speed) and temperature. Temperature was set at 300, 325, 350, 375 and 400°C. Compression rate was set to 1 mm/minute, 10 mm/minute, and 100 mm/minute. All protrusions were compressed from an initial height of 14 mm to a final height of 4 mm. Cylindrical samples were placed into the environmental chamber located on the MTS test system between the two compression platens. The chamber was heated to a set temperature and, upon reaching temperature, was left for 20 minutes to ensure the samples and the air temperature were the same. The sample was lightly compressed (30-100N) to establish uniform contact between the two platens and the test specimen before the compression process began and the Aramis strain measurement system was engaged. The load versus displacement traces were continuously recorded for each test as per the above process conditions. After completion of the test, the sample was removed and replaced with a new sample to continue testing.

#### **[4.2.6] Observation and Assessment of Test Specimens**

Data collected for each test sample included original geometry, test temperature, compression rate, continuous load versus displacement data, video images of the test sample during the test and crack geometry on the specimen. Load versus displacement data was converted into true stress versus true strain using standard equations. Trends between temperature, compression rate, materials (AM60 and AZ91) and surface roughness were compared. Video footage of the sample compressions was analyzed to obtain compression distance at the onset of

crack formation. Additionally, barreling of the samples was analyzed by comparing barrel profile measurements. However, no barreling correction was applied to the true stress-strain curves. See Figure 6.1 in Chapter 6.

#### **[4.3] Post-UPJ Joint Strength**

Lap shear UPJ joints were tested at room temperature in a uniaxial tension to assess their performance in tensile shear mode of deformation. The test set-up, utilized a servo-hydraulic MTS test frame as shown below in Figure 4.9. The samples were pulled at a constant displacement rate of 10 mm/minute to fracture while recording the load-displacement response of all test samples. Also, failed samples were observed as such with unaided eye for failure modes as well as by cutting and mounting some cross-sections for observing under an optical microscope.

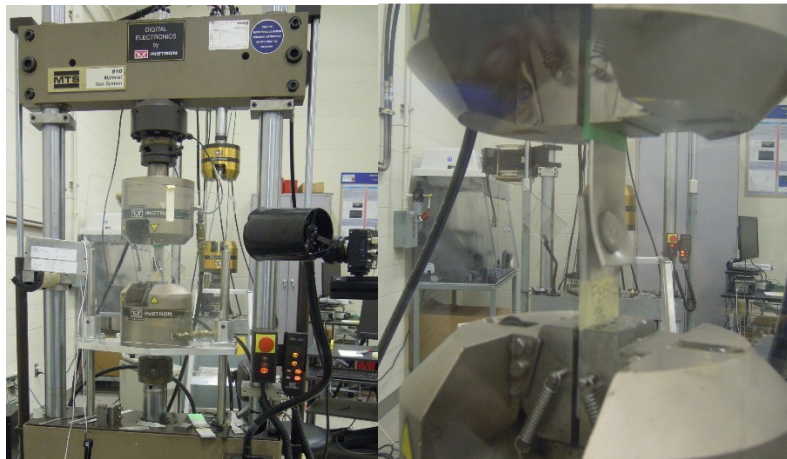


Figure 4.9. Experimental set-up for UPJ joint testing (left). The specimen in the setup (right).

#### **[4.4] Electrical Resistivity Measurements**

High electrical currents passing through the UPJ parts generate heat via classical electrical resistance heating process. This temperature achieved is a function of the resistivity of the material.



Two cast magnesium alloys, AZ91 and AM60, were used in the UPJ process where resistance heating was employed. However, a review of the literature, as noted earlier, revealed very little information on their electrical resistivity at room temperature and change in resistivity as a function of temperature. Any differences in the electrical resistivity of the two materials may offer additional insight into their respective heating rates and temperatures achieved, and consequently, their deformation behaviour during the UPJ process. Therefore, experiments were devised to obtain this data for the two alloys.

A common method of finding electrical resistivity of a material is through the use of a 4-wire resistance setup. A four wire setup has a precision current source and a precision voltmeter to find the resistance as expressed by Ohm’s law, as shown below in Figure 4.10 and in equation (4.1).

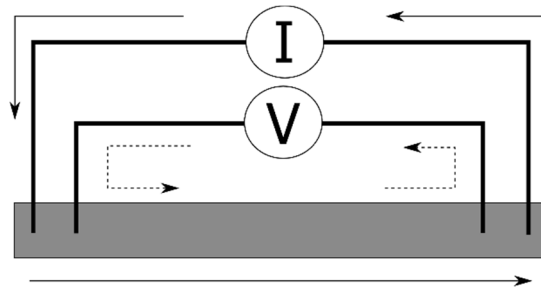


Figure 4.10. Electrical circuit for resistivity measurement. The test specimen in the form of a strip is shown in grey.

$$R = \frac{V}{I} \quad (4.1)$$

where  $R$ ,  $V$  and  $I$  represent resistance, applied voltage and current in the electrical circuit. The test material for electrical resistivity measurement is long and thin member of constant cross section

as shown in grey in Figure 4.9. For such a geometric configuration, the electrical resistivity can be simply expressed in the form of the following equation,

$$\phi = \frac{RA}{L} \quad (4.2)$$

where  $L$  is length,  $A$  is cross sectional area, and  $\phi$  is resistivity of the specimen.

The experimental set-up was relatively simple for electrical resistivity measurement as a function of temperature. The specimen was placed in a furnace and a thermocouple was placed close to the specimen. The furnace was heated to the desired temperature and the specimen was held at temperature for 15 minutes to reach a steady state. By measuring the applied voltage  $V$ , current  $I$ ,  $A$  and  $L$ , and utilizing equations (4.1) and (4.2), the electrical resistivity at the test temperature could be obtained. By carrying out experiments at a range of constant temperature conditions, electrical resistivity as a function of temperature was obtained.

The experimental procedure followed the ASTM standard for electrical resistivity measurement (ASTM B63-07, 2013). The experimental set-up is shown below in Figure 4.11. The set-up consisted of a tube furnace, a computer-based data acquisition system, a nanovoltmeter, a precision current source, and a thermocouple voltmeter (see Figure 4.11(a)). The test specimen was mounted with four wires (Figure 4.12) and placed into the tube furnace.

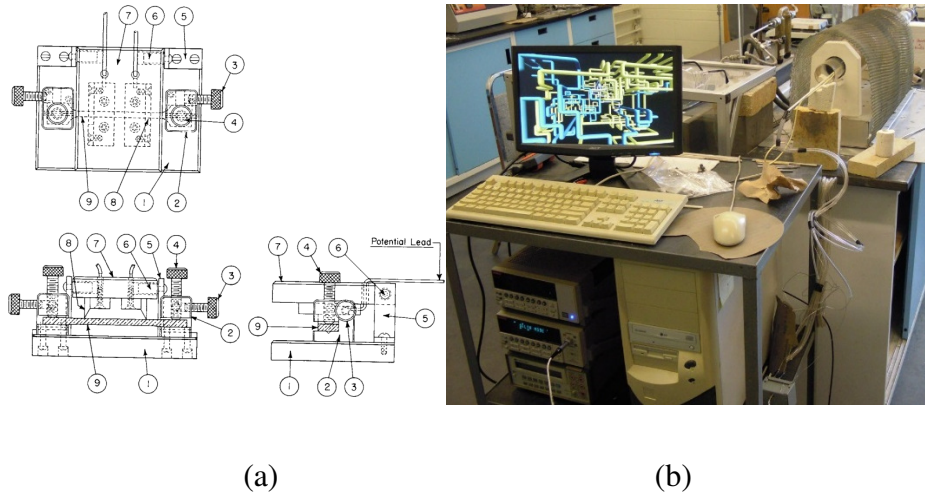


Figure 4.11. Electrical resistivity measurement set-up, (a) a schematic of the test-jig (ASTM B63-07, 2013), and (b) a photograph of the set-up utilized consisting of a tube furnace, computer-based data acquisition system, nanovoltmeter, a precision current source, and a thermocouple voltmeter (lower left).



Figure 4.12. A precision magnesium AZ91 sample with aluminum wires bonded to the specimen. This design was arrived at after several iterations of sample jigs, machining practices, and specimen geometry.

#### [4.5] Summary

Experimental procedures and test specific details pertaining to various deformation, and temperature and resistivity measurement experiments were presented in this chapter. Results from the above experiments are presented in the next chapter.

## **Chapter 5. Results**

This chapter presents results related to deformation and fracture behavior of AM60 and AZ91 cast magnesium alloys in the context of the UPJ process, as described earlier. The results are divided into 3 main sections covering axisymmetric isothermal compression of cylindrical specimens made from the above alloys, electrical resistance heating characteristics of these alloys, and large thermo-mechanical deformation of the protrusion (as part of a plate) to create the UPJ joint. Each of the main sections have been further divided into several sub-sections for a better comprehension of the diverse yet interconnected experiments.

### **[5.1] Isothermal Compression Test Results**

Compression load versus compression distance curves were continuously recorded from isothermal uniaxial compression tests on machined cylindrical specimens from AZ91 and AM60. The tests were conducted at different compression rates (or speeds) at several different temperatures in the range  $300^{\circ}\text{C} - 400^{\circ}\text{C}$  as described earlier in Chapter 4. All specimens were compressed inside the environmental chamber and with dimensions of 11mm in diameter and 14 mm in length as per the experimental procedure presented in Chapter 4.

#### **[5.1.1] True Stress versus True Strain Curves**

Compression load versus displacement data was converted to true stress versus true strain data. This conversion required the assumption that the specimen maintains a uniform profile with a consistent cross sectional area. During experimentation the protrusion exhibited barreling, resulting in a larger cross sectional area around the middle and a smaller at the top and bottom

causing some deviation in the expected true stress versus true strain response. Further compression resulted in material rolling onto the top and bottom platens, increasing the contact area (see Figure 5.1). Conversion of load-displacement data to true stress versus true strain data did not account for this barreling factor.

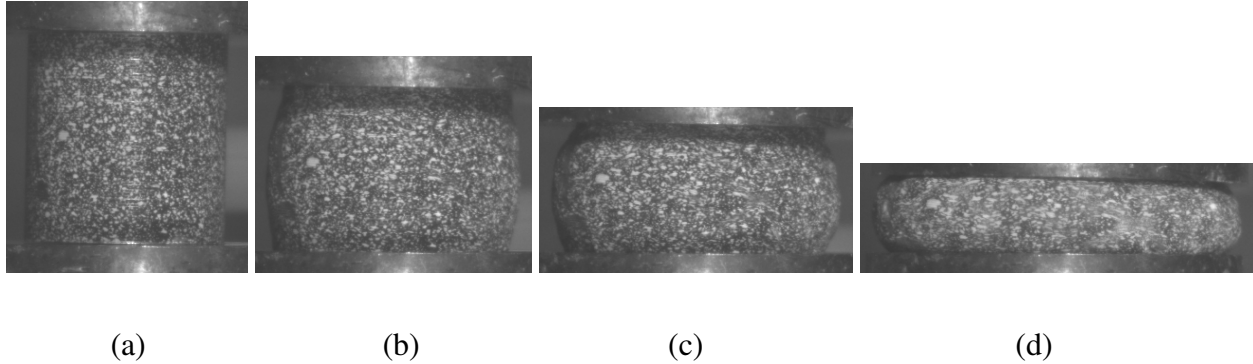


Figure 5.1. Barreling of a 14 long and 11 mm diameter cylinder of AZ91 compressed at 400°C and at a rate of 1 mm/minute, (a) initial geometry, (b,c,d) increasing contact between the platens and the protrusion as the ends of the protrusion stretch. As compression continues, part of the side walls of the protrusion become absorbed into the top and bottom surfaces (c and d).

Results in the form of true stress versus true strain in the temperature range 300°C – 400°C at a compression rate of 1 mm/minute are shown in Figure 5.2 (a). All of the curves exhibit a ‘saddle’ shape with an initial hump, a decrease, and then a gradual increase as the protrusion was compressed. Similar shape can be observed in the original load-displacement characteristic as well (see Figure 5.2 (b)). This trend was reduced when lubrication was added to the protrusion (see sub-section 5.1.1.3 later). However, since the saddle shape in the curves was present in a large number of samples tested without lubrication, the data in the later sections of this chapter are presented as a load versus displacement traces only. As expected, both the load-

displacement and true stress-strain curves systematically move to lower flow stress values with an increase in temperature. The tests were interrupted at a total true strain of about 1.1 in keeping with the range of strains achieved in the UPJ process.

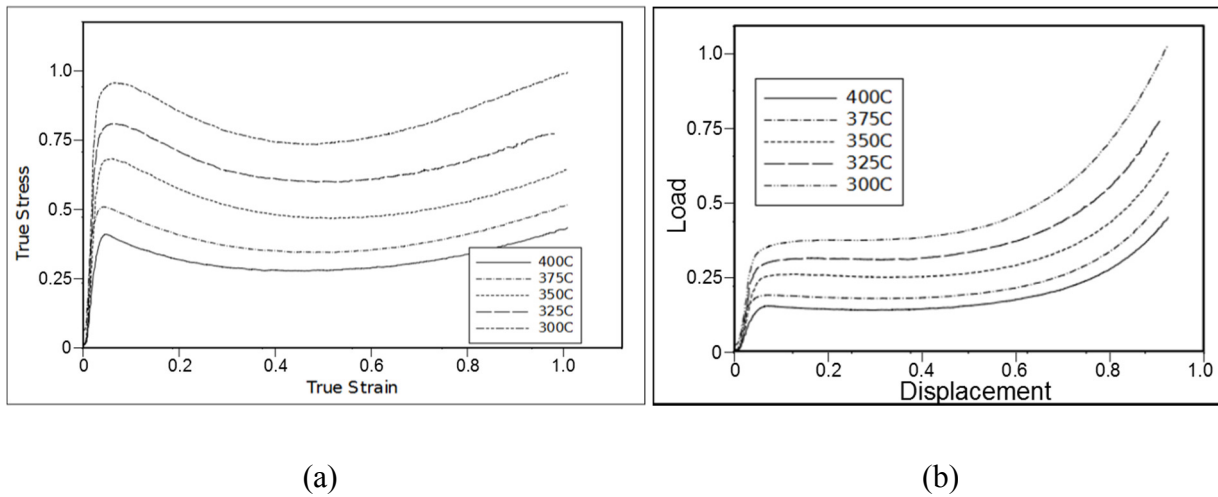


Figure 5.2. Comparison of material flow curves in axisymmetric compression at different temperatures, (a) true stress versus true strain curves, (b) punch load versus displacement curves. The tests were carried out on a 14 mm long, 11 mm diameter AZ91 protrusions compressed at a rate of 1 mm/minute.

Strain was also measured using digital image correlation (DIC) software within the ARAMIS strain measurement system in order to compensate for the barreling. This yielded inconclusive results due to the extensive fractures on the surface as well as the low resolution of the camera images. The imaging camera was outside of the heating chamber and viewed through several layers of high temperature glass resulting in reduction of image quality. As well, the patterns on the surface of the protrusion the DIC requires for measurement would either be enveloped by the platens or under such high strain the software could not sample or generate a

strain map properly. The strain maps had to be re-obtained in several ‘relative stages’ (2-4) during compression and yielded quantitatively unreliable results. Examples of strain maps are shown in Figure 5.3. As no consistent or reliable strain map could be created for all samples in all conditions, the process was discontinued.

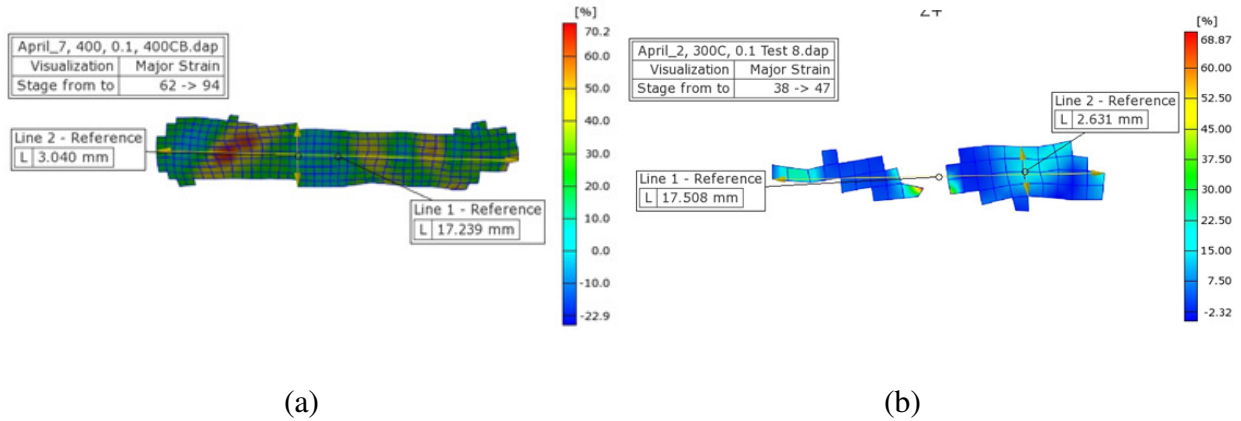


Figure 5.3. ARAMIS normal strain from the DIC software of 14mm long AZ91 cylinder compressed at a rate of 10 mm/minute. (a) Strain field data from a specimen compressed at 400°C. Regions of large strain in red and yellow and an angle to the vertical compression axis, from a slow strain rate test that exhibited minimal cracking and required only two relative stages for strain field analysis, (b). Strain field data from a specimen compressed at 300°C. There was significant loss of strain field data due to extensive cracking requiring several relative stages decreasing the analyzed area and accuracy of the result.

### [5.1.1.1] Effect of Compression Rate

Increasing compression rate (i.e., test speed) increased the force required to deform an 11 mm wide and 14 mm long cylinder of AZ91 while the shapes of the load-displacement traces remained largely similar. This behavior was observed at each of the 3 test temperatures (see Figures

5.4-5.6 below). For each individual test, the loads increased exponentially at large compression distances due to increased area of cross-section of the specimen, as reported in the literature for uniaxial compression tests on other metallic materials. Some discrepancy in the early part of the load-displacement curves from sample to sample can be noted, likely due to stiffness of the frame and the data collection system of the control system. Also, it appears that the elastic modulus of the cast alloys are rather sensitive to compression rate.

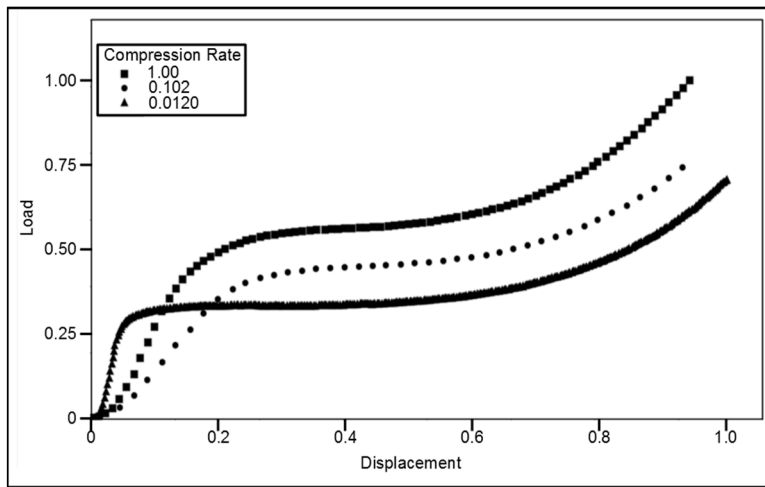


Figure 5.4. Comparison of compression load versus displacement traces for AZ91 cylinders tested at 300°C and 3 different compression rates.



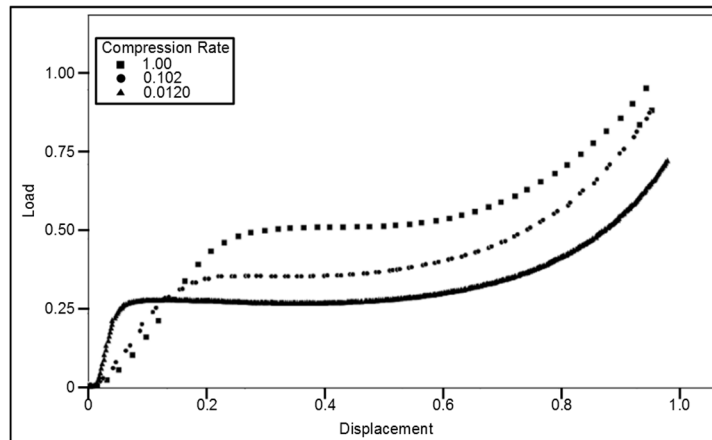


Figure 5.5. Comparison of compression load versus displacement traces for AZ91 cylinders tested at 350°C and 3 different compression rates.

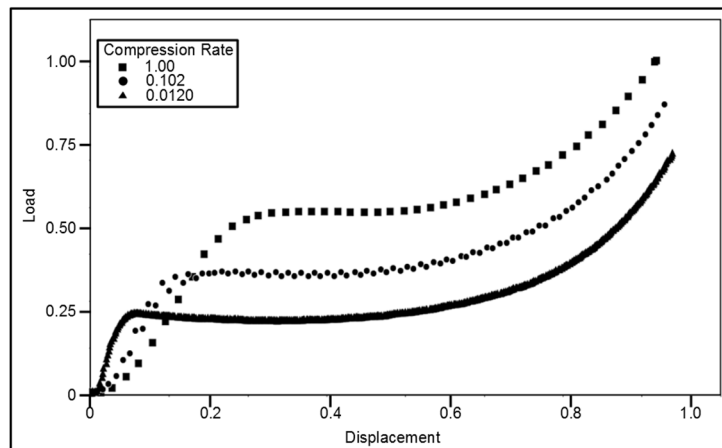


Figure 5.6. Comparison of compression load versus displacement traces for AZ91 cylinders tested at 400°C and 3 different compression rates.

### [5.1.1.2] Effect of Temperature

The effect of temperature is shown in Figures 5.7-5.9 below for 3 different compressions rates, 1 mm/min, 10 mm/min and 100 mm/min respectively. Once again, the punch load versus displacement traces have similar shapes. An increase in temperature progressively decreased the

force required to deform an 11 mm wide and 14 mm long cylinder of AZ91.

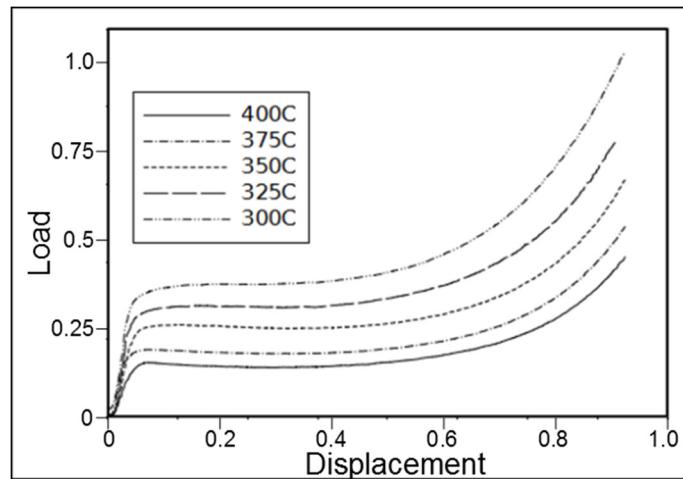


Figure 5.7. Comparison of compression load versus displacement traces for AZ91 cylinders tested at a compression rate of 1 mm/min and 5 different temperatures in the range  $300^{\circ}\text{C} - 400^{\circ}\text{C}$ .

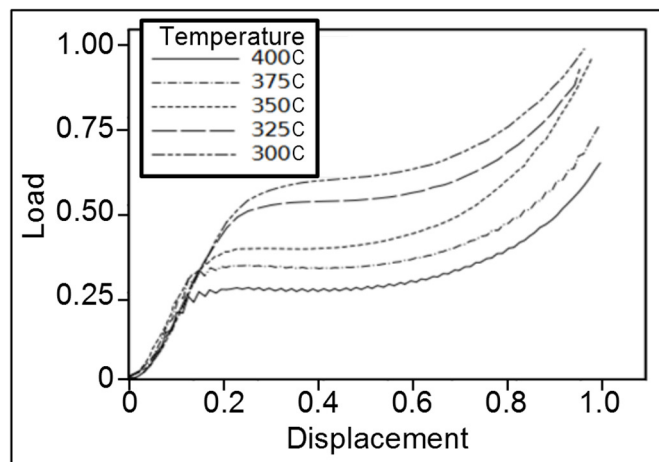


Figure 5.8. Comparison of compression load versus displacement traces for AZ91 cylinders tested at a compression rate of 10 mm/min and 5 different temperatures in the range  $300^{\circ}\text{C} - 400^{\circ}\text{C}$ . Noise in the data is due to differences in sampling rates between the triplicate experiments.

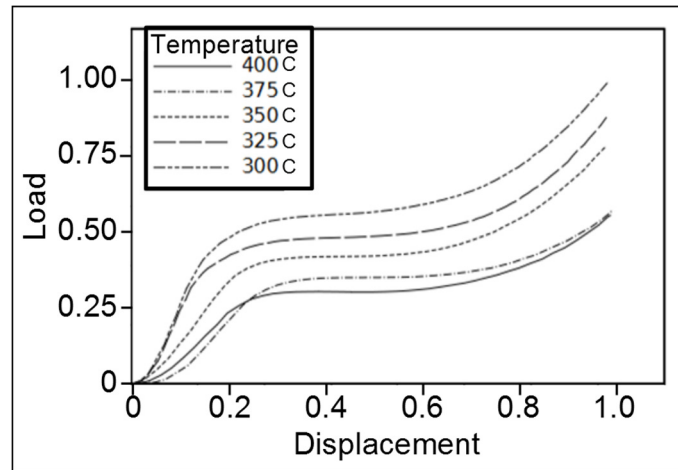
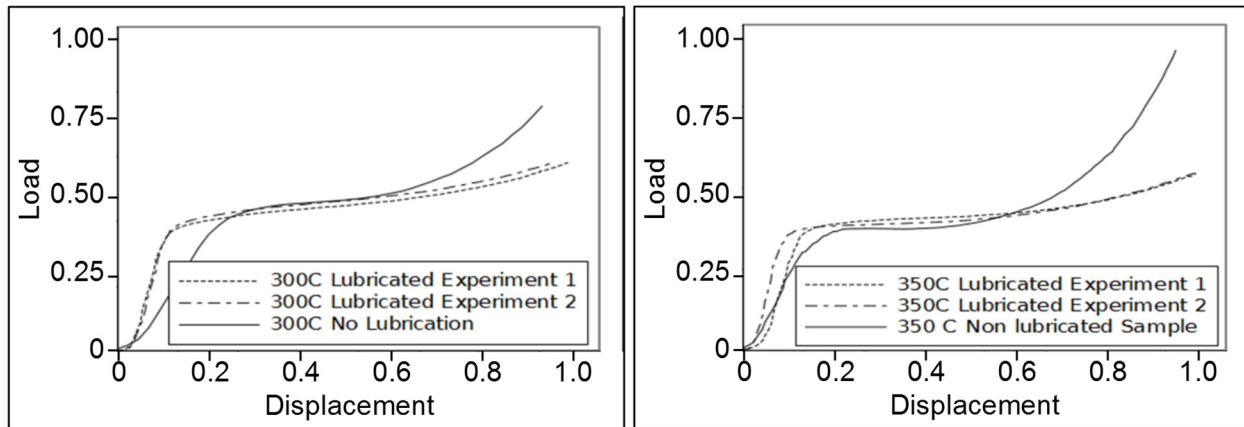


Figure 5.9. Comparison of compression load versus displacement traces for AZ91 cylinders tested at a compression rate of 100 mm/min and 5 different temperatures in the range  $300^{\circ}\text{C} - 400^{\circ}\text{C}$  .

### [5.1.1.3] Effect of Lubrication

Non-uniform deformation of the test specimen in the form of barrelling was observed in the test specimens during the test. To reduce the amount of barrelling, the surfaces of test specimen in contact with the compression platens of the test system were applied with a high temperature lubricant (commercial name, Loctite LB8150 silver grade anti-seize compound) and graphite sheet. The addition of lubrication decreased the load required for compression of magnesium AZ91 cylinders beyond 5 mm compression at two temperatures,  $300^{\circ}\text{C}$  and  $400^{\circ}\text{C}$  , as seen in Figure 5.10(a,b). The cylinders were compressed at a rate of 10 mm/minute.



(a)

(b)

Figure 5.10. Comparison of lubricated and non-lubricated compression of AZ91 cylinders compressed at (a) 300°C and (b) 350°C at a rate of 10 mm/minute with the same maximum normalized load axis.

#### [5.1.1.4] AM60 Versus AZ91 alloy

A comparison of load versus displacement curves from lubricated compression tests on AZ91 and AM60 specimens tested at 350°C and 10 mm/minute is shown in Figure 5.11. Both materials exhibited rather similar curves with AM60 showing a slightly lower flow stress compared to that of AZ91.

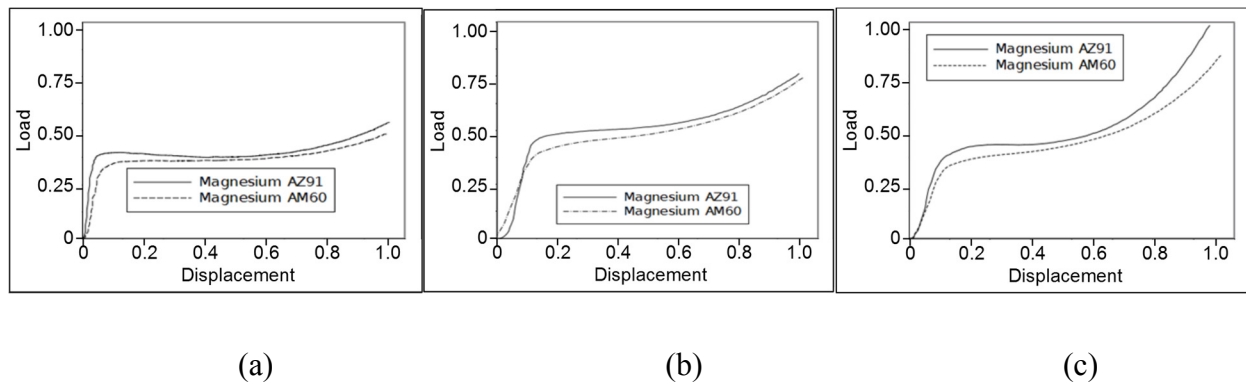


Figure 5.11. A comparison of load versus displacement of lubricated AM60 and AZ91 specimens compressed at  $350^{\circ}\text{C}$  and (a) 1mm/min, (b) 10 mm/min and (c) 100mm/min

## [5.1.2] Deformed Specimen Surface and Fracture Characteristics

### [5.1.2.1] Crack Initiation, Growth and Propagation

Fractures on protrusions during compression were typically observed on the free outer surface. Cracks initiated at an approximate angle of  $45^{\circ}$  with respect to loading (or vertical) axis (see Figure 5.12). Multiple cracks were observed with similar orientation in some cases all around the periphery of the specimen. In other cases, intersecting cracks at 2 different symmetric orientations (i.e., with an “X” shape) were observed. However, the crack morphology, as mentioned above, did not strictly follow a trend with respect to compression rate or temperature. Separate studies by another researcher in the group have revealed formation of macroscopic shear bands which intensify and become the site of crack initiation. At several strain rates and temperatures, the protrusion fractured well before reaching the desired true strain of 1.1.

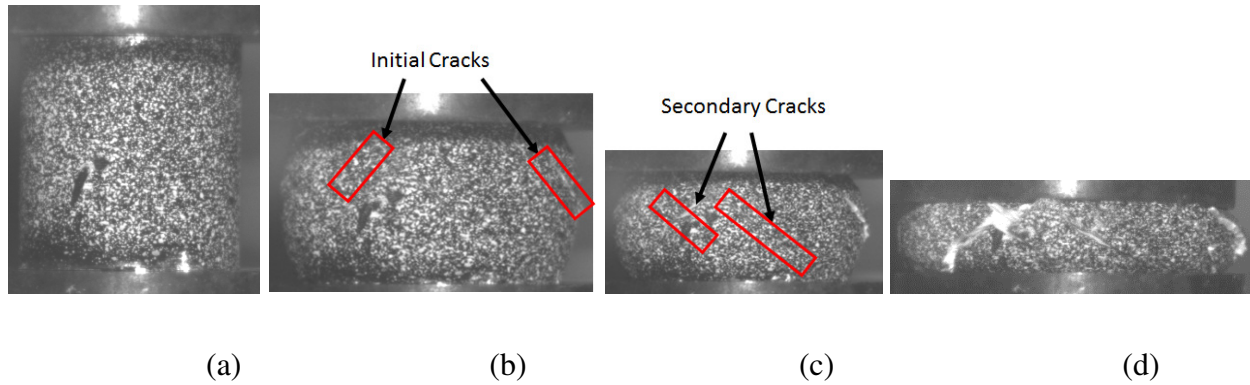


Figure 5.12. Crack initiation and growth on AZ91 cylinder compressed at a temperature of 350°C at a rate of 10 mm/minute, (a) undeformed initial protrusion, (b) crack initiation at an angle of 45° angle relative to axis of loading and at a vertical displacement of 5 mm, (c) secondary crack formation perpendicular to the initial cracks to form an ‘X’ shape at a vertical displacement of 8 mm, and (d) crack growth of one or both arms of ‘X’ shape along the hoop direction at a vertical displacement of 10 mm.

#### [5.1.2.2] Effect of Compression Rate

Triplicate compression experiments were performed on cylinders of AZ91 at compression rates of 1, 10, and 100 mm/minute and at temperatures of 300°C, 325°C, 350°C, 375°C, and 400°C. No noticeable change in the load versus displacement curves were noted at the onset of crack formation. Videos of each compression test sample was recorded and the true strain at crack initiation was found (see Figure 5.13). Some samples could be compressed to rather large strains without fracture. From this, lower compression rates and higher temperatures (tended to) increase the strain prior to failure.

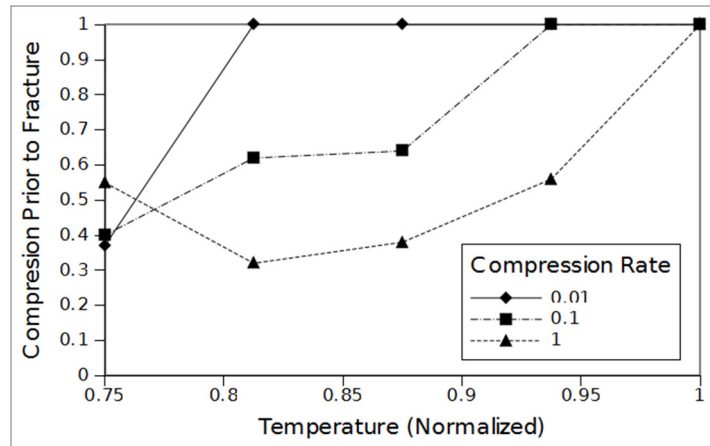


Figure 5.13. Compression strain prior to fracture at set temperatures and compression rates. No fracture is a value of 1.0.

Figure 5.14 below shows fracture characteristics of AZ91 with increasing compression rates at two different temperatures to a final height of 4 mm. The specimens were unlubricated. The barrelled surface of the specimen were folded over to become part of the top and bottom surfaces of the specimen at large displacements.

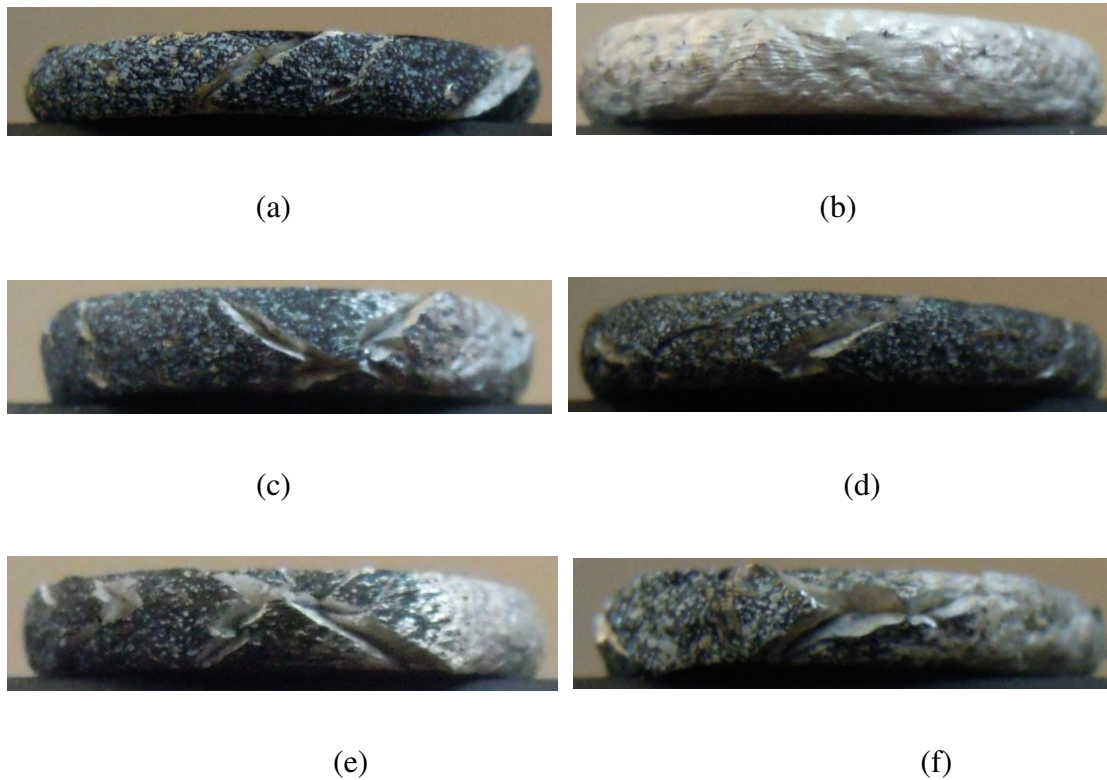


Figure 5.14. A comparison of fracture characteristics of AZ91 specimens compressed at two warm forging temperatures and 2 different compression rates, (a) lower temperature and slow compression, (b) higher temperature and slow compression, (c) lower temperature and moderate compression, (d) higher temperature and moderate compression, (e) lower temperature and rapid compression, (f) higher temperature and rapid compression.

### [5.1.2.3] Effect of Temperature

The effect of temperature on crack morphology of AZ91 samples is shown in Figure 5.15. All tests were carried out under unlubricated conditions. The morphologies correspond to the fastest compression rate of 100 mm/min and final height of 4 mm. The propensity for surface roughening and cracking decreased with an increase in temperature in the range  $300^{\circ}\text{C} - 400^{\circ}\text{C}$ .



The deformed specimens were largely crack free at 400° C. This is attributed to reduced flow stress as noted earlier in the load-displacement curves and more homogeneous flow of the material (leading to a reduced flow instability) at higher temperatures.

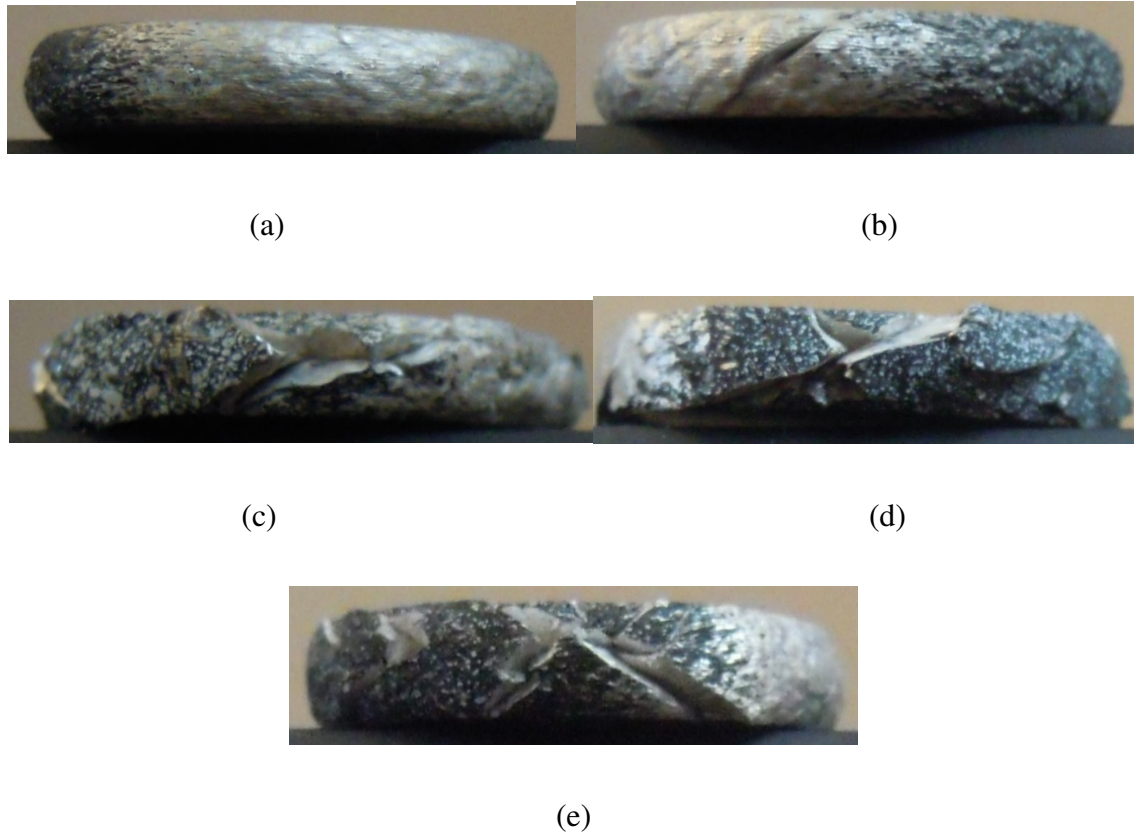


Figure 5.15. A comparison of fracture characteristics of uniaxial compression AZ91 with a rapid compression rate, (a) high temperature, (b) moderately high temperature, (c) moderate temperature, (d) low temperature and (e) very low temperature.

#### [5.1.2.4] Effect of Lubrication

Lubrication was found to reduce barreling and greatly reduce cracking and surface roughening of the protrusion, as shown below in Figure 5.16. This is attributed to a reduction in

friction between the compression platen and the top and bottom surfaces of the specimen. The effect is reported extensively in the literature. The tendency for crack initiation was also reduced with lubrication (and reduced barrelling) as the circumferential hoop strain component was reduced leading to an overall decrease in the effective applied strain. The addition of lubrication decreased the maximum diameter of the protrusion in the mid-height region by 0.5-1.3 mm.

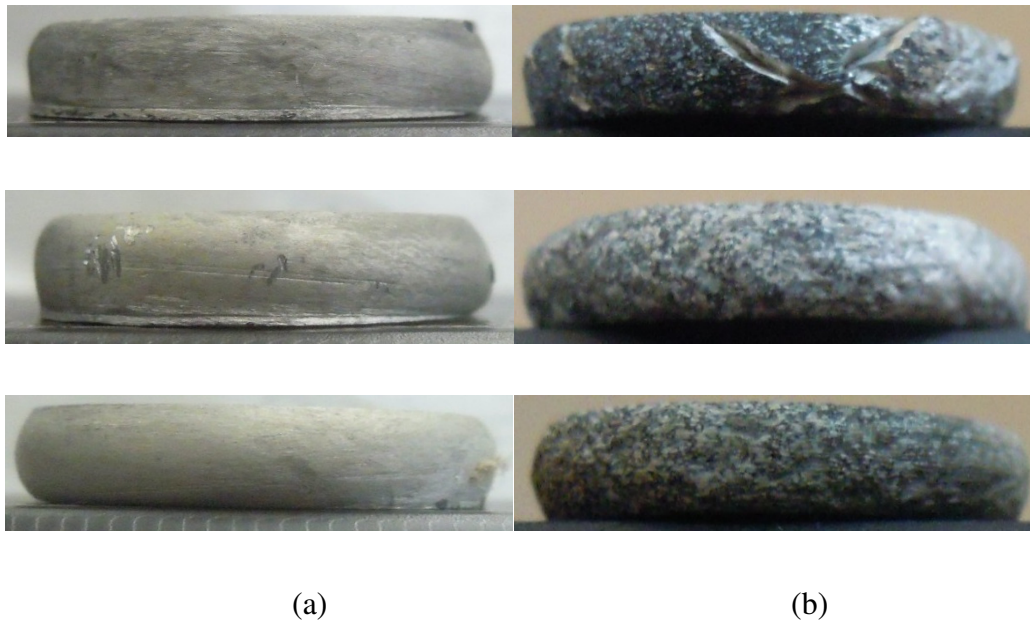


Figure 5.16. A comparison of deformed AZ91 samples, (a) with lubrication (left column), and (b) without lubrication (right column) compressed at 10 mm/min and at 300°C (top row), 350°C (middle row) and 400°C (bottom row). All samples were deformed to a height of 4 mm.

#### [5.1.2.5] AM60 Versus AZ91

No significant visual difference was noticeable between the lubricated compression of AM60 and AZ91. A key factor for this is that the maximum compression rate possible in the test system was 100 mm/minute. Slightly less barrelling was noted for AZ91. However, this trend may

be attributed to experimental error (see Figure 5.17 below for a qualitative comparison). The origin of this difference is presently unknown.

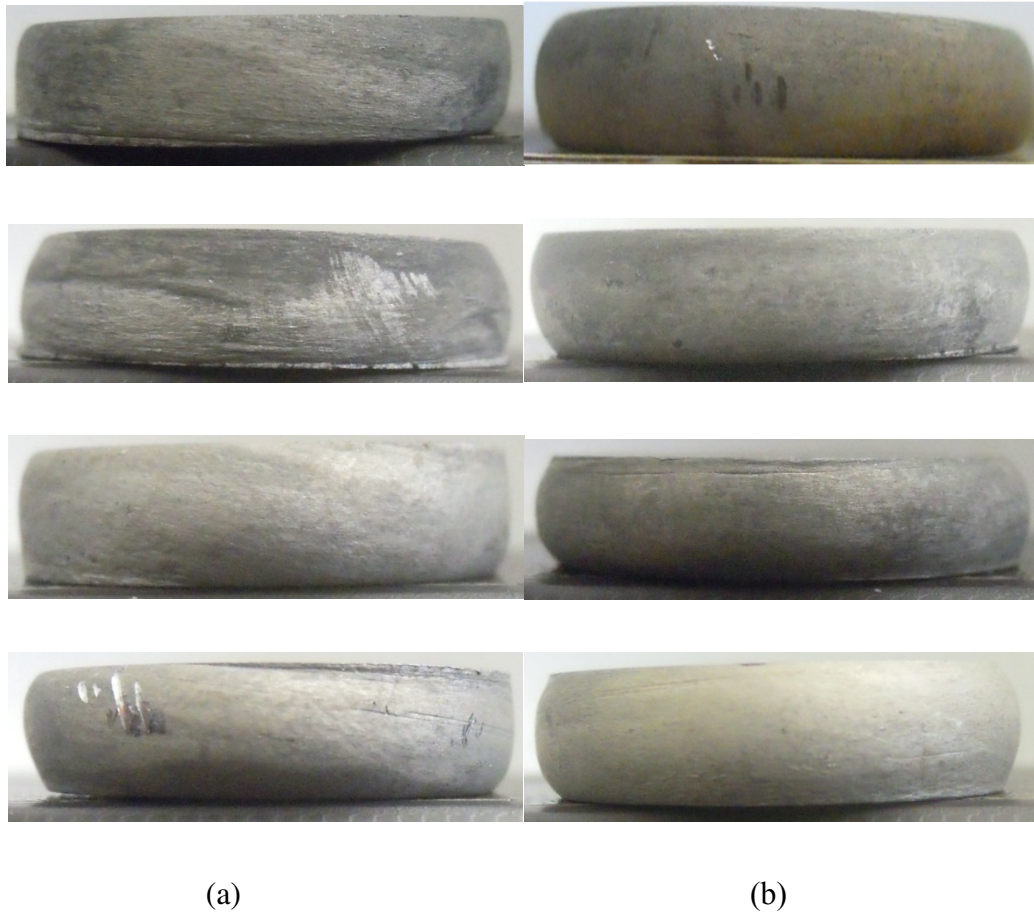


Figure 5.17. A comparison of (a) AZ91 and (b) AM60 cylinders compressed with lubrication at 1mm/minute compressed from 10 mm to a final length of 4 mm at a temperature of 250°C (top row), 300°C (upper middle row), 350°C (lower middle row) and 400°C (bottom row).

## [5.2] UPJ Specimen Heating Results

### [5.2.1] Thermocouple-based Results

#### [5.2.1.1] Embedded (Internal) Thermocouple Results

As noted earlier in Chapter 4.1.4.1, thermocouples were mounted at the top, middle and bottom of the UPJ protrusion by inserting them in small holes drilled transverse to the axis of the protrusion. A characteristic temperature-time curve from a thermocouple inserted at the mid-length of the protrusion and heated with a current profile 6 kA for 0.4 seconds is shown in Figure 5.18. The temperature response of the thermocouple appears to be rather rapid and synchronized with the application of current at short current durations. The temperature drops steadily after the application of the current.

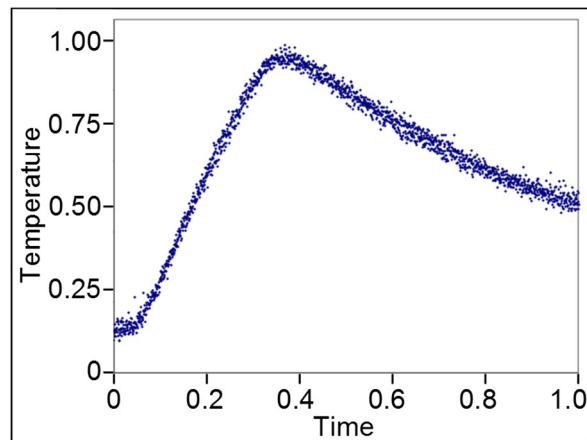


Figure 5.18. Characteristic temperature time trace form a thermocouple mounted inside a protrusion.

The temperature-time profile from 3 thermocouples mounted near the top and bottom and in the middle of the protrusion are shown in Figure 5.19. The temperature past the peak temperature

decayed exponentially for all experimental conditions. The protrusion was heated with 5 kA for 1 second. The middle of the protrusion exhibited the highest temperature. This was followed by intermediate temperature at the bottom and the lowest temperature at the top of the protrusion. This trend was found to be consistent throughout the various protrusion experiments (i.e., different current levels, test speeds etc.). The lowest temperature at the top of the protrusion could conceivably come from conductive heat transfer from the top of the protrusion to the cooler top electrode.

A key aspect of thermocouple based results is that the thermocouple itself has a specific heat and there was a time delay between the application of heat and registration of temperature by the thermocouple at larger current durations. This is due to heat transfer through the thermocouple. Consequently, after the current had been cut off (i.e., the heating cycle has been completed), the thermocouple continued to register increase in temperature as per the Newton's law of cooling. This can be seen in the continued rise in temperature past the 1 second mark in Figure 5.19.

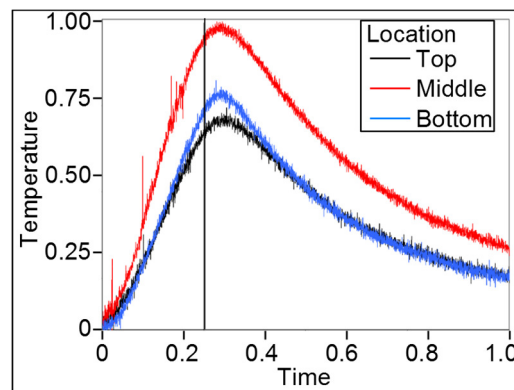


Figure 5.19. A comparison of temperature-time profiles for AZ91 protrusion heated with 5 kA for 1 second at a measurement location 1 mm from the top of the protrusion, the middle, and 1 mm from the base of the protrusion.

Increasing current increased the temperature of the protrusion exponentially as shown in Figure 5.20. This was also found to be consistent for the different test conditions. Theoretically, increasing the current duration increased the temperature linearly, however increasing current duration increases heat loss to the surrounding and results in a fall off. This trend is shown in Figure 5.21 and was found at all thermocouple locations.

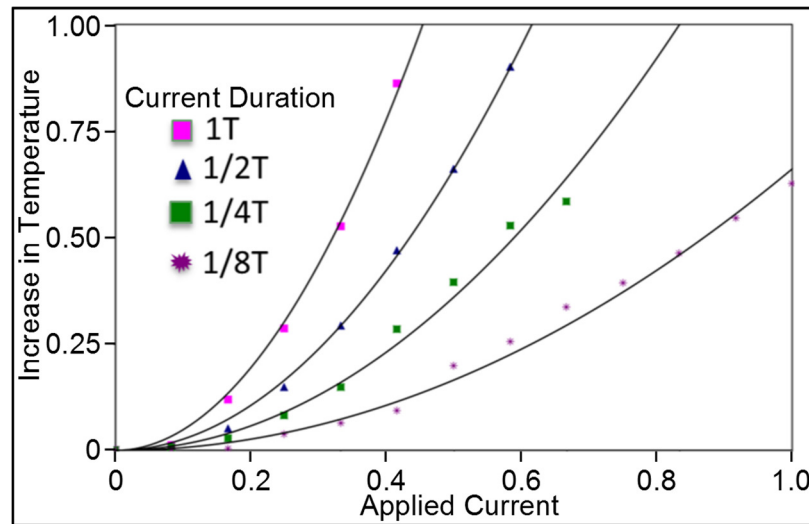


Figure 5.20. A plot of temperature from the middle thermocouple versus applied current for 4 different durations of constant applied current.

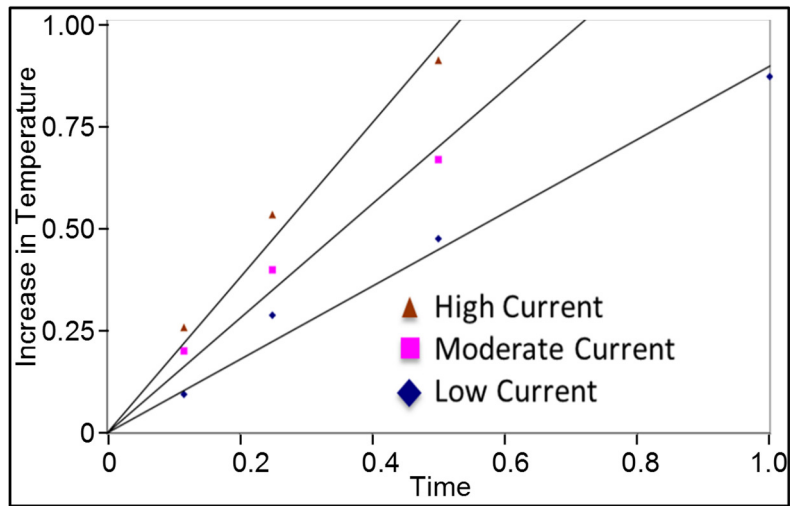


Figure 5.21. A comparison of temperature increase from the middle thermocouple as a function of duration of constant applied current for different current levels.

A comparison of the temperature-time profiles from four different protrusions heated with a constant current of 4 kA but with increasing duration of current application is shown in Figure 5.22. The rate of change of temperature as well as the peak temperature increased with an increase in the current duration. The rate of decrease in temperature past the peak temperature also increased with the increase in current duration.

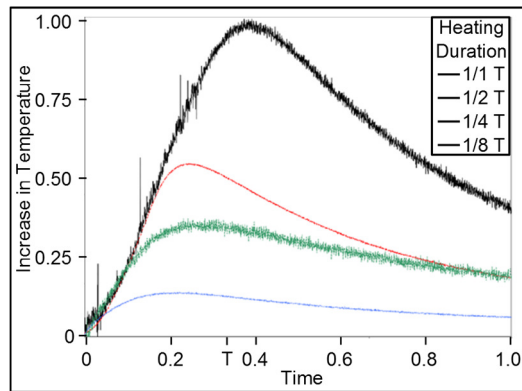


Figure 5.22. A comparison of temperature-time profiles at the mid-length position of an AZ91 protrusion heated with 4 kA of current for 4 different time durations.

The tests at similar CSTP values were found to yield similar maximum temperature measurements from internal thermocouples as shown in Table 5.1. The maximum current was changed from 9 to 15kA and the current duration was changed to produce the same CSTP.

Table 5.1. Comparison of temperatures measured by a centrally located thermocouple inside an AZ91 protrusion heated with the same CSTP of 81 kA<sup>2</sup>-s.

Current (kA)	Current duration (s)	Max. Temperature (°C)
0 to 9	1	220
0 to 10	0.81	223
0 to 11	0.67	225
0 to 12	0.56	233
0 to 13	0.48	228
0 to 14	0.41	212
0 to 15	0.36	224

### [5.2.1.2] Surface Mounted (External) Thermocouple

#### [5.2.1.2.1] AM60

The heating profile found from internally mounted thermocouples, shown earlier in Figure



5.19, were also seen with surface mounted thermocouples. For a heating of 0 to 15 kA for 0.25 seconds, the hottest location was at the middle, followed by the bottom, and the top was the coldest as shown in Figure 5.23 (but with some overlap in the top and bottom profiles). This temperature profile was consistently seen at all current profiles.

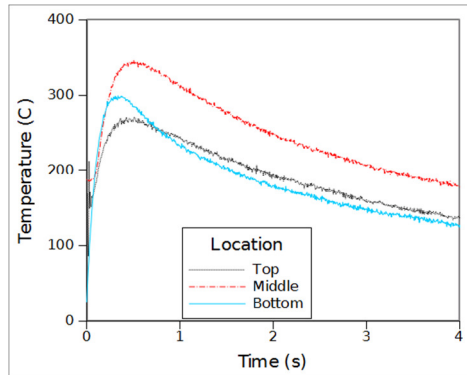


Figure 5.23. A comparison of temperature-time profiles for AM60 protrusion heated with a current profile of 0 to 15 kA over 0.22 seconds. Surface temperatures were measured 1 mm from the top of the protrusion, the middle, and 1 mm above the base of the protrusion

AM60 protrusions were heated with the same maximum current (0 to 11 kA) over a duration of 0.66, 0.5 and 0.33 seconds. The protrusion temperature nearly doubled as a result of increasing the duration of heating between 0.33 to 0.66 seconds as seen in Figure 5.24.

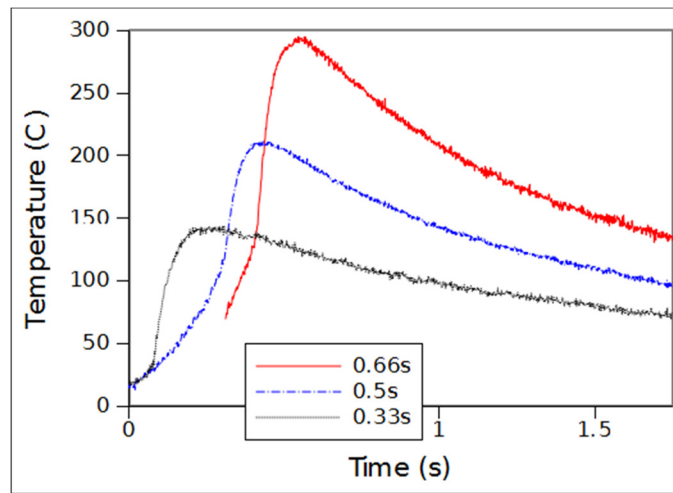


Figure 5.24. A comparison of temperature-time traces for surface mounted thermocouple located in the middle of an AM60 protrusion heated with 0 to 11 kA over 0.33, 0.5 and 0.66 seconds.

A comparison of temperature versus time profiles when the protrusions were heated with the same CSTP value of  $81 \text{ kA}^2\text{-s}$  is shown in Figure 5.25. It is seen that lower maximum current (9 kA) reduced the maximum temperature reached. The maximum external and internal thermocouple readings are compared in Table 6.3.

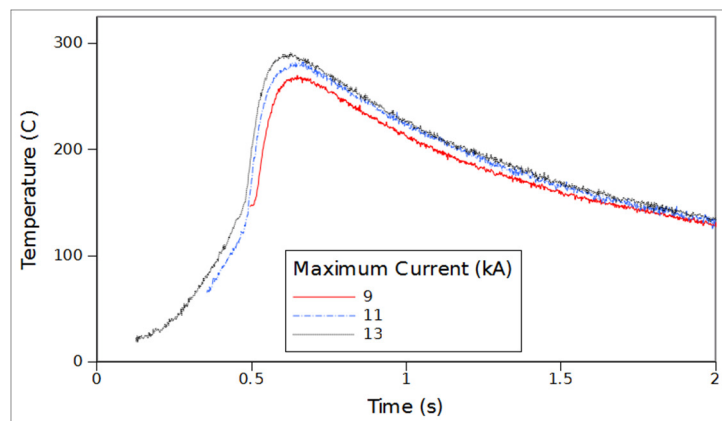


Figure 5.25. A comparison of temperature-time profiles from surface mounted thermocouples located in the middle of an AM60 protrusion subjected to a CSTP of  $81 \text{ kA}^2\text{-s}$ . The peak

temperatures of the temperature-time curves were aligned for comparison. Beyond the peak temperature the protrusion is cooled. Signal noise in this experiment prevented collection of temperature data while current was applied.

Table 5.2. A comparison of maximum internal and external temperatures from AM60 81 kA<sup>2</sup>-s CSTP experiments. Internal and external temperatures were measured with a grounded and shielded thermocouple and an external thermocouple welded to surface respectively.

Current (kA)	Duration (s)	Internal temperature (°C)	External temperature (°C)
0 to 9	1	232	270
0 to 11	0.66	238	283
0 to 13	0.49	242	291

A higher skin temperature from external thermocouple is likely caused by two possibilities. First, the skin surface has a higher resistivity as a result of denser grain density (or fine grain size). This would increase the heating of the skin surface relative to the internal heating. The second reason for difference in interior and exterior temperature measurement is that the skin surface was a fine thermocouple welded directly to the surface of the protrusion whereas the internal measurements were done using a tungsten encased thermocouple press fit into a hole with thermal conducting paste. As the protrusion cooled rather rapidly after heating, the temperature response of the internal thermocouple was expected to be sluggish and could cause the temperature differences.

Once again, the results shown in Table 5.2 suggest that a constant CSTP value tends to produce rather similar temperatures. The key parameters used in UPJ were the maximum current applied, the CSTP value, duration of application of current, compression rate, and compression

distance. As maximum current applied, duration of application of current and CSTP are related to one another, only two of these parameters were needed to be defined.

**[5.2.1.2.2] AZ91**

The heating profiles from internally mounted thermocouples, shown earlier in Figure 5.20, were also seen with surface mounted thermocouples. For an applied current of 0 to 11kA for 0.66 seconds, the surface mounted thermocouples measured a significantly higher surface temperature than for the internal measurements. Internal measurements recorded a maximum temperature of 240°C at this heating profile, while skin temperatures approached 300°C as shown below in Figure 5.26.

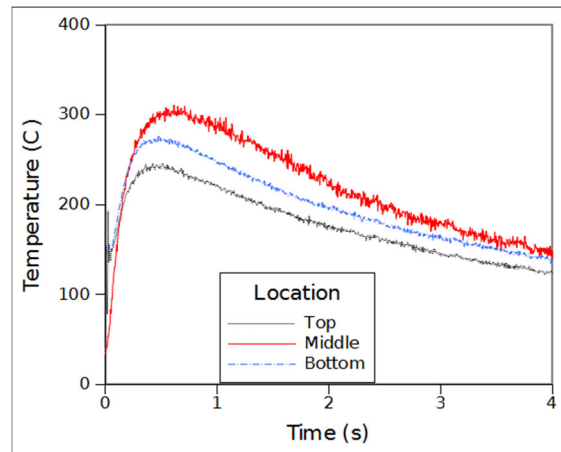


Figure 5.26. A comparison of temperature-time profiles for AZ91 protrusion heated with 0 to 11kA over 0.66 seconds at a surface measurement location 1mm from the top of the protrusion, the middle, and 1mm from the base of the protrusion.

A comparison of temperature-time profiles for AZ91 protrusions heated to 9 kA, 11 kA and 13 kA over a duration of 1, 0.66, and 0.48 seconds are shown in Figure 5.27. The trends are similar

to those reported earlier for AM60 (see Figure 5.25)

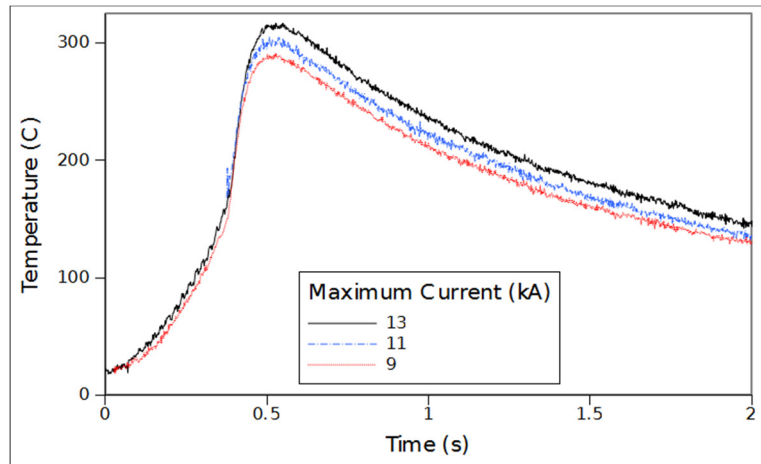


Figure 5.27. A comparison of temperature-time profiles from surface mounted thermocouples located in the middle of an AZ91 protrusion subjected to a CSTP of  $81 \text{ kA}^2\text{-s}$ . The peak temperatures of the temperature-time curves were aligned for comparison. Beyond the peak temperature the protrusion is cooled.

Thermocouples mounted internally and externally on an AZ91 protrusion heated with a constant CSTP of  $81 \text{ kA}^2\text{-s}$  while the maximum applied current was changed from 9 to 15kA over 1 kA intervals as shown in Table 5.3. The maximum temperature of the protrusion was relatively constant in the range of  $212^\circ\text{C}$  and  $233^\circ\text{C}$  internally and  $293^\circ\text{C}$  and  $312^\circ\text{C}$  externally. The average internal temperature was  $223^\circ\text{C}$  while the external temperature was  $301^\circ\text{C}$ , a difference of  $78^\circ\text{C}$ . This difference is thought to be caused by differences in thermocouple design or the higher resistivity on the outer surface, as mentioned earlier.

Table 5.3. A comparison of applied current, current duration and maximum internal and external temperatures attained in AZ91 protrusions.

Applied Current (kA)	Current Duration (s)	Max. Internal Temperature (°C)	Max. External Temperature (°C)
0 to 9	1	220	312
0 to 10	0.81	223	307
0 to 11	0.67	225	303
0 to 12	0.56	233	295
0 to 13	0.48	228	298
0 to 14	0.41	212	303
0 to 15	0.36	224	293

### [5.2.2] Infrared (IR) Camera-based Results

The above theoretical relationship between CSTP input, applied current value and current duration was also assessed by measuring maximum surface temperature on AZ91 protrusions with an infrared (IR) camera. Temperature was measured near the plate, the hottest location on the protrusion. Two examples of semi-qualitative result are shown below in Figure 5.28, showing the variation in temperature profile of the protrusion. The results were considered unreliable, indicating that increasing the heating rate increased the skin temperature exponentially. One theory which coincided with result was the surface of the protrusion has a higher grain density, resulting in a higher resistivity. This could increase the heating on the skin surface, and as higher heating rates have lower heat transfer to the surrounding, the faster heating would have a hotter skin. However, this theory is unable to explain the temperature profile on the skin or a rapid increase in temperature with higher currents.

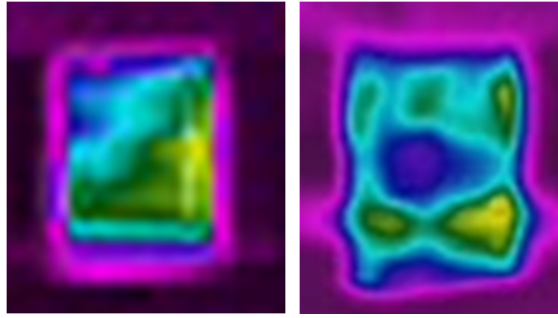


Figure 5.28. Two experimental results from the infrared camera under the same current profile conditions. The colour band (rainbow colour) indicated red the hottest, followed by yellow, green, teal, blue, and purple the coldest. Two different hottest temperature locations are noted on the two examples provided.

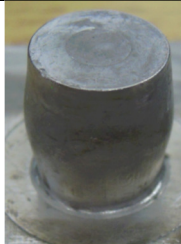
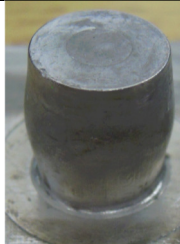

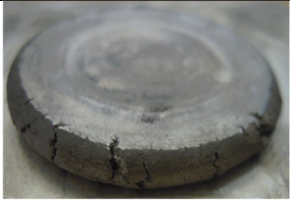




### [5.3] Cast Protrusion Compression Experiments

AZ91 cast plate components, with no upper plate (with hole), were heated and compressed to set distances using the UPJ system to compare the deformation characteristics of the protrusion. The AZ91 protrusions were heated with a current profile of 0 to 11 kA over 1 second and compressed at a rate of 42 mm/s. At 1 mm compression distance, the protrusion formed a barreled shape such as the top third of the protrusion was the widest (see Table 5.4). This is consistent with the free (or unconstrained) deformation of the top compared to the fixed base of the protrusion. Also, as noted earlier from thermocouple experiments, the middle of the protrusion was commonly the hottest, followed by the top, and the bottom the coldest. So the upper half of the protrusion at higher temperature was able to deform more easily compared to the lower half at a lower temperature. At 6 mm compression distance, the protrusion barreled to form a vase shape where the top third has a rapidly changing diameter. As the upper Tungsten electrode had a high thermal conductivity and a larger specific heat compared to that of AZ91 magnesium, the electrode

extracted heat energy from the magnesium and increasing the flow stress near that contact surface. In addition, friction at the electrode/protrusion interface resisted the expansion of the protrusion at the top of the protrusion. The bottom plate feature of AZ31 continued to constrain any shape change to the bottom of the protrusion. Since the middle region of the protrusion was the hottest and was free to deform, its flow stress was reduced and it was able to expand in that area. These factors collectively allow the top third of the protrusion to deform the most. At 9 mm compression distance, both the top and bottom rolled over to become part of the top and bottom surfaces of the protrusion covering the original top and bottom edges of the cylinder. This was clearly evident in the impression marks separating the old and new edges at the top of the protrusion. The protrusion now exhibited beveled edges tangent to the top and bottom surfaces and nearly half of the material in the protrusion became part of the barrelled section. Lastly, at 12 mm compression distance, the protrusion exhibited surface cracks in the coin-like barrelled region. The chamfer was removed and a definitive edge was formed as more material came in contact with the electrode. The crack emanated from the surface and the centre region of the highly coined protrusion remained crack-free.



Table 5.4. Comparison of compressions of AZ91 cast plate to set distances.

Compression Distance	1 mm	6 mm	9 mm	12 mm
Photographs of deformed protrusions				
Protrusion profile evolution				

As noted earlier, increasing friction between the electrode (i.e., compression platen in the isothermal experiments) and the protrusion resulted in a decrease in the radial strain at the top strain relative to the circumferential strain in the middle and consequently increasing the barreling of the protrusion. Barreling is beneficial in terms of a decrease in compressive load, as observed with compression of cylinders in an environmental chamber. However, it does increase the propensity towards surface fracture of the specimen.

#### [5.4] UPJ Trial Results

In this sub-section, the results from trials on AZ91 and AM60 cast protrusions joined to an aluminum sheet to create the UPJ joint are presented. The details of the experimental set-up were provided earlier in Chapter 3. The results take the form of punch load versus displacement traces, load versus time traces, visual appearance, with an unaided eye, as a measure of ‘quality’ of the

joint as well as optical microscopic observations of cut UPJ joints.

#### **[5.4.1] Test repeatability results**

##### **[5.4.1.1] Punch Load Versus Displacement Curves**

Ten repeated UPJ experiments were carried out on AM60 cast samples, each at a current of 0 to 11.5 kA over 1.11 seconds and a compression rate of 21 mm/s while keeping all other parameters as well as the test procedure identical. The objective here was to see if the punch load versus displacement, as a process ‘signature’, was repeatable. Each of the protrusions was preloaded first, and then at 0.8 seconds it was heated by supplying a current. At 2 seconds, the current was turned off and the protrusion was compressed from an initial length of 14 mm to a length of 4 mm (thus providing a compression distance of 10 mm). The protrusion was then held in position for another 0.2 seconds before the ram (actuator) was retracted to remove the specimen from the test system. The load versus time and actuator position versus profiles at various stages of the test are shown below in Figures 5.28 and 5.29 respectively. These tests, as noted earlier in Chapter 4 were conducted in load control when pre-loading and then switched to position control when deforming the protrusion during compression. Consequently, in the largely elastic deformation during pre-loading both the load and position signals have very little variability until the specimen heating occurs at which time both load and position fluctuations occur due to frequent and unstable loss and re-establishment of contact between the electrode and the protrusion. However, during subsequent plastic deformation of the protrusion, the contact is permanently established and the position control is accurately maintained as shown in Figure 5.29. However, it is likely that the peak load fluctuations occurred from sample-to-sample due to contact variations

from either cast specimen top and bottom surface quality or perhaps material variability from the casting process (see Figure 5.30).

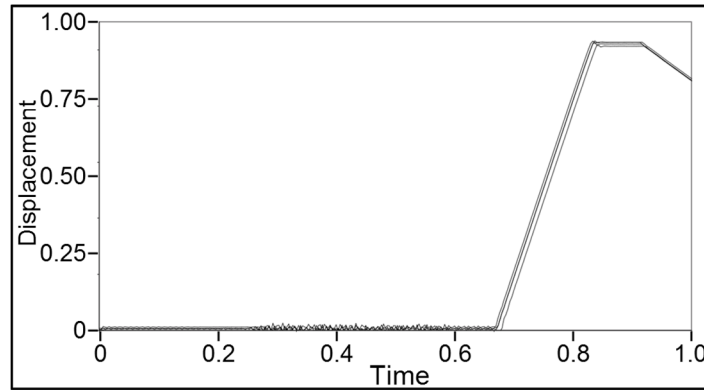


Figure 5.29. Load versus time traces from repeated UPJ experiments.

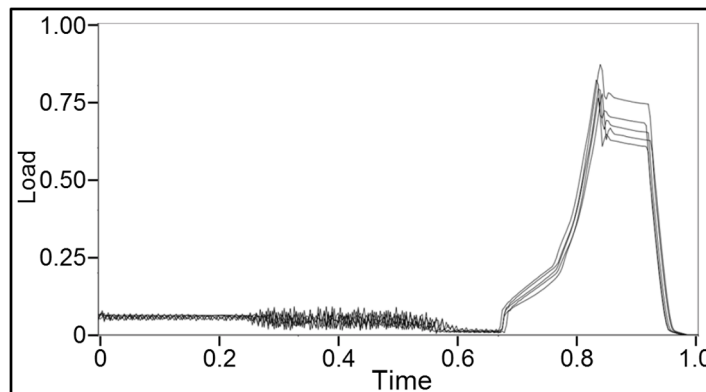


Figure 5.30. Position versus time traces from repeated UPJ experiments.

#### [5.4.1.2] Protrusion Deformed Surface and Fracture Characteristics

The results of test repeatability in terms of images of UPJ joints are shown in Figure 5.31 from a set of 5 repeat tests. Four of the five UPJ samples exhibited largely crack-free deformation of the protrusion to create the joint head.



Figure 5.31. A comparison of visual appearance of UPJ heads from 5 repeat tests. Four of the 5 tests did not indicate any cracks or fissures, while the fifth (left most) had small surface cracks on the top edge that did not penetrate into the protrusion.

#### **[5.4.2] Test Matrix 1 Results**

Two different test matrices were considered for UPJ experiments to investigate the effect of process variables on the quality of the UPJ joint. The first test matrix, referred to as ‘Matrix 1’, involved a broader exploration of the effect of process variables to develop a general understanding of the sensitivity of each of the process variables on punch load versus displacement traces as well as surface quality of the protrusion head. The second test matrix, referred to as, Taguchi orthogonal array, was based on 3 key process variables, where the goal was to identify the optimum combination of the 3 process variables to produce the ‘best’ visual quality of the joint, irrespective of its punch load versus displacement response. All UPJ tests reported in this sub-section were conducted on cast (and not subsequently machined) protrusions with the premise that original fine grain structure of the cast surface will play a critical role in the thermo-mechanical deformation process. A brief study was also conducted on cast and lightly machined protrusions as noted earlier in Chapter 4.

### [5.4.2.1] AM60 Cast Plate with Protrusion

#### [5.4.2.1.1] Effect of Heating Rate

Results from tests with a constant CSTP while changing the maximum current applied are reported in this sub-section. The results are divided into 2 sub-sections consisting of macroscopic response in the form of punch load versus displacement traces and physical joint characteristics such as surface roughening, fissures and crack formation on the periphery of the deformed protrusion head.

##### [5.4.2.1.1.1] Punch Load Versus Displacement Curves

Changing the maximum current while keeping the CSTP constant had minimal effect on the load versus displacement curves as shown below in Figure 5.32.

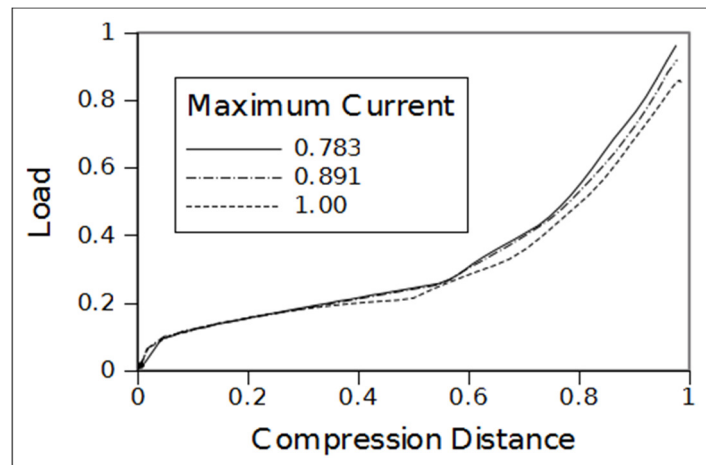


Figure 5.32. A comparison of load versus time traces for AM60 protrusions compressed at a rate of 21mm/s, a CSTP of 141 kA<sup>2</sup>-s.

#### [5.4.2.1.1.2] Protrusion Fracture Characteristics

Different maximum current values while maintaining a constant CSTP was found to cause a difference in the quality of the joint as illustrated in Figure 5.33. For example, increasing maximum current and decreasing the duration of heating to maintain a constant CSTP resulted in a drastic increase in crack formation. The maximum current applied to a protrusion appeared to be linked, and not independent, of other parameters in the crack formation. Other parameters include compression rate and compression distance.

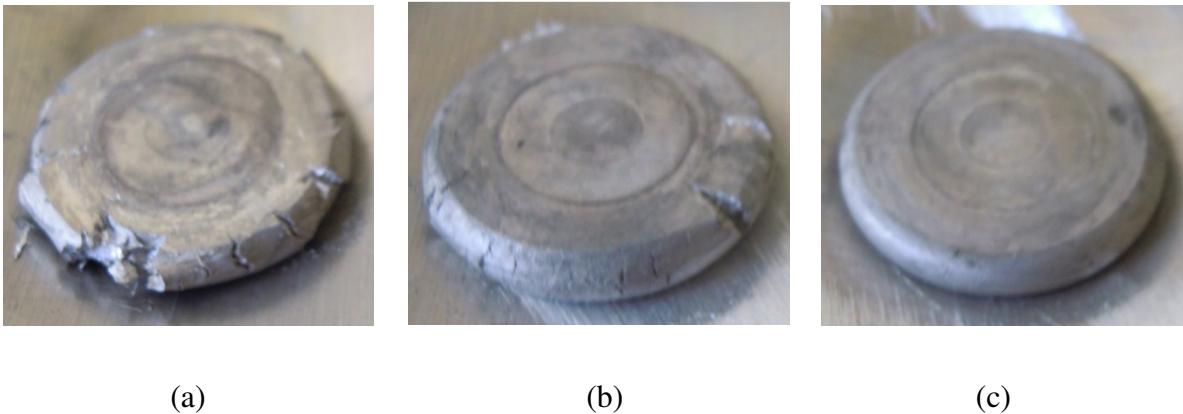


Figure 5.33. A comparison of images of protrusion head compressed at a rate of 31.5 mm/s and with the same CSTP of 100 kA<sup>2</sup>-s and a (a) high, (b) moderate, and (c) low maximum applied current.



Figure 5.34. A defect-free UPJ head from AM60 protrusion formed with a very high maximum current, a high CSTP and a low compression rate.

#### **[5.4.2.1.2] Effect of CSTP Value**

As noted earlier, by increasing the magnitude of applied current and/or duration of applied current increased the CSTP value.

##### **[5.4.2.1.2.1] Punch Load Versus Time Curves**

Figure 5.35 shows the effect of increasing CSTP while compression rate and maximum current applied were constant during deformation. Higher maximum CSTP reduced the load versus time traces.

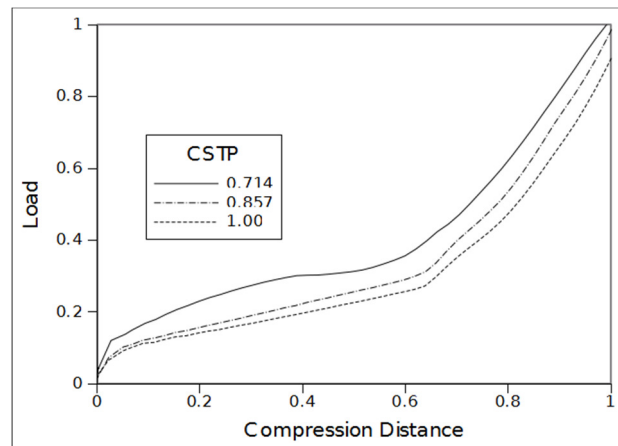


Figure 5.35. A comparison of changing the CSTP on the load versus time traces for AM60 alloy. The protrusion was compressed at a rate of 42 mm/s over a distance of 10 mm with a maximum applied current of 11.5 kA.

#### [5.4.2.1.2.2] Deformed Protrusion Surface and Fracture Characteristics

Figure 5.36 below shows the effect of change in CSTP on cracking and failure of the protrusion. A set of 4 experiments were conducted where the CSTP was varied while keeping the magnitude of current constant. CSTP had a strong effect on the crack formation where a lower CSTP produced surface cracks typically inclined at  $45^\circ$  to the loading axis (see the leftmost image in Figure 5.36). When the CSTP was far larger, catastrophic failures were observed (see the rightmost image in Figure 5.36). The likely origin of this type of failure is still unclear. However, several possibilities are presented in the following chapter. At the optimal CSTP value the protrusion head tended to have defect-free appearance with virtually no surface cracks (see the third image from the left in Figure 5.36).



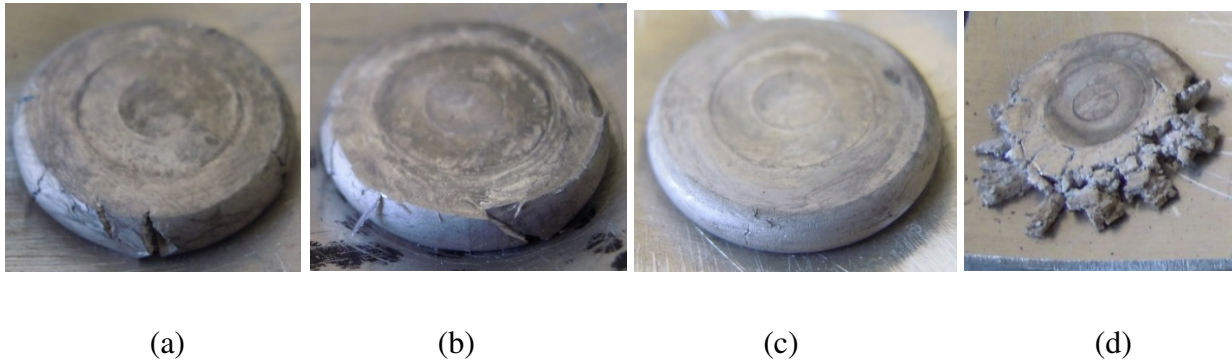


Figure 5.36. Effect of change in CSTP on fracture characteristics of AM60 protrusion compressed at a low compression rate, heated with a high maximum current and with a (a) low, (b) moderate, (c) high, and (d) very high CSTP.

#### [5.4.2.1.3] Effect of Compression Distance

##### [5.4.2.1.3.1] Punch Load Versus Displacement Curves

As expected, an increasing compression distance had no effect on the load versus displacement curve of the compression of magnesium AZ91 as shown in Figure 5.37. All curves fell on top of one another. The samples compressed to lower displacements simply did not attain the level of load of the sample compressed to larger displacements. This test data could also be considered as a measure of good test-to-test repeatability.

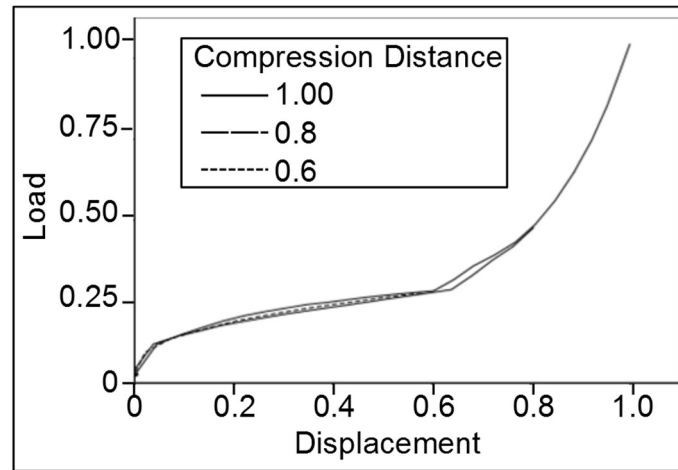


Figure 5.37. A comparison of load versus displacement of protrusions heated with 0 to 11kA over 1 second, a CSTP of 121 kA<sup>2</sup>-s and compressed at a rate of 42 mm/s for 3 different compression distances.

#### [5.4.2.1.3.2] Protrusion Surface and Fracture Characteristics

Increasing compression distance had a direct effect on the initiation, size and number of cracks in AM60 protrusion (see Figure 5.38). Compression distance was a key factor in crack formation since increasing compression directly implies increasing applied strain to the specimen. However, it should be noted that the protrusion head will typically have a fixed final diameter requirement in industrial practice and this would be dependent on a fixed value of compression distance. Therefore, compression distance was not considered a useful process variable for the Taguchi orthogonal array matrix (these results are presented later in this Chapter).

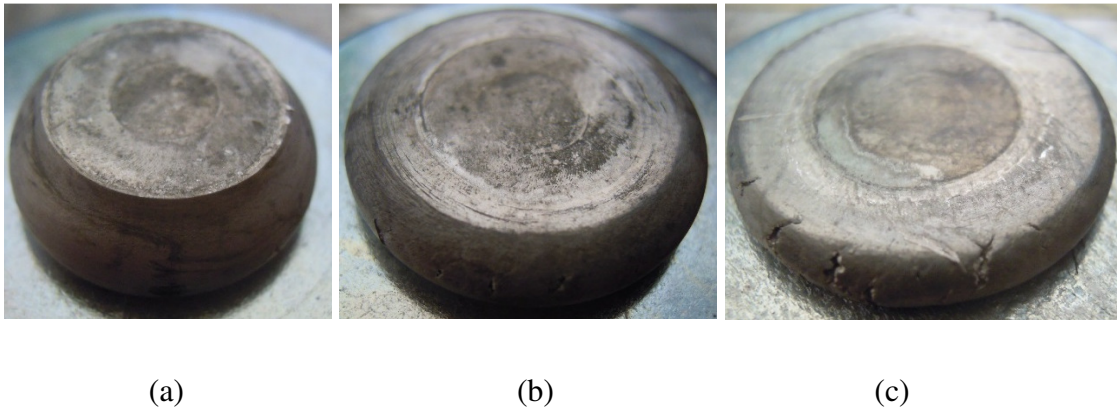


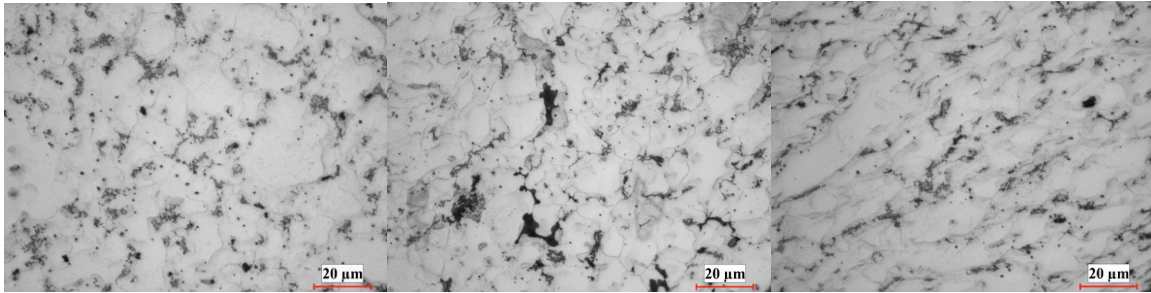
Figure 5.38. Comparison of compression distance on the presence of crack size and density. The protrusions were heated with 0 to 11kA over 1 second, giving a CSTP value of 121 kA<sup>2</sup>-s and compressed at a rate of 42mm/s for distances, (a) 6 mm, (b) 8 mm, and (c) 10 mm.

#### [5.4.2.1.3.3] Effect of Compression Distance on Microstructure

AM60 protrusions were heated with 0 to 11.5kA over 1.07, a high CSTP and compressed at a rate of 21mm/s to distances 5.5mm, 7.5mm and 9.5mm onto steel washers (instead of the earlier aluminum sheet with a hole) with an inner diameter of 14 mm and a thickness of 2 mm. This profile was found to produce optimal results. The samples were cut, mounted, polished and the microstructures observed.

The microstructures exhibited recrystallization in 5.5 and 7.5 mm compression as shown in Figure 5.39. The 9.5 mm compression sample had some recrystallization, but shear bands and grain deformations indicate that the recrystallization was incomplete. This is believed to be due to the rapid increase in strain rate and the decrease in temperature of the protrusion during the last millimetre of compression as the sheet metal accounts for nearly half of the protrusion height. During the last two millimetres of compression, this sheet metal increased the strain rate

significantly. The temperature of the protrusion decreases due to conduction of heat to the electrode and the plate portion of the casting, reducing the formability of the protrusion.



(a)

(b)

(c)

Figure 5.39. Optical micrographs (50x) of the sliced and mounted AM60 protrusion samples at compression distances of (a) 5.5 mm, (b) 7.5 mm and (c) 9.5 mm.

#### [5.4.2.1.4] Effect of compression rate

##### [5.4.2.1.4.1] Punch Load Versus Displacement Curves

The effect of compression rate on load-displacement traces for AM60 protrusion is shown in Figure 5.40 for three different values of compression rates. The load values remain close together for the three compression rates until the last stages of deformation when the peak load increased with an increase in compression rate. The increase in load with compression rate is consistent with positive strain rate sensitivity of AM60 cast magnesium at higher temperatures.

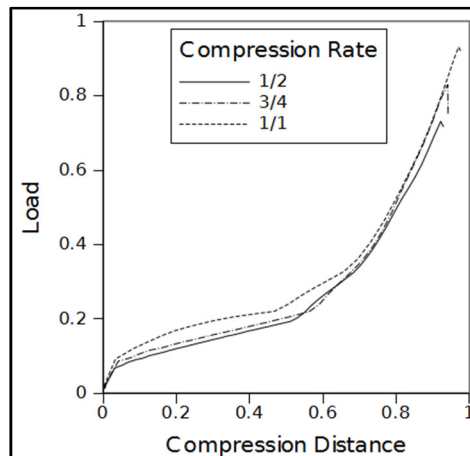


Figure 5.40. Load versus displacement traces at 3 different compression rates. The protrusions were heated with a CSTP of  $141 \text{ kA}^2\text{-s}$  and a maximum current of  $11.5 \text{ kA}$ .

#### [5.4.2.1.4.2] Deformed Protrusion Surface and Fracture Characteristics

Compression rate was a key parameter affecting the quality of the protrusion head for AM60 alloy. Both faster and slower compression rates led to crack formation on the periphery. At higher compression rates, as shown in Figure 5.41(d), the material exhibited plastic instability likely due to increased evidence of adiabatic shear banding in the microstructure (see Figure 5.42). At the slower rate of  $15 \text{ mm/s}$  (Figure 5.41(a)), there was increased heat loss to the surrounding which reduced the outer surface temperature of the protrusion and thus reduced its ductility and likely increased its propensity for fracture.

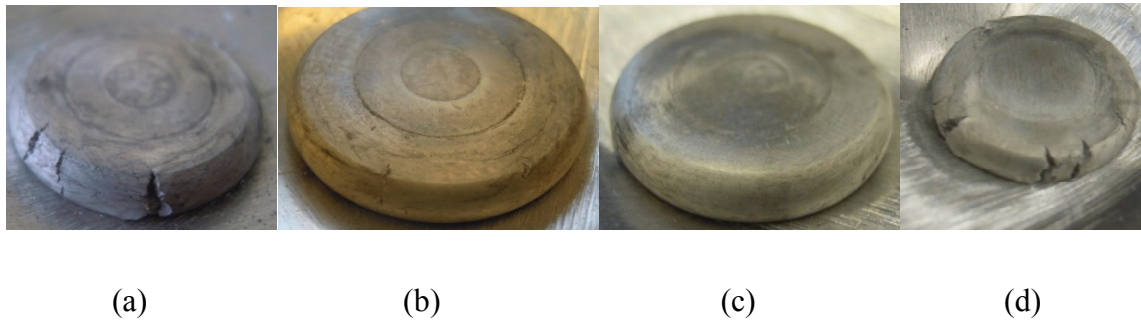


Figure 5.41. A comparison of compression rate of AM60 heated with 0 to 11.5kA, a high CSTP, and compressed at a (a) very low, (b) low, (c) moderate and (d) high compression rate.

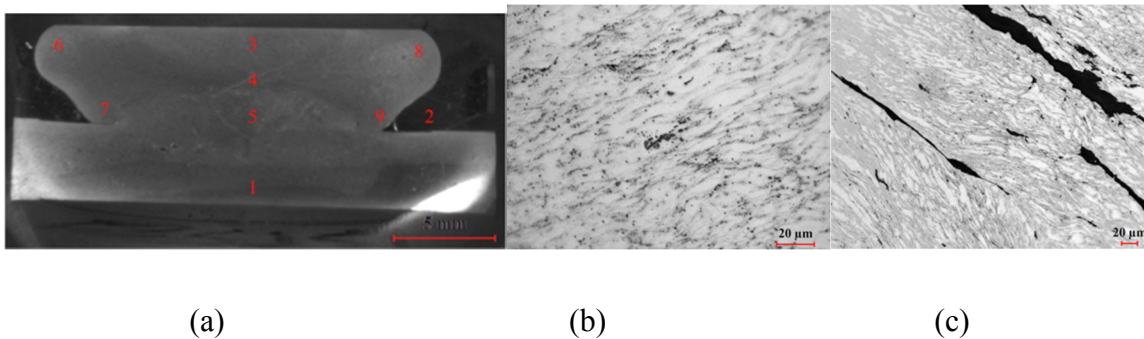


Figure 5.42. Microstructure comparison of compression rates for AM60 specimen heated with 0 to 11.5kA over 1.08 seconds with a CSTP of 141 kA<sup>2</sup>-s. The optical micrographs in (b, c) are from location 8 in (a). The protrusion was compressed at rates 21 mm/s and 42 mm/s to obtain micrographs (a) and (b) respectively.

#### [5.4.2.2] AZ91 Cast Plate with Protrusion

Similar UPJ experiments to AM60 cast magnesium alloy were performed on AZ91 cast magnesium alloy to gain a better understanding of the relative role of material parameters and microstructural characteristics of the 2 materials on the UPJ process. AZ91 alloy was produced via a die casting process similar to the AM60 alloy (see section 4.1.3 in Chapter 4).

#### [5.4.2.2.1] Effect of Constant CSTP with Varying Maximum Applied Current

##### [5.4.2.2.1.1] Punch Load Versus Time Curves

Changing the magnitude of applied current and duration to yield similar CSTP input did not have a noticeable effect on the load applied to the protrusion (see Figure 5.43 below). This was consistent with the earlier result for AM60 alloy.

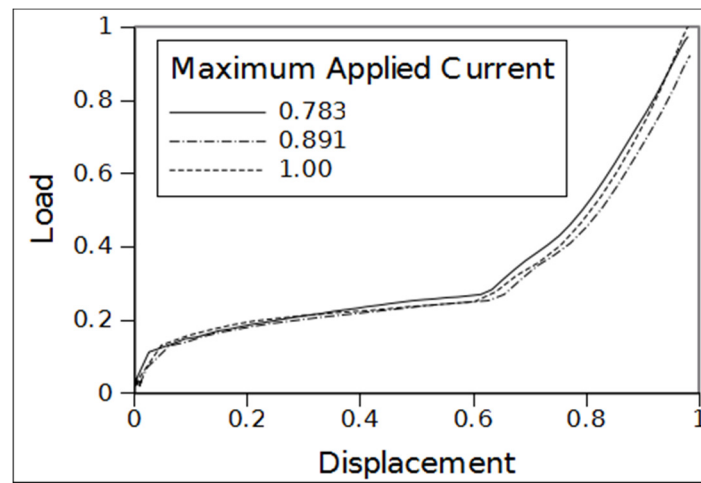


Figure 5.43. A comparison of load versus time traces for compression for AZ91 protrusions compressed by 10 mm at a rate of 21mm/s with a CSTP value of 100 kA<sup>2</sup>-s.

##### [5.4.2.2.1.2] Deformed Protrusion Surface and Fracture Characteristics

Increasing the magnitude of the applied current while maintaining a constant CSTP value of 121 kA<sup>2</sup>-s resulted in crack formation and increased crack density beyond the application of 11.5 kA as shown in Figure 5.44. This was found to be consistent for all experiments with AZ91 alloy.



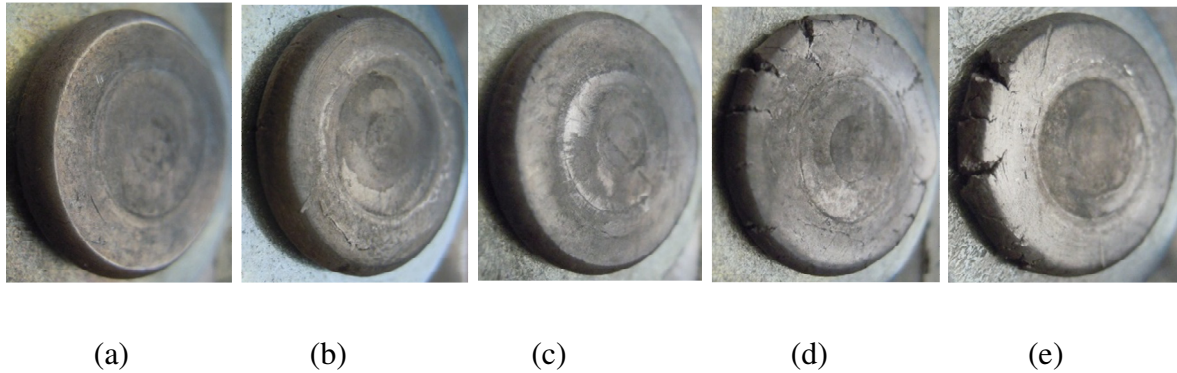


Figure 5.44. Images of AZ91 protrusion heads under a constant moderate CSTP value and showing deformation and fracture characteristics when the maximum current applied was (a) moderate, (b) moderate-high, (c) high, (d) higher and (e) very high.

The magnitude of the applied current and its duration appeared to have a large effect on the crack formation in AZ91 protrusions when CSTP was held constant. As noted earlier for AM60 alloy, a higher maximum current for in a shorter duration potentially prevented heat to transfer through the protrusion to reach the surface. This tended to cause surface cracking as shown in Figure 5.44(d,e). On the other hand, a slower heating rate as a result of lower maximum current may have allowed cooling of the surface prior to compression, preventing crack formation on the skin. An exact reason for increasing maximum current affecting the crack formation was not fully revealed, but it was found as a critical parameter in the formation of cracks on AZ91.

#### [5.4.2.2] Effect of CSTP Value

##### [5.4.2.2.1] Punch Load Versus Displacement Curves

Increasing the CSTP value decreased the load-displacement of the protrusion as shown in Figure 5.45. The characteristic shape of this curve, as noted earlier for AM60, remained unchanged



for all test conditions.

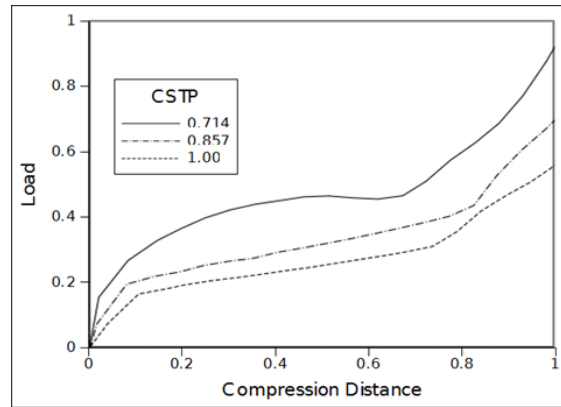


Figure 5.45. A comparison of punch load versus displacement traces for AZ91 compressed at 42 mm/s, a maximum current of 11kA and a set CSTP value.

#### [5.4.2.2.2.2] Deformed Protrusion Surface and Fracture Characteristics

Figure 5.46 shows images of protrusion head of UPJ joint with AZ91 protrusion for different CSTP values. The protrusions were compressed by 10 mm at a rate of 42 mm/s. The protrusion head typically cracked when the CSTP was below a lower threshold value or above an upper threshold value. However, in the intermediate CSTP, between the two thresholds, good joints with no visible fracture on the outer surface were observed. Decreasing the CSTP resulted in fractures into the protrusion while increasing the CSTP resulted in fracture on the outer barrelled surface. A high CSTP would result in small fractures on the surface (see Figure 5.46(e)) that would increase in density and severity with increasing CSTP as shown in Figure 5.46(f). Figure 5.47 shows the image of the UPJ joint produced under conditions well beyond the operational CSTP range of parameters where shattering of the sample into small fragments and melting of the specimen can be observed.

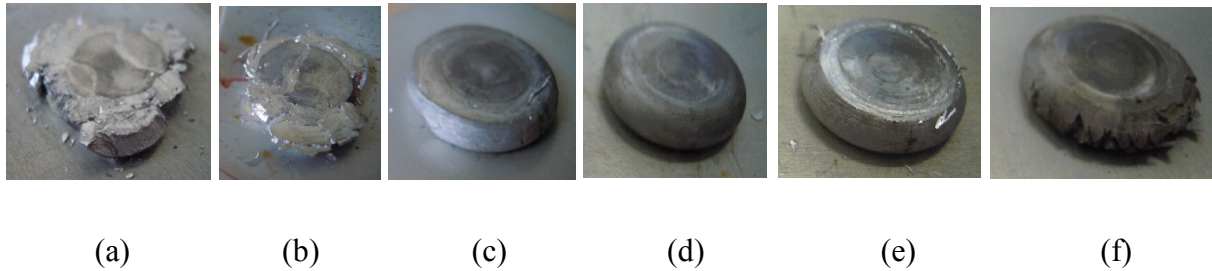


Figure 5.46. Images of protrusion head of the UPJ joint with AZ91 protrusion for different CSTP inputs. The protrusions were compressed by 10 mm at a rate of 42 mm/s and heated with a maximum current of 11kA and a CSTP of (a) nothing, (b) extremely low, (c) very low, (d) low, (e) moderate, and (f) high.

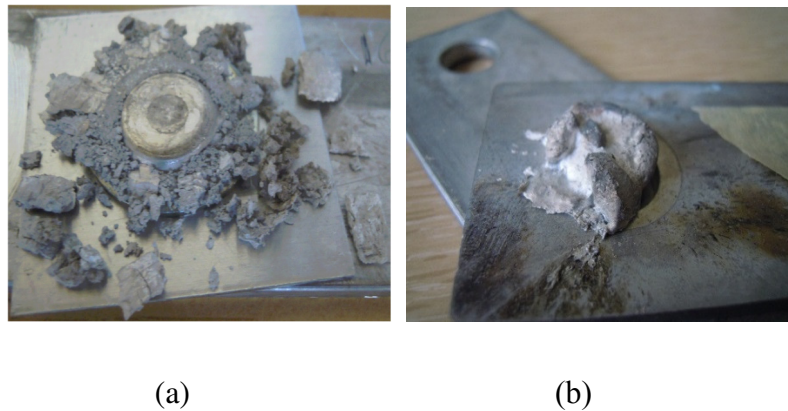


Figure 5.47. AZ91 protrusions subjected to CSTP beyond the operational range. (a) A CSTP value of 160 kA<sup>2</sup>-s fractured into several small pieces during compression. (b) An uncompressed protrusion heated with a CSTP value of 210 kA<sup>2</sup>-s melted.

### [5.4.2.2.3] Effect of Compression Distance

#### [5.4.2.2.3.1] Punch Load Versus Displacement Curves

An increasing compression distance had no effect on the shape of the load versus

displacement curve, a result similar to that for AM60 alloy (see Figure 5.48).

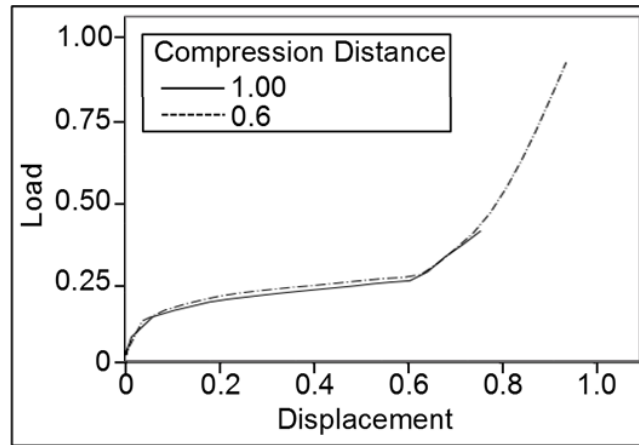


Figure 5.48. A comparison of load versus displacement of protrusions heated with 0 to 11kA over 0.83 seconds and compressed at a rate of 42 mm/s for 2 different compression distances.

#### [5.4.2.2.3.2] Deformed protrusion surface and fracture characteristics

As earlier for AM60, increasing compression distance had a direct effect on the initiation, size and number of cracks in AZ91 protrusion (see Figure 5.49).

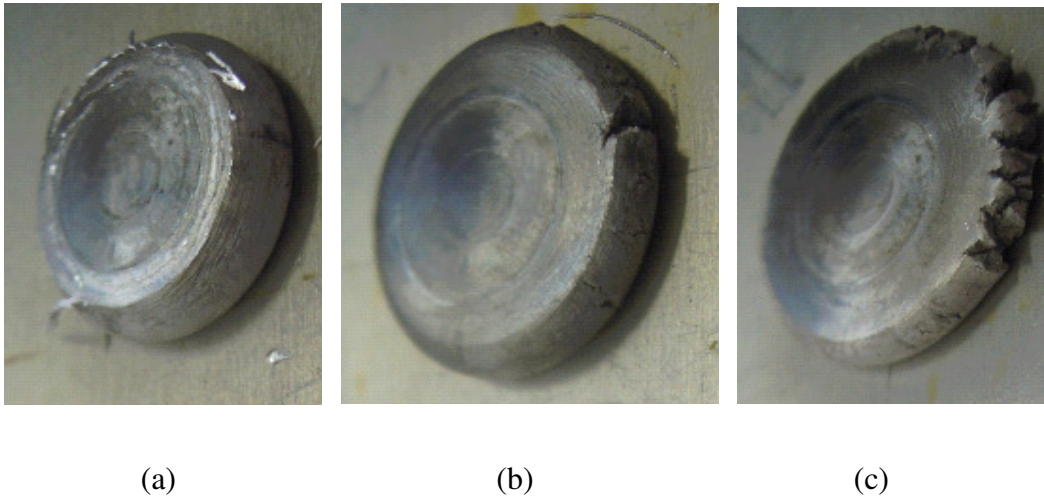


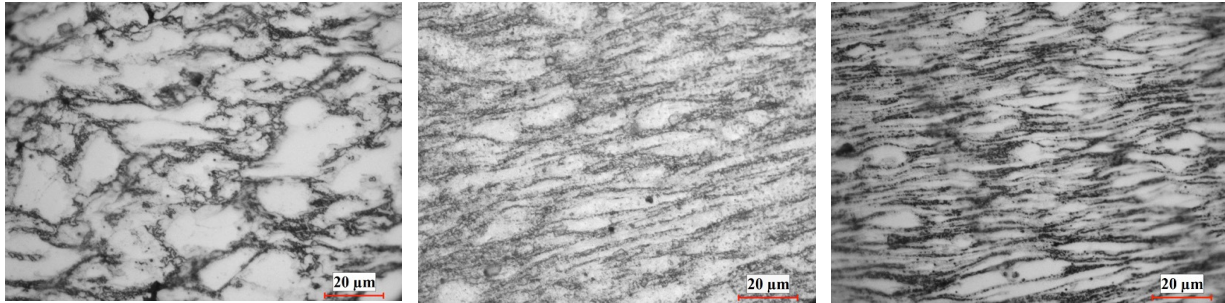
Figure 5.49. Comparison of compression distance on the presence of crack size and density. The protrusions were heated with 0 to 11kA over 0.83 seconds yielding a CSTP value of  $100 \text{ kA}^2\text{-s}$  and compressed at a rate of 21mm/s for distances, (a) 8 mm, (b) 9 mm, and (c) 10 mm.

#### [5.4.2.2.3.3] Effect of compression distance on microstructure

AZ91 protrusions were heated with 0 to 11.5kA over 0.75 seconds giving a CSTP value of  $100 \text{ kA}^2\text{-s}$  and compressed at 42 mm/s to distances 5.5 mm, 7.5 mm and 9.5 mm onto steel washers with an inner diameter of 14 mm and a thickness of 2 mm. The samples were cut, mounted, polished and the microstructure was observed to analyze porosity and material flow in the interior of the protrusion.

The microstructure did not exhibit complete recrystallization. Shear bands and elongation of the grains were present in post deformed protrusions especially at larger compression distances. At the 5.5 mm compression distance the grains remained largely equiaxed (Figure 5.50(a)). This is due to the protrusion being at optimal temperatures for deformation. As the protrusion was compressed further the protrusion exhibited features of colder deformation such as shear bands,

indicating that the protrusion lost heat through conduction to the electrode and to the casting. Increasing initial temperature of the protrusion resulted in crack formation around the periphery and produced poor quality results.



(a)

(b)

(c)

Figure 5.50. Optical micrographs (50X) of the sliced and mounted AZ91 protrusion samples compressed to (a) 5.5 mm, (b) 7.5 mm, and (c) 9.5 mm.

#### [5.4.2.2.4] Effect of Compression Rate

##### [5.4.2.2.4.1] Punch Load Versus Displacement Traces

Figure 5.51 show the effect of compression rate on load versus time and load versus displacement traces for 4 different compression rates. The protrusions were heated with a current of 0 to 11kA over 0.83 seconds, a CSTP of 100 kA<sup>2</sup>-s and compressed to a distance of 10 mm. Unlike with AM60, compression rate had a significant effect on the load versus displacement trace. Increasing compression rate moved the load versus time and load versus displacement curves to higher load levels. This effect is directly related to the positive strain rate sensitivity of AZ91 alloy at higher temperatures. Coupled with compression rate, the slower a protrusion was compressed the greater the heat lost from the protrusion to the surroundings, resulting in a colder protrusion.

The protrusion compressed at 5.25 mm/s resulted in fracture as a result of the heat loss from the protrusion to the surroundings. This fracture was through the middle of the protrusion, not just on the free outer surface, and represented by a sharp drop in the load (see Figure 5.51(b)).

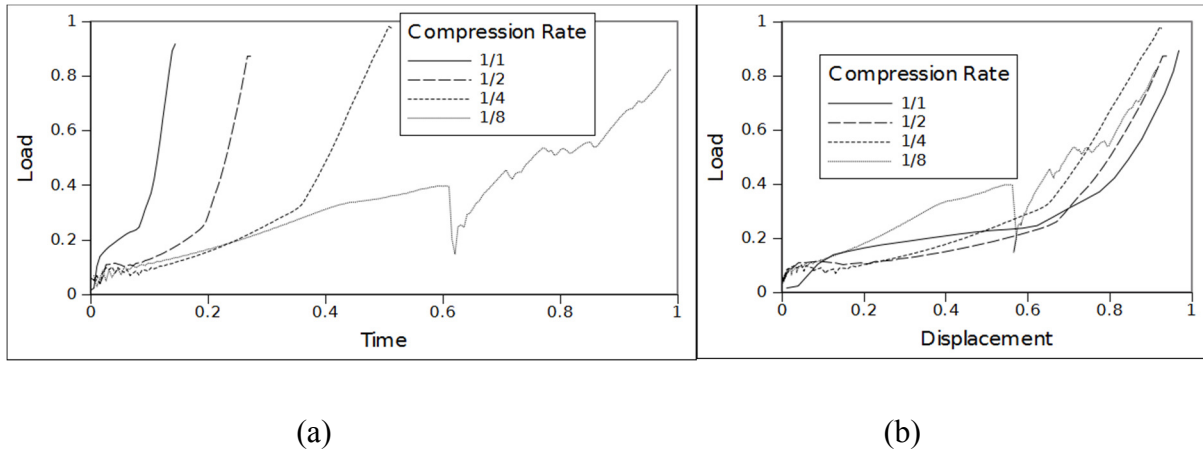


Figure 5.51. (a) A comparison of load versus time traces for AZ91 protrusion compressed at 4 different compression rates and heated with a maximum current of 11kA and a CSTP value of 100 kA<sup>2</sup>-s, (b) A Comparison of load versus displacement traces of magnesium AZ91 compressed at 4 different compression rates.

#### [5.4.2.2.4.2] Deformed Protrusion Surface and Fracture Characteristics

The deformation and fracture characteristics of AZ91 protrusions as a function of compression rate are shown in Figure 5.52. Cracking and fracture occurred at lower compression rates due to protrusion cooling which reduced the ductility of the material. As the compression rate increased, the crack formation was reduced but never quite fully eliminated even at higher compression rates where other microstructural effect such as adiabatic shear instability was noted. In general, the quality of the protrusion head improved with an increase in the compression rate.

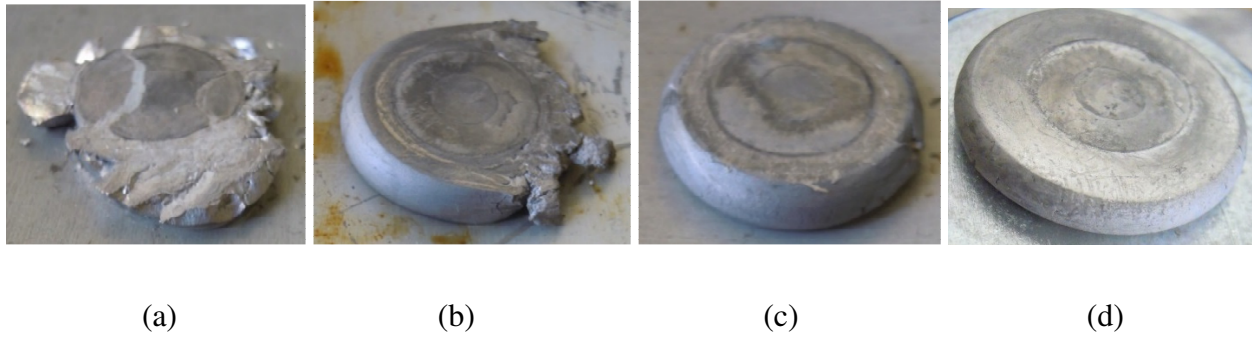


Figure 5.52. AZ91 UPJ protrusion heated with a maximum current of 11kA and a CSTP value of  $100 \text{ kA}^2\text{-s}$  head characteristics as a function of compression rate, (a) eight speed, (b) quarter speed, (c) half speed, and (d) full speed.

#### [5.4.3] Experimental Test Matrix 2 (Taguchi Orthogonal Array) Results

Taguchi method is well recognized for establishing the significance of specific process variables on the process outcome which in the present work was in terms of a quality index of the UPJ part by visual inspection. As noted earlier in Chapter 4, a scale from 1 to 10 was established to characterize the quality of the joint. A Taguchi orthogonal experimental array was created with UPJ process variables; compression rate (CR), maximum current (MC), and CSTP value where each of the variables were assigned 3 different values (low, medium and high) based on the UPJ process limits of the existing equipment at McMaster. Each of the experiments representing a combination of the above process variables were also repeated 3 times to obtain data for a total of 27 tests for each of the 2 cast magnesium alloys (AM60 and AZ91). Each joint was classified in terms of the above quality scale. The  $R^2$  value as a measure of scatter in the prediction data was also calculated.



**[5.4.3.1] AM60**

The results of Taguchi analysis for AM 60 are shown in the form of (i) mean of means, (ii) mean of standard deviation and (iii) mean of signal/noise (S/N) ratio in Figure 5.53(a-c) respectively. A higher mean of means, a lower mean of standard deviation, and a lower mean of S/N ratio are considered the most desirable for an ‘optimum’ combination of the process variables. From the Taguchi analysis, the optimal process variables consisted of a low maximum current, a high CSTP, and a rapid compression rate. The  $R^2$  value of the accuracy of prediction was 71%. Based on the above ‘optimum’ values, a set of 3 repeat experiments were performed and the results are shown in Figure 5.54. It is clear that not all repeat tests based on Taguchi analysis yielded a good quality protrusion head. This variability in the results is discussed in the following chapter.

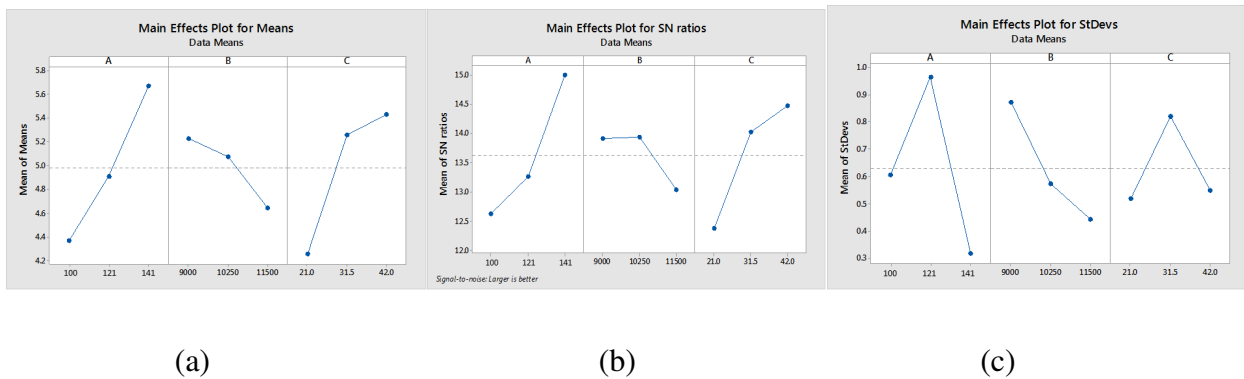


Figure 5.53. Results of Taguchi analysis for UPJ process optimization for part quality of AM60 alloy with the columns of CSTP, maximum current, and compression rate.





Figure 5.54. Three repeat tests for AM60 alloy based on Taguchi optimal process variables. The protrusions were compressed at a rapid rate, a low maximum current and a high CSTP.

#### [5.4.3.2] AZ91

A similar Taguchi orthogonal array using the same 3 process variables (CSTP value, maximum current and compression rate) was created for AZ91 alloy and a set of 27 experiments were performed. The data was once again analyzed as per the 1-10 scale for part quality. The  $R^2$  value of the accuracy of prediction was 58.1%, a value considerably lower than the value of 71% achieved for AM60 alloy. The results of Taguchi analysis are presented in Figure 5.55(a-c). The following optimum process variables were obtained from the analysis; a low maximum current, a moderate CSTP, and a rapid compression rate. Results of subsequent triplicate tests are shown in Figure 5.56. Once again, the outcome of the results was not consistent as both good joint as well as failed one were obtained under identical optimum tests conditions. This is further discussed in the following chapter.

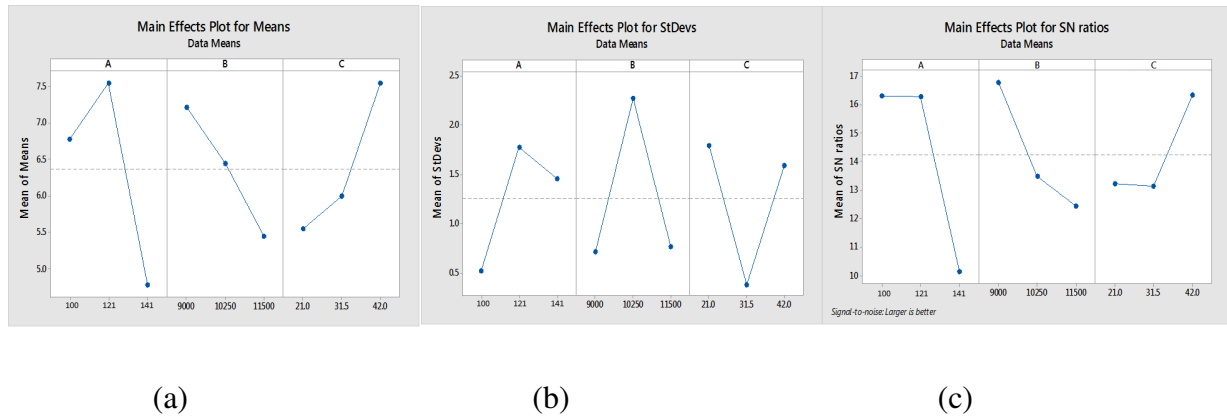


Figure 5.55. Results of Taguchi analysis for UPJ process optimization for part quality of AZ91 alloy.

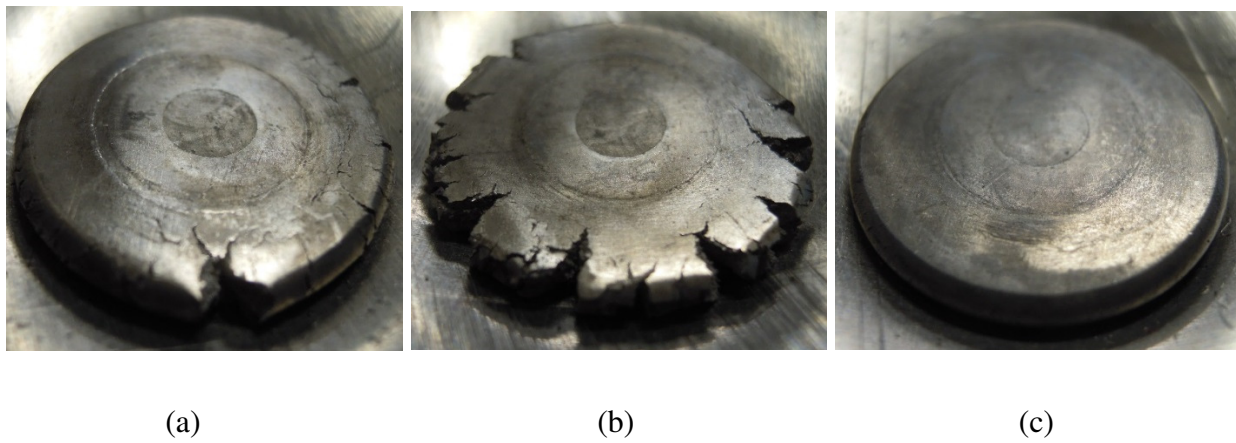


Figure 5.56. Three repeat tests for AM60 alloy based on Taguchi optimal process variables of a high compression rate, a low maximum current and a moderate CSTP. Only one of three tests resulted in a good joint.

### [5.5] Further Process Optimization

Due to the limited success of the Taguchi orthogonal array experimental matrix, more ad-hoc post-UPJ parametric optimization experiments were continued. Trends were noted during

these additional experiments that resulted in visually good quality joints. Further changes to the CSTP value, heating rate and compression rate were performed. For AM60, a parameter using a high CSTP, a high maximum current and compressed at a moderate compression rate produced perfect and nearly perfect results in repeat experiments whereas optimal result from Taguchi orthogonal array had the same heating profile but a high compression rate, producing a sub-optimal result. However, no optimal (completely surface crack free) joint could be produced with AZ91 in the process variable range studied in the present work.

### [5.5.1] AM60

A set of experiments with a heating profile of 0 to 11.5kA over 1.08 seconds, a CSTP of 141 kA<sup>2</sup>-s with varying compression rate was performed. It was found that a slow compression rate produced optimal results. A slower compression had cracking indicating sub-optimal temperatures during compression despite being heated with the same CSTP. This was thought attributed to heat loss from the protrusion to the surroundings as noted in Chapter 5.4.2.2.4.1.



(a)

(b)

(c)

Figure 5.57. Comparison of compression rate at a heating profile of 0 to 11.5 kA over 1.08 seconds compressed at (a) low, (b) medium and (c) rapid compression rates. The low compression rate

produced consistently optimal results.

Specimens obtained under optimal conditions of a high maximum applied current, a low CSTP, and slow compression rate were cut axially through the middle of the protrusion and mounted, as shown in Figure 5.58. A large porosity was present in the protrusion compressed to 5.5 mm (Figure 5.58(a)).

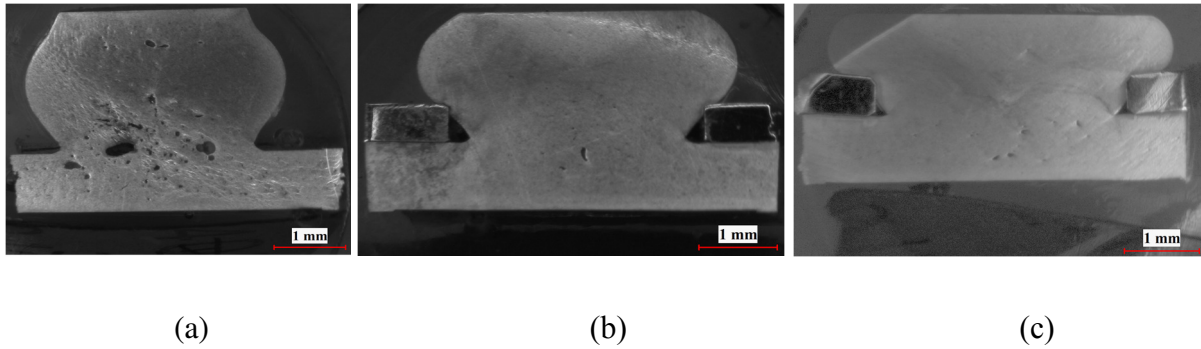


Figure 5.58. AM60 protrusion heating profile of 0 to 11.5kA over 1.08 seconds, compressed at a rate of 21 mm/s to distances (a) 5.5mm, (b) 7.5 mm, and (c) 9.5mm.

Figure 5.39 in Chapter 5.4.2.1.3.3 shows the microstructures of specimens compressed to distances of 5.5 mm, 7.5 mm and 9.5 mm, respectively. The microstructures exhibited fine recrystallized grains with curved grain boundaries indicating that dynamic recrystallization (DRX) occurred when the protrusion was heated and compressed at these conditions. From their smaller grain size of about  $10 \mu\text{m}$  relative to the initial as-cast grain size, dynamically recrystallized grains could be identified. DRX is a combination of nucleation and growth process, as sub-grain formation occurs due to the slip, formation of nucleating sites because of recovery, followed by the migration of grain boundaries (growth) attributing to the release in stored energy while migrating boundaries swept the group of dislocations. From Figure 5.39(c), it can be seen that the

grain growth or the recrystallization during the final 2 mm of compression is somewhat less extent compared to compression from 0-7.5 mm. This may be attributed to the increase of equivalent strain rate when the specimen is compressed at a distance of 9.5 mm. Due to the less time available, the growth of newly formed nuclei is incomplete although nucleation and the formation of new nuclei has occurred.

The optimal low compression rate was tested at heating rates far beyond the original test matrix usually produced good results. In some repeat experiments, the material would melt just under the top surface, showing liquid metal formation. This melting did not affect the surface quality of the barrelled cylindrical (see Figure 5.59).



Figure 5.59. Comparison of two AM60 UPJ joints produced using applied current of 0 to 15 kA over 0.62 seconds and compressed a compression rate of 21mm/s. Liquid magnesium formed under the top surface of the protrusion and spread laterally in the specimen shown on the right. The protrusion head, however, remained crack free.

### [5.5.2] AZ91

As lower internal temperature produced decent results, several tests were performed at a maximum current of 11.5 kA, compressed at 42 mm/s and varying the CSTP value (see Figure

5.60 below).



(a)

(b)

(c)

Figure 5.60. Comparison of surface quality of magnesium AZ91 protrusions compressed at 42 mm/s. The protrusions were heated with a high maximum current and a (a) high, (b) medium, and (c) low CSTP value.

No other set of process parameters resulted in a more desirable joint appearance than a high maximum current, a low CSTP value and a high compression rate. Protrusions were heated and compressed to 5.5 mm, 7.5 mm and 9.5 mm then cut axially across the diameter and mounted for microstructure analysis. The optical micrographs are shown in Figure 5.61.



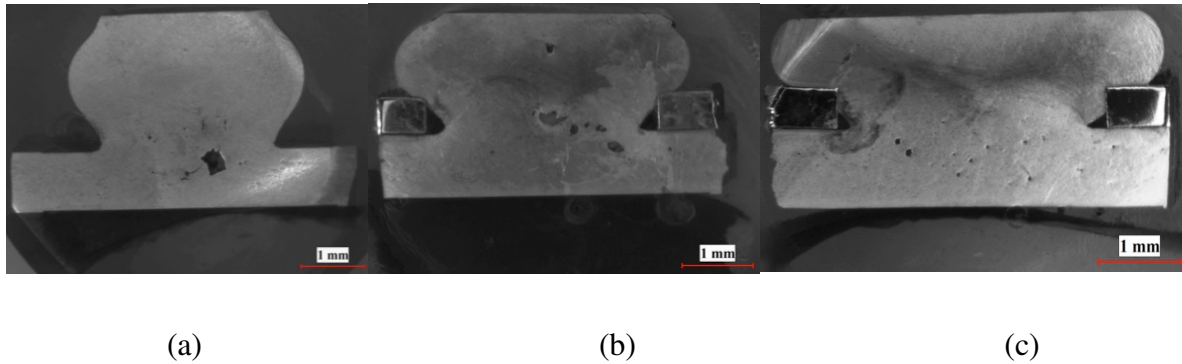


Figure 5.61. Cross-sectional views of the AZ91 UPJ joints with a current profile of 0 to 11.5kA over 0.75 seconds, compressed at a rate of 42 mm/s to compression distances of 5.5 mm (left), 7.5 mm (middle) and 9.5 mm (right).

Figure 5.50(a-c) in Chapter 5.4.2.2.3.3 shows the etched microstructures of samples compressed to 5.5 mm, 7.5 mm and 9.5 mm, respectively. These microstructures do not show any sign of significant DRX. In 5.5 mm compression sample some non-uniform DRX can be observed. Many of the pyramidal slip systems are involved during slip at the predicted protrusion temperature. Hence, the rate of nucleation is expected to be faster than the rate of migration of interfaces (grain boundaries) and the DRX is primarily controlled by the migration rate. Migration depends on the diffusion and may be hindered due to the presence of high volume fraction of  $Mg_{17}Al_{12}$  intermetallic particles on grain boundaries in the starting microstructure of cast AZ91 alloy and thus limiting the DRX. It is reported that new recrystallized fine grains can be easily formed at prior grain boundaries in Mg alloys (Robertson et. al., 2009). However, certain incubation period is necessary for the occurrence of DRX before grain nucleation and growth. At higher compression rates (i.e., high strain rates), the time is not enough for grains to nucleate and grow. Due to the short time available, the heat that is generated during compression does not get

conducted away to colder parts of the protrusion, and therefore a drop in flow stress occurs locally, resulting to the localization of deformation as seen in 7.5 mm and 9.5 mm compression distance samples. Another possibility is that the intermetallic particles on grain boundaries do not act as sources or sinks for vacancies which are essential for the diffusion process. Because of this, thermal recovery might have reduced and so the nucleation of DRX (or the softening mechanism) might be suppressed. It must be noted that the flow localization is also a kind of softening mechanism during which more dislocations are annihilated by the recovery process than are created by each unit of further strain. Dislocation density in sub-grain interiors gets reduced. But if the localization is intensified during the further deformation, formation of shear bands or cracks may occur. There was no cracking observed for AZ91 alloy with the optimized UPJ parameters. This resulted in largely defect-free microstructures.

## **[5.6] Post-UPJ Joint Strength**

### **[5.6.1] General Observations**

The experimental procedure related to UPJ joint testing was presented earlier in Chapter 4. The joints failed in primarily three different ways, protrusion failure at the base, protrusion head separation, and plate failure, as shown below in Figure 5.62. Both failure modes were present on both alloys



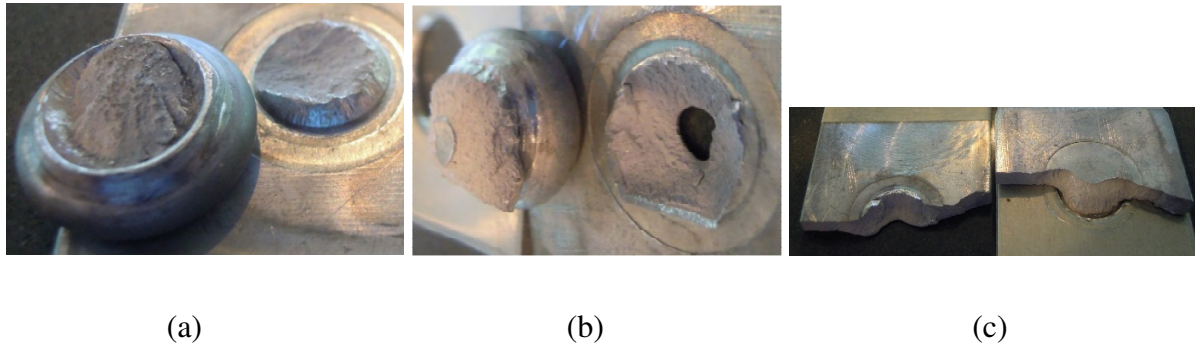


Figure 5.62. Failure modes associated with UPJ joints from tensile tests, (a) protrusion failure from the base of the protrusion, (b) protrusion head separation, and (c) base plate failure. AZ91 samples shown.

Failed samples were observed by cutting, polishing, mounting and observing them under an optical microscope as shown in Figure 5.63. Fractures began at the interface between the protrusion and the cast plate. This location had a sharp fold as a result of the upsetting process. The barrelled material exhibited a fold over, causing a cavity (Figure 5.63(b)). Depending on the upsetting characteristics, different fracture characteristics were observed. An example of the upset location at the base between the protrusion and the cast plate. A cavity was covered by the upsetting process, an optimal location for a crack initiation. As the folding of the material at the base of the protrusion was not a well-controlled process, different cavity geometry and hence crack characteristics were noted (Figure 5.63(b,c)).

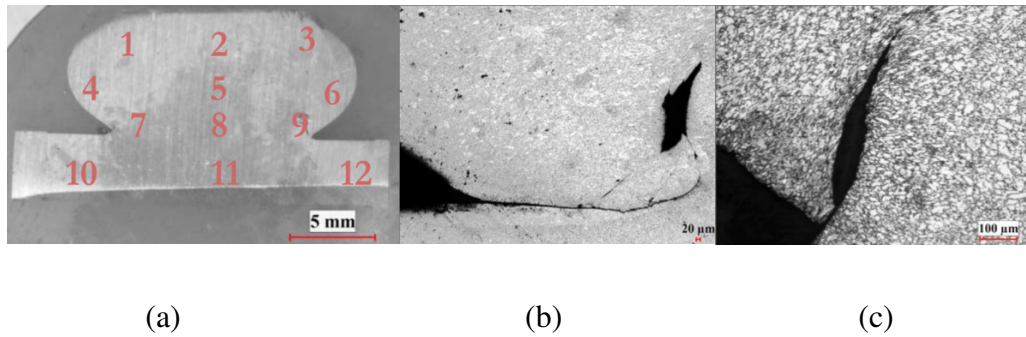


Figure 5.63. Cavities inside an upset protrusion formed in AM60 during the upsetting process. Cavities form on the protrusion at located at 7 on figure (a) of an upset protrusion. The cavities in figures (b) and (c) show two different shapes, indicating different mechanisms of cavity formation and geometry. Sharp corners found inside the cavity localized the stress, resulting in fracture when loaded. Figure (b) shows a protrusion heated with a CSTP of  $141 \text{ kA}^2\text{-s}$  and compressed at  $31.5 \text{ mm/s}$  and figure (c) shows a protrusion heated with a CSTP of  $100 \text{ kA}^2\text{-s}$  and compressed at  $42 \text{ mm/s}$ .

### [5.6.2] Post-UPJ Joint Strength of AZ91

The failure loads were largely constant in the range  $4.5\text{kN}$ –  $5.2\text{kN}$  for a majority of combinations of UPJ process variables (CSTP value, compression distance and compression rate) with a few uncharacteristic data points at about  $6 \text{ kN}$  fracture load (see Figure 5.64). In fact, these high values corresponded to some rather quite poor joints with surface cracks. These failure modes also did not exhibit any trend with respect to the three main UPJ process variables.

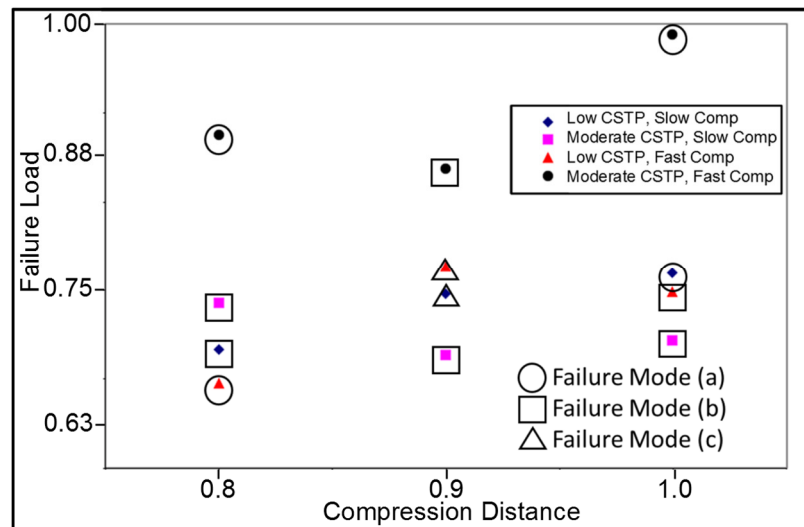


Figure 5.64. Comparison of tensile shear failure loads from UPJ joints obtained from Experimental Test Matrix 1. Failure modes are shown in Figure 5.62.

### [5.6.3] Post-UPJ Joint Strength of AM60

AM60 UPJ joints, obtained as part of the experimental test matrix 2, were also tested at room temperature in uniaxial tension to assess their performance in tensile shear mode of deformation. The samples were pulled at a rate of 10 mm/minute and their Taguchi outputs are shown in Figure 5.65. The failure loads were in the range of 3.1 kN – 6.7 kN for majority of combinations of process variables (CSTP value, maximum current and compression rate). Unlike the prior post UPJ joint strength tests with AZ91, the failure mode did exhibit some clear trends with respect to the three main process variables.

Base plate fracture (12 samples out of a total of 27) and head removal from the plate (again 12 samples out of 27) were the most common fracture modes, with the remaining 3 samples exhibiting internal cracking of the protrusion head. Higher peak current increased the base plate

fractures, while lower maximum current resulted in head removal from the plate. The average strength of the joints as a function of failure mode was highest for plate fracture with a fracture load of about 5.3 kN, head removal from the plate with 4.5 kN, and head cracking internally at 4.3 kN. Based on the Taguchi matrix in Figure 5.65, the strongest joint resulted from a low maximum applied current, a high CSTP and a rapid compression rate. It is to be noted that this set of UPJ process parameters was outside of the optimal processing parameters for producing a crack-free protrusion head.

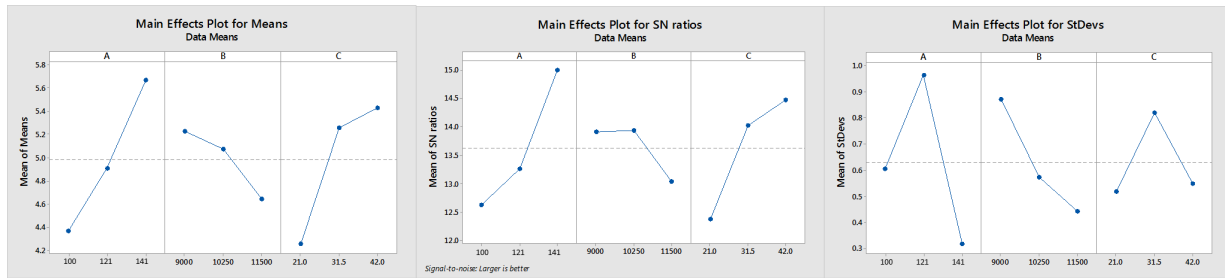


Figure 5.65. Taguchi output matrix in terms of failure load. Increasing the CSTP, decreasing heating rate, and increasing compression rate increased the maximum strength of the joint.

### [5.7] Electrical Resistivity Results

Temperature dependent electrical resistivity measurement procedure was described earlier in Chapter 4. A linear increase in resistivity as a function of temperature was noted for both AM60 and AZ91 are shown below in Figure 5.58. The alloy AZ91 resulted in a higher rate of increase in resistivity with temperature compared to AM60 as indicated by the differences in the slopes of the two curves (see Figure 5.66(a,b)). These slopes were  $1.97 \times 10^{-10}$  Ohm-m/ $^{\circ}$ C versus  $1.52 \times 10^{-10}$  Ohm-m/ $^{\circ}$ C for AZ91 and AM60 respectively. Thus, it clear that the two materials exhibited rather different heating profiles for identical applied currents and current duration during the UPJ process.

AZ91 with higher values of resistivity can be expected to heat up faster and thus achieve a higher protrusion temperature for the same CSTP value.

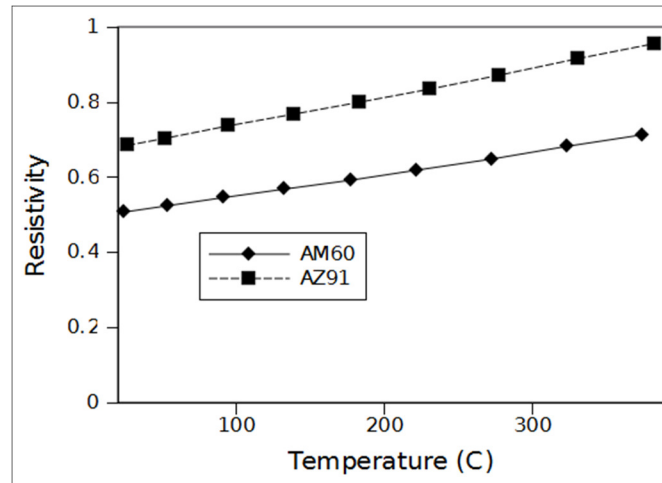


Figure 5.66. Electrical resistivity as a function of temperature of AZ91 and AM60.

## [5.8]. Summary

This chapter provided an extensive assessment of resistance heating and thermo-mechanical deformation behavior of AM60 and AZ91 cast magnesium alloy part when subjected to rapid transient heating and subsequent high strain rate and large deformation to create a UPJ joint. The process consisted of elastic pre-loading, followed by transient electrical resistance heating of the joint, and then followed by high rate deformation of the cast protrusion. Three critical process parameters for the new UPJ process were systematically varied and results pertaining to their effect on UPJ joint quality were presented. The joint quality was assessed in the form of deformed surface and fracture characteristics as well as microstructural changes within the protrusion from the deformation process as well as on the overall response of the material in the form of punch load versus displacement and load versus time traces. In general, AM60 alloy exhibited a larger UPJ

process variable window as well as a more robust UPJ process to achieve good visual quality and a stronger joint compared to the AZ91 alloy. This will be discussed in more detail in the next chapter.

## **Chapter 6. Discussion**

This short chapter presents a brief discussion of some key results from the previous chapter that provide an understanding of the relationship between material and process parameters and general characteristics of the UPJ process. The discussion is divided into 6 short sections. The first section pertains to the characteristics of the new UPJ experimental set-up that has been developed as part of this research work. The second section pertains to physical, mechanical formability characteristics of the two cast Mg alloys in relation to high temperature and high strain uniaxial compression and forming of UPJ joint. A comparative advantage of AM60 over AZ91 is also discussed. The third section focusses on use of CSTP as a UPJ process parameter and its relationship to energy input and internal temperature achieved, as well as its significance in terms of assessing the UPJ joint quality. The fourth and fifth sections summarize the findings of the UPJ process optimization studies and post-UPJ joint strengths and underlying process conditions. The last section discusses the various limitations of the present experimental UPJ set-up as well as other methods of quantification of temperature field and strain field data.

### **[6.1]. New UPJ Test System Characteristics**

The first step towards a comprehensive experimental study of the UPJ process involved development of a well-controlled, laboratory-based, UPJ process. Such a process was successfully developed while keeping the various design requirements and constraints as noted earlier in Chapter 3. Good test-to-test repeatability of the overall process response, as characterized by load and displacement versus time (for example, see Figs 5.28 and 5.29), was achieved. The process cycle time in the range of 1-2 seconds was also achieved for producing individual UPJ joints. The

design allows for making temperature measurements at specific locations within the protrusion with embedded and surface welded thermocouples. The primary objectives of the UPJ system to reduce power consumption and increase process speed were largely achieved. The process parameters could be controlled to rather tight specifications and the effect of process parameters and material properties on the quality of the UPJ joint could be successfully studied by the new UPJ system.

### **[6.2] High Temperature and High Strain Rate Deformation of Cast Magnesium Alloys AM60 and AZ91**

The two magnesium alloys, AM60 and AZ91 were studied for their applicability to the UPJ process. These alloys exhibited quite similar flow behavior under a smaller range of strain rates and isothermal deformation conditions as shown in Figure 5.11. However, their responses under higher strain rate and transient temperature field of the UPJ process was rather different. Also, microstructurally, they are substantially different materials. AZ91 has a higher amount of eutectic phase that is mostly present around the grain boundaries of the matrix  $\alpha$  phase and often quite non-uniformly distributed within the microstructure. At lower temperatures, the eutectic phase region behaves in a brittle manner and causes early onset of damage and crack formation. At higher temperatures, the melting of the eutectic occurs, it creates a two-phase semi-solid material that is unstable during deformation and is likely responsible for failure of the protrusion. This is consistent with the experiments at lower and higher applied CSTP values where extensive cracking of the protrusion head was observed. The best UPJ joints are in fact produced at intermediate CSTP values (see Figure 5.47). Since AM60 alloy has a lower amount of the eutectic phase, it offered a



larger process window (i.e., a larger range of CSTP values and applied currents) for producing a good quality joint. It is to be noted that AM60 exhibited more evidence of DRX during UPJ tests compared to AZ91 alloy at similar compression rates and compression distances. Greater occurrence of DRX in hot deformation is typically associated with enhanced ductility of the alloy. Higher electrical resistivity and higher resistivity rate of change with temperature of AZ91 compared to AM60 alloy (see Figure 5.69) is consistent with experimental observation that it was able to achieve higher internal temperatures, and as a result, should exhibit better formability. However, the temperature window for AZ91 was smaller and higher resistivity and protrusion temperature did not necessarily translate into more defect free UPJ joint due to other factors (for example, porosity).

### **[6.3] Current Squared Time Profile (CSTP) as a UPJ Process Variable**

CSTP was found to have a direct effect on the protrusion temperature. A constant CSTP based on several different combinations of maximum applied current and current duration resulted in approximately the same maximum temperature as measured by both embedded and surface mounted thermocouples in the mid-length location of the protrusion (see Table 5.2 and Table 5.3 in Chapter 5.2). Also, an increased CSTP value linearly increased the maximum temperature at the same mid-length location. Therefore, CSTP appears to provide a good measure of energy or heat input into the protrusion. In fact, energy expression, as shown in Equation 2.1 in Chapter 2, is a function of current squared, time, and resistance. Resistivity, as defined by Equation 4.2 in Chapter 4.3, is a function of the cross sectional area, the length, and the resistance in the system. A third term, the increase in temperature of a bulk item is as shown below:

$$\Delta T = \frac{\text{Energy}}{C_p \rho L \pi r^2} \quad (6.1)$$

where  $C_p$  is the specific heat in kJ/kg-K,  $\rho$  is the density in kg/m<sup>3</sup>,  $L$  is the length in m,  $r$  is the radius in m, and  $\Delta T$  is the change in temperature in °C. Combining Equation 2.1, 4.2, and 6.1 yields the following equation.

$$\Delta T = \frac{\int_0^{t_0} I^2 \frac{\phi L}{\pi r^2} dt}{C_p \rho L \pi r^2} \quad (6.2)$$

where  $t_0$  is the duration of heating in seconds,  $\phi$  is the resistivity of the alloy in ohm-m, and  $I$  is in coulombs per second. The equation is simplified as follows:

$$\Delta T = \frac{\int_0^{t_0} I^2 \phi dt}{C_p \rho (\pi r^2)^2} \quad (6.3)$$

If one assumes that the parameters  $\phi$ ,  $\rho$  and  $C_p$  vary with temperature such that the ratio  $(\phi/C_p\rho)$  remains constant, one could see from Equation 6.3 that the CSTP will then have a direct relationship with temperature of the protrusion. In this case, CSTP can serve as a useful process variable for UPJ. However, this would need to be assessed experimentally for the two cast alloys utilized in this study. One limitation of CSTP is that it does not account for heat loss to the surroundings.

A low CSTP was found to cause crack formation in the form of either slanted or zig-zag cracks. From the experiments in the environmental chamber, this was caused by the protrusion

not undergoing dynamic recrystallization. Localization of deformation and sub-optimal slip systems inside the microstructure would cause shear bands to form inside the protrusion. The outer surface underwent high strains at a low temperature, leading to crack formation. The slanted cracks indicate that the protrusion was under hoop strain and failed in shear. This was also seen at very low CSTP where the protrusion would crack diagonally through the middle. A high CSTP caused the protrusion to fall apart into small chunks as seen in Figure 5.48 in Chapter 5. These chunks were rough and did not fit back together in any way. This is thought to be heating beyond the eutectic temperature of the alloy where the alloy in the grain boundaries to reach liquid temperatures shown in Figure 2.16 and 2.13 in Chapter 2.5. The material inside the grains (primary Mg) was solid or semi-solid while the eutectic alloy in the grain boundaries ( $Mg_{17}Al_{12}$ ) would melt at around 438°C (Lou et al. 2012). This would cause the material to fall apart on the microscopic grain boundaries instead of deforming as a macro alloy. An optimal CSTP allowed dynamic recrystallization inside the protrusion. This prevented shear band formation and allowed the material to deform without failure if the strain rate (or compression rate) was also optimal.

#### **[6.4] UPJ Process Optimization Studies**

AM60 was found to yield optimal UPJ joint quality at a slow compression rate and a high CSTP. The maximum current was found to have a relatively small effect on the result as seen in Figure 5.55. It is unknown why rapid compression rate had a negative effect on the protrusion. Rapid compression rates were optimal according to the Taguchi array while repeated experiments at this compression rate yielded poor and inconsistent results. The skin temperature of the protrusion appears to be critical as to how the protrusion deforms towards the later stages of the

joint. As the temperature of the skin is reduced, it becomes less ductile and prone to early fracture.

Optimal UPJ joint for AZ91 corresponded to a low CSTP value, a low maximum current and a rapid compression rate. This temperature is thought to be a combination of the temperature and strain rate sensitivity (Figure 2.14 in Chapter 2) and the cooling of the protrusion. AZ91 has a thermal diffusivity 16% larger than AM60, coinciding to faster heat loss to the surroundings and greater thermal uniformity within the protrusion. A larger CSTP value resulted in large vertical fractures. From parametric studies, AZ91 joint visual quality was best at low CSTP values (and essentially temperature) and a higher compression rate (see Figure 5.57(a)). A slow compression rate, on the other hand, resulted in heat loss to the surroundings, thus reducing the temperature during compression. Low maximum current and a long heating duration normalized the internal temperature of the protrusion while rapid compression maintained the temperature of the protrusion, enabling it to compress with the fewest cracks. However, the microstructure indicated that no recrystallization occurred at low values of CSTP and compression profile (Figure 5.65 in Chapter 5.5.2). A solution to this would be to apply current during compression for AZ91 to enable recrystallization but this was not tested.

### **[6.5] UPJ Joint Strength Evaluation**

The joints were tested in lap-shear, a process commonly performed on spot welding tests. A large majority of the joints reached their joint strength target as suggested by FCA US. However, the correlation of joint strength and UPJ process parameters was rather tenuous. These experiments, in general, found hotter but more gradually (or slowly) heated protrusions resulted in stronger joints. This is likely due to cavity formation at the base of the protrusion where the

protrusion meets the cast plate as shown in Figure 5.63. A slowly heated protrusion to higher temperatures resulted in the area noted above to become more ductile and formed a smoother cavity. A cooler protrusion resulted in a sharp corner at the cavity that tended to propagate a crack.

#### **[6.6]. Miscellaneous Experimental Limitations**

The use of ARAMIS from GOM and associated digital image correlation (DIC) software was unable able to produce reliable strain field data over the entire length of the specimen during compression experiments inside an environmental chamber. The smaller glass window of the environmental chamber prevented the use of two cameras for a 3D view of the deforming sample. Also, presence of glare, large distance of the cameras from the specimen, and lack of zoom options on the camera resulted in lower than optimal specimen image resolution. These compounding factors resulted in inconsistent strain maps and very poor correlation over the entire image set.

Increased lubrication of the specimen at the specimen-platen interfaces in the case of environmental-chamber based isothermal compression experiments reduced the friction and consequently barrelling. This resulted in a downward shift in the load versus displacement trace, increased the compression distance and the maximum rate of compression prior to fracture as shown in Figures 5.10 and 5.15 of Chapter 5. Unfortunately, the advantages of reduced friction with the application of grease at the specimen-platen interfaces could not be tested for the UPJ process. Presence of grease at the electrode-protrusion interface was not conducive to the electrical resistance heating method. An increase in the surface contact resistance can expected as the grease in the lubricant would burn and deposit onto the electrode.

The temperature of the protrusion was measured externally and internally via a

thermocouple. Internally an ungrounded and shielded thermocouple was used, while externally a thermocouple was welded to the protrusion. The internal thermocouple measured an internal temperature  $\sim 80^{\circ}\text{C}$  colder than the surface mounted thermocouple as seen in Table 5.2 and Table 5.3 in Chapter 5.2. This was attributed to the time delay for the heat to transfer to the thermocouple and the high heat losses to the surroundings, reducing the temperature of the protrusion rapidly after the heating occurred. As well, the microstructure on the surface of the protrusion was reported much denser than that of the inside, resulting in higher resistivity and higher heat generation on the skin surface. Thermocouple measurements were difficult due to single noise. Most of the experiments that had significant noise were removed from this thesis. High noise data would have large variation in output, with a measured value of  $\pm 500^{\circ}\text{C}$  between measurements. Most experiments were unable to measure during the heating phase of the process, to the point where one instrument was heavily damaged measuring a thermocouple. In general, a new system is needed for accurate UPJ temperature measurement. The use of infrared temperature sensor to obtain surface temperature data was unable to produce reliable results. This was due to minimal experience using an equipment that was received on a short term loan and the parameters such as emissivity were not properly calibrated.

The UPJ process did occasionally melt on or near the electrode contact surface. As shown in Figure 5.62(b), the protrusion was subjected to a maximum current of 15 kA. This melted the magnesium just below the top surface. This liquid metal flowed around the protrusion, potentially acting as a lubricant during the UPJ process. There was no accompanying change in geometry or barreling. This could be a new direction for further research on the UPJ process.

A number of as-received die cast magnesium samples were cut and examined for porosity

and other casting defects. In general, there were many sample with large pores and distribution of porosity varied from sample to sample (see Fig. 5.63). Since the die cast process parameters were not available and porosity could not be measured prior to UPJ testing by a non-destructive method, it was impossible to attribute lack of repeatability in UPJ tests under identical UPJ process conditions to porosity. It is likely, that sample-to-sample porosity differences contributed to the variability in the damage development in the form of cracks from sample-to-sample under identical process conditions.

The protrusions were optimized to reduce crack formation on the outer surface. This optimization was for corrosion and visual quality. However, identifying cracks, types of cracks, and crack depth in a quantitative manner was effort intensive and could not be measured. In general, quantitate and accurate crack measurement method was needed, but no repeatable method was found except by visual observations and assigning a value according to Table 4.1 in Chapter 4. This had several limitations, the primary one being that this was a qualitative-to-quantitative chart. This reduced the effectiveness of parametric studies that were designed to optimize the UPJ process. Intuition and analysis of the results did manage to yield optimal results once some of the parameters were optimized through the original process.

The types of cracks noted on the protrusion varied from small surface cracks, vertical cracks, to zig-zag cracks. Small surface cracks were sometimes difficult to find and were like scales on a surface. This can be best seen in the middle diagram in Figure 5.63 of Chapter 5. Vertical cracks were attributed to overheating and/or too rapid a compression at a desirable temperature. They were present in Taguchi optimal results in Figures 5.55 and 5.57. This is thought to be a mixture of too high of a CSTP resulting in the decrease in the material strength and hoop stress. As the skin

surface has a higher grain density from casting, the skin temperature is hotter. If the skin reaches the eutectic temperature the protrusion fails. By compressing slowly the protrusion may lose heat to the surrounding. Zigzag cracks were attributed to a low CSTP. This was seen in Figure 5.47(c) where a slanted crack is seen. This is attributed to a large hoop stress resulting from barreling.

The Taguchi Orthogonal Array was used to optimize for a crack-free protrusion. However, it did not produce an optimal joint. The optimal joints were found through further experiments and analysis of the results. The Taguchi Orthogonal Array is suited for situations where the set of process variables are being related to a clearly quantifiable and measurable output parameters such as yield strength and ultimate strength of a material. Higher and lower strength can be achieved and the parameters in the experiment may have linear, exponential or other trends with respect to strength. For the UPJ process, as the joint quality was assigned a value from a chart and the values had an absolute maximum of 10, the equation relating process variables to UPJ joint quality was unable to find a set trend, let alone relationships amongst parameters. Such interrelationships were found only by empirical observations. For example, a combination of low maximum current and a high compression rate produced a good UPJ joint in AM60, while a high maximum current and low compression rates could produce an even better UPJ joint. Similarly, a combination of low maximum current and low compression rate as well as a combination of high maximum current and a high compression rate produced failures of the protrusion head in the UPJ joint. A new means of finding a quantitative value for the crack is needed for Taguchi method to become suitable for optimizing the UPJ process.



## Chapter 7. Conclusions

[1]. A new computer controlled upset protrusion joining (UPJ) system integrated a commercial spot welding resistance heating system and a commercial servo-hydraulic material testing system. In this process, a cylindrical protrusion on one side of a casting was heated via resistance heating and then rapidly compressed to bond the casting to a sheet metal plate with a hole. The current applied was a ramp function starting from 0 to a maximum current over a duration as a constant current caused the surface of the magnesium to burn.

[2]. The UPJ system was successfully used to rapidly form UPJ joints on two separate cast magnesium alloys, AM60 and AZ91, in 1-2 seconds under a range of process conditions.

[3]. UPJ of the above cast magnesium alloys were tested in tensile lap shear under various process conditions and the failure loads were found adequate for automotive design purposes.

[4]. Parametric studies of UPJ process parameters, material property analysis and microstructure analysis empirically correlated the above cast magnesium alloys with the quality and strength of the UPJ joints. These studies concluded AM60 alloy has a wider UPJ process window for strength and quality of UPJ joints. AZ91 alloy has a smaller process window of acceptable quality and strength.

[5]. A new UPJ process parameter, referred to as current square time profile (CSTP) has been shown to exhibit good correlation with temperature of the protrusion prior to forming.

[6]. The temperature profile from electrical resistance heating was hottest at the symmetric center of the cylindrical protrusion, lower at the base of the protrusion and lowest at the top of the

protrusion. The difference in temperature between the center and top of the protrusion temperature was approximately 70°C, a difference attributed to the high thermal conductivity, low specific heat of the protrusion and high specific heat and thermal conductivity of the electrode.

[7]. Different fracture characteristics of the protrusion head were identified in the creation of the UPJ joint as a function of applied current, CSTP value, compression rate and compression distance.

[8]. Three different failure modes of the UPJ joints were identified from tension-shear tests.

[9]. Some limitations of the newly developed experimental UPJ set-up as well as other methods of quantification of temperature field and strain field data were identified.

## **Chapter 8. Suggestions for Future Work**

[1]. While the studies related to the UPJ process were extensive, additional process parameters should be studied to further assess and expand the usefulness of the UPJ process as a method of joining. It is suggested that the new protrusion and top electrode geometries should be considered in the future.

[2]. The UPJ process may find new and unique applications with other metals and alloys. Therefore, it should be studied for joining other non-ferrous materials which are difficult to join by welding. Materials such as aluminum, zinc and steel castings could be potentially joined by the UPJ process.

[3]. The UPJ joint strength and failure modes were studied in tension shear mode only. Joint strength in cross-tension mode of failure should also be determined as this loading mode will likely exist when an automotive component will be in service. Additionally, tests for corrosion, fatigue, and simultaneous corrosion and fatigue of both lap shear and cross-tension specimen should be carried out for the implantation of UPJ joints in the automotive components.

[4]. In the present study, the protrusion was heated by applying current through a ramp function before compression. Combined profiles, such as a ramp and step, application of heat during compression, and post-UPJ heat treating are key parameters that could improve joint strength, extend UPJ to other alloys and reduce heating durations. Therefore, these aspects should be studied in the future.

[5]. The present study comprised largely of experimental work which at times was challenging as

some of the useful output parameters such as temperature and strain fields as a function of UPJ process variables could not be determined with certainty due to limitations of the experimental techniques and the constricted space where UPJ occurs. A powerful computational method of finite element (FE) analysis could be utilized to simulate the electrical resistance heating process to obtain the transient temperature field within the protrusion. Also, this temperature field can then be utilized in another FE model to simulate the high rate thermo-mechanical deformation of the protrusion to analyze the material flow as well as strain localization, damage development, and fracture characteristics. A good correlation of the model results with the experimental results presented in this thesis will greatly enhance further optimization of the UPJ process via modeling in a cost-effective manner.

## Chapter 9. References

- ASTM Standard B63-07, 2013, Specification for concrete aggregates, ASTM International, West Conshohocken, PA. pp. 1-3.
- American Foundry Society, 2006. Magnesium Alloys. The American Foundry Society Technical Department, Schaumburg, IL.
- Bauccio, M., ASM Metals Reference Book. ASM International, Materials Park, OH.
- Braszczyńska-malik, K., 2011. Precipitates of Gamma-Mg<sub>17</sub>Al<sub>12</sub> Phase in Mg-Al alloys, Magnesium Alloys - Design, Processing and Properties, Frank Czerwinski (Ed.), ISBN: 978-953-307-520-4, InTech.
- Buch, A. 1999. ASM Specialty Handbook – Magnesium and Magnesium Alloys. ASM International, Metals Park, OH. pp. 22-49.
- Campbell, F., 2008. Elements of Metallurgy and Engineering Alloys. ASM International, Materials Park, OH. ISBN -10: 0-87170-867-1. pp. 208-209.
- Chung, C., Ding, R., Chiu, Y., Hodgson, M., Gao, W., 2009. Microstructure and mechanical properties of an as-cast AZ91 magnesium alloy processed by equal channel angular pressing. *Processing, Microstructure and Performance of Materials*. IOP Publishing. Doi:10.1088/1757-899X/4/1/012012.
- Coppieters, S. 2012. “*Experimental and numerical study of clinched connections*” Ph.D. thesis,

KU Leuven, Department of Metallurgy and Materials Engineering.

- Čížek, L., Greger, M., Dobrzański, L., Juříčka, I., Kocich, R., Pawlica, L. & Tański, T., 2006. Mechanical properties of magnesium alloy AZ91 at elevated temperatures. *Journal of Achievements in Materials and Manufacturing Engineering*. Vol. 18 Is. 1-2, Sep-Oct. pp. 203-205.
- Guldberg, S. & Ryum, N., 1997. Microstructure and crystallographic orientation relationship in directionally solidified Mg-Mg<sub>17</sub>Al<sub>12</sub>-eutectic. *Materials Science and Engineering*, Vol. 289 Is. 1-2, Sept. pp. 143-150.
- Ho, C., Ackerman, W., Wu, K., Havill, T., Bogaard, R., Matula, R., Oh, S., & James, H., 1983. Electrical resistivity of ten selected binary alloy systems. *Journal of Physical Chemistry Reference Data*, Vol.12, No.2, pp. 138, 207.
- Hynes, L., 1948. Industrial Electric Resistance Heating. *AIEE Transactions*, Vol. 67, pp. 1359-1361.
- Johnson, G. & Cook, W., 1983. A constitutive model and data for metals subjected to large strains, high strain rates and high temperatures. *Proceedings of the 7<sup>th</sup> International Symposium on Ballistics*, pp. 541-547.
- Kang, Z., Ping, Y. & Lilong, C., 2015. Constant current vs. constant power control in AC resistance spot welding. *Journal of Materials Processing Technology*, Vol. 223, pp. 299-304.
- Kuhn, H. & Lee, P., 1971. Strain instability and fracture at the surface of upset cylinders.

*Metallurgical Transactions*, Vol. 2, pp. 3197-3202.

Liu, L., Zhou, S., Tian, Y., Feng, J., Jung, J., & Zhou, Y., 2009. Effect of surface conditions on resistance spot welding of Mg alloy AZ31. *Science and Technology of Welding and Joining*, Vol. 14, No. 4, pp. 356-361.

Lou, A., Zang, C., Sachdev, A., 2012. Effect of eutectic temperature on the extrudability of magnesium-aluminum alloys. *Scripta Materialia*, Vol. 66 Is. 7 April, pp. 491-494.

Luo, A., Lorimer, G.W. (Ed.), 1996. Understanding the Solidification of Magnesium Alloys. *Third International Magnesium Conference*, Manchester, UK, pp. 449-464.

Matos, A., 2010. Multiaxial fatigue simulation of an AZ31 magnesium alloy using ANSYS and a plasticity program. Master's thesis, University Técnica de Lisboa, France.

Marciniak, Z., Duncan, J., & Hu, S., 2002. *Mechanics of Sheet Metal Forming*. Jordan Hill, Oxford: Linacre House. pp. 61-80.

Matumoto, R. & Osakada, K., 2010. Ductility of a magnesium alloy in warm forging with controlled forming speed using a CNC servo press. *Journal of Materials Processing Technology*, Vol. 210, pp. 2029-2035.

Mrvar, P., Terčelj, M., Kugler, G., Fazarinc, M., & Medved, J., 2006. Characterization of solidification and hot workability of MgAl6Mn foundry alloy, *RMZ-Materials and Geoenvironment*, 52(2) pp. 175-192.

Mucha, J., Kaščák, L., Spišáka, E., 2011. Joining the car-body sheets using clinching process with

- various thickness and mechanical property arrangements, *Archives of Civil and Mechanical Engineering*. Vol. 11 Is. 1, pp. 135-148.
- Pérez-Prado, M., del Valle, J., Contreras, J., Ruano, O., 2004. Microstructural evolution during large strain hot rolling of an AM60 Mg alloy. *Scripta Materialia*. Vol. 50, Is. 5. pp. 661-665.
- Polmear, I.J., 1989. *Light Alloys, Metallurgy of the Light Metals*, 2<sup>nd</sup> edition, Edward Arnold, London. pp. 237-249.
- Ravi Kumar, N.V. et. al., 2003. ‘Grain refinement in AZ91 Mg alloy during thermo-mechanical processing’, *Materials Science Engineering*. A 359 pp. 150-157.
- Ricketts, N., 2014. Properties of cast magnesium alloys. [http://mg.tripod.com/asm\\_prop.htm](http://mg.tripod.com/asm_prop.htm)
- Robson, J.D., Henry, D.T. & Davis, B., 2009. ‘Particles effect on recrystallization in magnesium-manganese alloys: Particle-stimulated nucleation’, *Acta Mater* 57 pp. 2739-2747.
- Semiatin S., & Jonas, J., 1984. *Formability and Workability of Metals*. Ohio: American Society for Metals Park.
- Solberg, J. & Tørklep, J., 1991. Superplasticity in magnesium alloy AZ91. *Materials Science and Engineering*. Vol. 134, pp. 1201-1203.
- Spotwelding Consultants Incorporated, 2015. Recommended use of resistance welding materials. <http://www.spotweldingconsultants.com/tuffaloy/DATA.html>
- Zhu, T., Chen, Z. & Wei, G., 2010. ‘Effect of cooling conditions during casting on fraction of  $\beta$ -



Mg<sub>17</sub>Al<sub>12</sub> in Mg-9Al-1Zn cast alloy', *Journal of Alloys and Compounds*, 501 pp. 291-296.

Wang, S. & Wei, P., 2001. Modeling dynamic electrical resistance during Resistance spot welding. *American Society of Mechanical Engineers*, Vol. 123, pp. 576- 585.

Wang, L., Zhang, B., Zhu, S., Zhang, C. & Guan, S., 2007. Application of silicocalcium in Mg-6Al-0.5Mn alloy. *China foundry*, Vol. 4 No. 4 pp. 284-287.

Yakubtsov, I., 2010. Effect of composition and microstructure on behaviours of electrical resistivity during continuous heating above room temperature in Mg-based alloys. *Journal of Alloys and Compounds*, Vol. 492, pp. 153-159.

Yan, C., Bai, R., Gu, Y. & Ma, W., 2008. Investigation on the mechanical behaviour of AM60 magnesium alloys. *Journal of Achievements in Materials and Manufacturing Engineering*. Vol. 31, is. 2, pp. 398-401.

Zeng, R., Chen, J., Dietzel, W., Zettler, R., Santos, J., Nascimento, M. & Kainer, K., 2009. Corrosion of friction stir welded magnesium alloy AM60. *Corrosion Science*, Vol. 51, pp. 1738-1746.